The Study of Ship Motions in Regular Waves using a Mesh-Free Numerical Method

by

Bruce Kenneth Cartwright, B. Eng., M. Sc.

Submitted in fulfilment of the
requirements for the Degree of

Master of Philosophy

University of Tasmania

April 2012

Candidate	Bruce Kenneth Cartwright
Student number	602728
Department	National Centre for Maritime Engineering and Hydrodynamics Australian Maritime College
Supervisors:	
Primary	Professor M. R. Renilson, Australian Maritime College
Co-	Mr G. J. Macfarlane, Australian Maritime College
Research Advisors:	
	Dr S. M. Cannon, Defence Science and Technology Organisation, Melbourne, Australia.
	Dr P. H. L. Groenenboom, ESI Group, Delft, Netherlands.

Declaration

I certify that:

a) except where due acknowledgement has been made, the work is that of the candidate alone

b) the work has not been submitted previously, in whole or in part, to qualify for any other academic award

c) the content of the thesis is the result of the work which has been carried out since the official commencement date of the approved research program

d) ethics procedures and guidelines have been followed

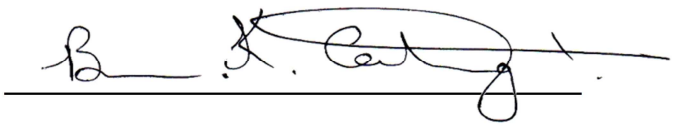

Bruce K Cartwright

Date: 12th April 2012

Authority of Access

This thesis may be made available for loan and limited copying in accordance with the Copyright Act 1968.

Abstract

Mesh-free methods are becoming popular in the maritime engineering fields for their ability to handle non-benign fluid flows. Predictions of ship motions made using mesh-free methods need to be validated for benign conditions, such as regular waves, before progressing to non-benign conditions. This thesis aims to validate the response of a ship in regular waves by the Smoothed Particle Hydrodynamics (SPH) mesh-free method.

Specifically, the SPH technique uses a set of interpolation points, designated SPH particles, located at nodes that track the centre of discrete fluid volumes with time. As part of this research a set of simple rules was established to locate the free surface of the fluid based on the location of the SPH particles. These simple rules were then used to validate the hydrostatics of a ship floating in the fluid, identifying the vertical location of the water line to 0.22% of the Design Water Line length.

The propagation of regular waves in SPH has historically been problematic, resulting in diminishing wave height with propagation distance. In this study, non-diminishing deep-water regular waves were generated in a shallow tank by moving segments of the floor in prescribed orbital motions, a technique developed by the researcher and hereinafter called the moving-floor technique. The resulting waves showed no discernible loss in wave height with propagation distance, and were computationally more efficient than modelling a full-depth tank. The resulting surface profiles of the waves were within ± 5% of the theoretical values, while the velocity and pressure profiles were within ± 10%.

The pitch and heave transfer functions for a round bilge high speed displacement hull form at Froude numbers of 0.25 and 0.5 were predicted using waves in SPH developed by the moving-floor technique. These predictions were compared to transfer functions obtained from experiments in a towing tank. The results obtained using SPH generally under-predicted the experimental results by about 10%, but by as much as 50% at peaks or at high frequencies where the responses were small. Reasons for the under-prediction by the SPH technique are discussed in this thesis.

The outcomes of this research demonstrate that with some refinement, the SPH technique should be capable of accurately predicting the motions of a ship in regular waves. It is hoped this work will serve as a stepping stone to exploit the flexibility of the SPH technique to analyse any shape hull, to be applied to non-linear waves, and to be coupled with a structural solver.

Acknowledgements

It is a pleasure to acknowledge my Principal Supervisor, Professor Martin Renilson, for his continued enthusiasm, guidance, encouragement and relentless questioning of my ideas that have facilitated my understanding of the subject sufficient to complete this body of work.

I also thank Dr Paul Groenenboom for his assistance with the preparation and explanations of the software on which much of this work is based.

Damian McGuckin deserves special thanks for allowing me to use the resources of his company, Pacific ESI, to conduct this work.

Finally this work would not have been possible without the support of my partner, Carol Atkinson, for all the things she does.

Contents

1 Introduction

1.1 *Motivation*

The motivation for this research was to explore the use of a generic hybridised mesh-free and finite element method as a universal tool for the prediction of the structural response of a floating structure to waves.

The vision was to have one software tool that can predict both the global motions, and the global and local structural response, including damage, of a floating, or sinking, structure subjected to any wave scenario. Such a capability was envisaged to be useful to the assessment of not only monohull vessels, but also multihull and small water-plane area twin hull (SWATH) vessels, submarines, off-shore structures, high-speed and lightweight vessels. It could also turn out to be useful in the investigation of the response of structures which accidentally found themselves in or on the water, such as ditching of aircraft or helicopters, or the human body itself in a boat subjected to violent wave forces.

In practise, validating the vision was a bold task. Hence, the research presented here has focused on establishing the groundwork for the vision by:

a. restricting the scope to that of a rigid-ship motion response in regular waves; and

b. comparing these results to tank tests and linear theory predictions.

The vision to have one software tool to conduct the complete hydrodynamic and structural response prevails. It is hoped the work here will be continued, and some recommendations to achieve this are presented in Chapter 9, Future Work.

1.2 *Aim of the Current Work*

The aim of the current work was to build confidence in mesh-free methods by comparing the numerical simulation predictions to conventionally generated results from model towing tank tests and linear theory. One specific hull at two speeds in regular head waves has been compared.

The hull form used was a hull developed by the Australian Maritime Engineering Cooperative Research Centre (AMECRC) as part of their High Speed Displacement Hull Form (HSDHF) Systematic Series. The specific hull chosen was the model known as the AMECRC09. This hull is typical of a generic high speed naval vessel. The results used for a baseline are those from the work of Macfarlane and Lees (1999).

1.3 *Approach to the Present Work*

Mesh-free methods are emerging in various sectors of the maritime sector but are not yet commonplace. As they are not commonplace yet, a number of simple steps were taken in this research to build confidence in the mesh-free approach for ship motions. Exploring the buoyant force on some submerged shapes in two and three dimensions with this mesh-free method allowed some hydrostatic concepts to be validated. Next, the simulation of the classical dam break scenario provided some validation of the method's ability to handle various free surface conditions such as splash and the interaction between the fluid and a rigid body.

Non-diminishing regular waves in a mesh-free fluid domain have not been demonstrated previously in the literature. A novel technique to achieve such waves in a mesh-free domain has been developed in the course of this research. The waves developed by this approach are presented for a variety of wave frequencies.

Finally the mesh-free predictions of motions for a vessel in regular waves will be presented and compared to results for the same vessel in tow tank testing and from an industry-standard linear theory panel method.

1.4 *Use of a Robust Code*

One of the underlying ideas behind this research was to use well-proven, commercial software tools, and in particular to be able to rely on their underlying robustness. The key feature here being that the commercial software tools are reliable in their execution and implementation, yet their use within the maritime fraternity is new, such that the techniques for producing reliable results have not been demonstrated to the industry. That, to some degree, is the essence of this research: the development and demonstration of techniques to deliver reliable results.

2 Theoretical Background

2.1 *Mesh-Based Methods*

The traditional numerical analysis of a fluid's dynamical behaviour over time relies on the subdivision in space of the fluid into smaller pieces that can be analysed individually (Liu 2002). The behaviour of the system of smaller pieces taken as a whole over the time-frame in question then describes the original complete system. The process of producing these smaller pieces is called discretisation, which involves the use of cells or elements to represent either the fluid body, a Lagrangian discretisation, or the space in which the fluid resides, an Eulerian discretisation. The resulting elements are a "mesh" that represents both the geometry of the system and the connectivity of each element therein to its neighbour(s). In a Lagrangian system, the mesh moves with the fluid. In this approach the free surface will always be at the interface of two specific elements, one filled with water the other filled with gas. In an Eulerian system, the fluid is mapped onto the mesh, and the fluid then flows through the mesh with time and the location of the free surface will be defined by the proportion of fluid and gas in any specific element.

The governing equations for the system, based on principles such as the conservation of mass, energy and momentum, and expressed as differential and partial differential equations, are written to address the changes for any single cell or element. While these equations will be similar for both the Lagrangian and Eulerian systems, there will be differences because of the different frame of references used.

Due to the different approaches being employed, there is an inherent difference in the ability of the two systems to solve specific problems (Liu and Liu 2003). When tracking the location of a moving free-surface or the interface of two materials is the aim, the Langrangian formulation is best as the mesh moves with the interfaces. This is reliable up to the point the movements begin to severely distort the shape of the elements, and numerical stability may become a problem due to irregular shaped elements. For the Eulerian system the mesh does not distort, but instead additional computations are required to accurately locate the free surface or interface within the mesh elements.

When large mesh distortions become a problem for the Lagrangian formulation it is possible to then ***re-mesh*** the fluid with an undistorted mesh to permit the computations to continue. Without making light of the intricacies of the task, re-meshing is basically the mapping of all variables from one mesh onto another mesh in such a way that any errors induced will be small. The final mesh should ideally be more uniform and consistent in element size and distribution, and hence have more favourable numerical properties than the original mesh. However, re-meshing will almost always require considerable computational effort, and there is often some loss of information from the system that will diminish the accuracy of the solution (Liu and Liu 2003).

2.2 *Mesh-Free Methods*

Mesh-free methods define a system by a set of points that are able to move around the domain, instead of a mesh of elements, or cells. Associated with those points are various properties. The governing equations for the system describe how the points interact with each other, taking into consideration those properties.

As the points are discrete, with no connectivity to their neighbours, one of the advantages of mesh free methods is their ability to handle large geometric distortions of the original configuration and remain numerically stable.

A specific field of mesh-free methods is the so-called Mesh-free Particle Method, or MPM, where a finite number of points is used to track both the state of the system and the motion of the system. One of the most developed of these methods is the Smoothed Particle Hydrodynamics (SPH) technique. This was specifically developed as a system of discrete particles to describe a continuum system (Liu and Liu 2003). Importantly, the SPH method is a Lagrangian method.

Liu (2002), Vignejvic (2004), Nguyen et al (2008) and Liu and Liu (2010) provide a summary of the many, more commonly used, mesh free methods available such as the Element-Free Galerkin (EFG) method, the Reproducing Kernel Particle Method (RKPM), the Point Interpolation Method (PIM), the Moving Particle Semi-implicit (MPS) method, and the Finite Point Method (FPM). In this work the SPH mesh-free method has been chosen exclusively as it the most mature of the mesh-free methods available, based on the volume of published papers.

2.3 *Formulation Principles for SPH*

This section outlines the fundamental mathematics of the SPH formulations and is based on the book by Liu and Liu (2003). These formulations are the same as those set out by the originators of the technique Lucy (1977), and Gingold and Monaghan (1977), and are the same as those which are employed in the commercial software code PAM-CRASH (2009) which is used for this research, henceforth referred to simply as ‘the software’.

The SPH formulations are developed in the form of integrals in Liu and Liu (2003), and then converted to a discrete particle representation relevant to numerical methods. The description here commences with the interpretation at the discrete particle level.

2.3.1 Particle Approximation

A key feature of the SPH method is its ability to describe a material property at some specific point by the smoothed and weighted average of the value of that property at its neighbouring particles. This would be an integral over the domain of the function for a non-discrete or continuous system. However, herein, it must be represented as a summation of the particle properties, and so is termed the particle approximation.

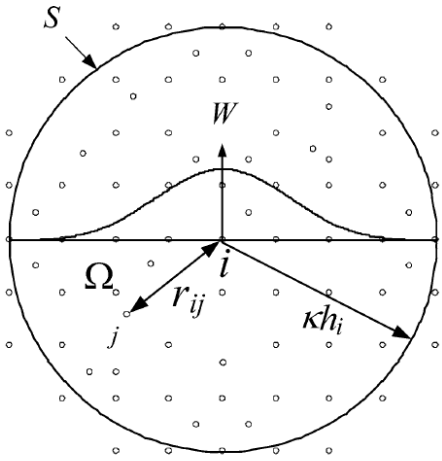

Figure 2-1 Smoothing function, *W*, for particle *i* in a 2-dimensional domain (Liu and Liu 2010).

Referring to Figure 2-1, Ω is the domain of integration and *W* is the smoothing function that is used to approximate field variables at some point *i*. The field variables of all the *j* particles within the cut-off distance of κ*h* from *i* are averaged by the weight of the smoothing function. This cut-off distance is the smoothing length *h* multiplied by an appropriately chosen constant κ. The extent of the domain within the cut-off distance is termed *S*, the support domain of *W*. Note that the magnitude of *W* depends on the distance between the points, and has *h* as a parameter.

The smoothing function W is chosen such that:

a) the integral over the domain is unity, the normalisation condition;
b) as the smoothing length goes to zero, not only will the value of the function approach infinity but its integral is still unity, the delta function property; and
c) the value of the smoothing function at a distance greater than the smoothing length away from the central point, is zero, the compact support condition.

In this way the field variables are represented and calculated by means of the points and the smoothing function. The material itself can also be similarly represented by assigning a volume to each point, and then using the smoothing function to find the local volume based on its neighbours by means of the smoothing function. This will now be used to summarise the characteristic equations.

The representative mass of each particle is the volume of each particle, ΔV_j, multiplied by the density of each particle, ρ_j , for each of the *j* particles within the support domain, as follows:

$$m_j = \Delta V_j . \rho_j \tag{1}$$

The particle approximation for the integral of the function *f(x)* at particle *i* then becomes:

$$f(x) = \sum_{j=1}^{N} f(x_j)\, W(x - x_j, h) \Delta V_j \tag{2}$$

$$= \sum_{j=1}^{N} \frac{m_j}{\rho_j} f(x_j)\, W(x - x_j, h) \tag{3}$$

Using < > to denote a particle approximation, it is then given as:

$$< f(x) > = \sum_{j=1}^{N} \frac{m_j}{\rho_j} f(x_j) . W_{ij} \quad (4)$$

And

$$W_{ij} = W(x_i - x_j, h) \quad (5)$$

Equation (4) is the essence of the SPH technique as it states that the value of a function at particle *i* is approximated by the average of that function at all the particles within the support domain of particle *i*, weighted by the smoothing function.

Derivatives of the function *f(x)* are found by approximation also. They can be expressed as:

$$< \nabla . f(x) > = - \sum_{j=1}^{N} \frac{m_j}{\rho_j} f(x_j) . \nabla W_{ij} \quad (6)$$

Where

$$\nabla_i W_{ij} = \frac{x_i - x_j}{r_{ij}} \frac{\partial W_{ij}}{\partial r_{ij}} = \frac{x_{ij}}{r_{ij}} \frac{\partial W_{ij}}{\partial r_{ij}} \quad (7)$$

Another key feature of the SPH technique is the implication of Equation (6), where it is stated that the derivative of a function at the particle *i* is approximated by the average of the values of the function at all the particles within the support domain of particle *i*, weighted by the gradient of the smoothing function. The important concept to note here is that it is not the derivative of the actual function which is being calculated, but instead is the derivative of the smoothing function. Hence the evaluation of the derivative of an unknown function may be simplified by using the known derivative of the smoothing kernel. Often the smoothing function is chosen such the derivative is easily calculated.

2.3.2 Support Domain and Influence Domain

The previous section used the term *support domain* to describe the region which is considered when determining the local value of a function.

The support domain can be centred somewhere in space that may or may not coincide with the location of one of these particles. It is important to remember that the function values at that point in space are approximated by considering the value of the function at all the particles within the support domain.

Another common term is the *influence domain* which is the region over which a particle exerts its influence.

In contrast to the support domain, the influence domain must be associated with a particle, and thus it represents the domain over which that particle has influence.

Although similar, these two concepts emerge commonly in the literature (Liu and Liu, pp 46 2010) and lead to different ways of coding and implementing the SPH formulations.

2.3.3 Navier-Stokes and Euler Equations

The Navier-Stokes equations are a set of partial differential equations that state the conservation of mass, momentum and energy for a fluid. These are defined in the Lagrangian form consistent with Liu and Liu (2003) as:

Continuity:

$$\frac{D\rho}{Dt} = -\rho \frac{\partial \boldsymbol{v}^{\beta}}{\partial \boldsymbol{x}^{\beta}} \tag{8}$$

Momentum (free of external force):

$$\frac{D\boldsymbol{v}^{\boldsymbol{\alpha}}}{Dt} = \frac{1}{\rho}\frac{\partial \sigma^{\alpha\beta}}{\partial \boldsymbol{x}^{\beta}} \tag{9}$$

Energy:

$$\frac{De}{Dt} = \frac{\sigma^{\alpha\beta}}{\rho}\frac{\partial \boldsymbol{v}^{\alpha}}{\partial \boldsymbol{x}^{\beta}} \tag{10}$$

(The superscripts α and β are used for the coordinate directions, and summation over repeated indices is implied. ν is velocity and χ is displacement in the respective directions.)

The total stress tensor is $\sigma^{\alpha\beta}$ and composed of two parts, one part the isotropic pressure p, and the other, the viscous shear stress due to dynamic viscosity, μ, as follows:

$$\sigma^{\alpha\beta} = -\rho\delta^{\alpha\beta} + \tau^{\alpha\beta} \tag{11a}$$

with,

$$\tau^{\alpha\beta} = \mu\varepsilon^{\alpha\beta} \tag{11b}$$

and,

$$\varepsilon^{\alpha\beta} = \frac{\partial \boldsymbol{v}^{\beta}}{\partial \boldsymbol{x}^{\alpha}} + \frac{\partial \boldsymbol{v}^{\alpha}}{\partial \boldsymbol{x}^{\beta}} - \frac{2}{3}(\nabla.\nu)\delta^{\alpha\beta} \tag{11c}$$

When the viscous component is considered negligible, the Navier-Stokes Equations without viscous term becomes the Euler Equation (Liu and Liu 2003). This affects the energy equation leaving only the pressure component as follows:

$$\frac{De}{Dt} = -\frac{p}{\rho}\frac{\partial \boldsymbol{v}^{\alpha}}{\partial \boldsymbol{x}^{\beta}} \tag{12}$$

In particle approximation form, the expressions are now as follows:

Continuity:

$$\frac{D\rho_i}{Dt} = \sum_{j=1}^{N} m_j \boldsymbol{v}_{ij}^{\beta} \frac{\partial W_{ij}}{\partial x_i^{\beta}} \tag{13}$$

Momentum (after some manipulation, refer Liu and Liu 2003):

$$\frac{D\boldsymbol{v}_i^{\boldsymbol{\alpha}}}{Dt} = \sum_{j=1}^{N} m_j \left(\frac{p_i}{\rho_i^2} + \frac{p_j}{\rho_j^2}\right)\frac{\partial W_{ij}}{\partial \boldsymbol{x}_i^{\alpha}} \tag{14}$$

Energy:

$$\frac{De}{Dt} = \frac{1}{2}\sum_{j=1}^{N} m_j \left(\frac{p_i}{\rho_i^2} + \frac{p_j}{\rho_j^2}\right) \boldsymbol{v}_{ij}^{\beta} \frac{\partial W_{ij}}{\partial \boldsymbol{x}_i^{\beta}} \tag{15}$$

Where

$$\boldsymbol{v}_{ij} = \boldsymbol{v}_i - \boldsymbol{v}_j \tag{16}$$

Liu and Liu (2003) note that the removal of the viscosity term in these equations describes an inviscid fluid, with the resulting equations then becoming simply the Euler equations. It should be noted that the software used for this research solved the Euler equations.

Liu and Liu (2010) state that many of the early algorithms did not conserve linear and angular momentum. The momentum equation stated here in equation 14, and that employed in the software used for this research, does conserve momentum as the smoothing kernel is symmetric with respect to interchange of the particle index.

2.3.4 Artificial Viscosity

Artificial viscosity is a numerical term introduced originally to control the calculation problems associated with shock waves (Monaghan and Gingold 1983). The problem was that the shock front was typically very much smaller than the particle size, and so instabilities resulted. To overcome this, the effective width of the shock front was stretched by increasing the apparent viscosity.

For the Euler Equation where there is no real viscosity term, the velocity of the particles is modified slightly by the addition of the artificial viscosity term to the momentum equation as follows, where Π_{ij} is the artificial viscosity term:

$$\frac{D\boldsymbol{v}_i^{\alpha}}{Dt} = -\sum_{j=1}^{N} m_{\mathrm{j}} \left(\frac{p_i}{\rho_i^2} + \frac{p_j}{\rho_j^2} + \Pi_{ij}\right) \frac{\partial W_{ij}}{\partial \boldsymbol{x}_i^{\alpha}} \tag{17}$$

The most common form of the artificial viscosity is that proposed by Monaghan (1985), and aptly called the Monaghan artificial viscosity. The formulation is as follows:

$$\Pi_{ij} = \frac{2}{\rho_i + \rho_j}\left(-\alpha \frac{c_i + c_j}{2} \mu_{ij} + \beta \mu_{ij}^2\right) \tag{18}$$

Where:

$$\mu_{ij} = \begin{cases} \frac{1}{2}(h_i + h_j)\frac{(v_i - v_j)\cdot(r_i - r_j)}{|r_i - r_j|^2 + \eta^2}, & (v_i - v_j)\cdot(r_i - r_j) < 0 \\ 0, & (v_i - v_j)\cdot(r_i - r_j) \geq 0 \end{cases}$$

Where η is a factor to prevent numerical divergences when two particles are approaching each other, *c* is the speed of sound, *h* is the smoothing length and *v* is the velocity particle vector.

In Equation (18) the α and β terms are called the alpha and beta constants of the artificial viscosity. Monaghan, Thompson and Hourigan (1994) state that these two terms control the shear and bulk viscosity respectively, and that the shear viscosity is approximately equal to the product of α, the smoothing length and the speed of sound.

2.3.5 Equation of State

Throughout this research, one variant of the many modifications of the original Murnaghan equation of state (Murnaghan 1944) has been used. The form used states that the pressure p is given by:

$$p = p_0 + B\left(\left(\frac{\rho}{\rho_0}\right)^{\gamma} - 1\right) \tag{19}$$

Specifically, ρ/ρ_0 is the ratio of the current mass density to the initial mass density, and γ is a constant equal to 7 for most applications (Monaghan, Thompson and Hourigan 1994). B is the bulk modulus of the material and is often chosen to produce a sound speed at least 10 times higher than the maximum (expected) fluid velocity. This implies that the Mach number of the flow will remain less than 0.1 which limits the density variation to about 1%, which is deemed to be a pragmatically acceptably density fluctuation that maintains the quasi-incompressible nature of the flow regime (Monaghan, Thompson and Hourigan 1994). The Mach number also influences the time step (see Section 2.3.9) and hence the overall computational effort required to complete a simulation of given duration, and so this determination of the minimal Mach number to retain essential flow characteristics is a convenient tool for reducing computation time.

A cut-off pressure is included in the implementation of this equation of state in the software as a simple cavitation model. In this role when the pressure of the material equals that of the cut-off pressure, the material strength is reduced to zero.

Another commonly used equation of state is the polynomial equation of state:

$$p = C_0 + C_1\mu + C_2\mu^2 + C_3\mu^3 + (C_4 + C_5\mu + C_6\mu^2)E_i \tag{20}$$

Where E_i is the internal energy and C_0 to C_6 are material constants and the terms $C_2\mu^2$ and $C_6\mu^2$ are set to zero if :

$$\mu < 0\ ;\ \mu + 1 = \rho/\rho_0$$

Toso (2009) studied the impact of deformable structures on water using SPH to represent the water, and found very similar simulation results between these two equations of state when similar properties were used in each. Toso (2090) also reported that good correlation with experimental results was maintained with a significant reduction in computation time when the speed of sound was reduced in the Murnaghan equation following the guidelines of Monaghan, Thomson and Hourigan (1994), however the correlation between experiment and prediction by SPH deteriorated when the speed of sound was reduced further.

For simulations of benign events, such as a ship moving through waves (without excessive slamming), the duration of the simulation may need to proceed for minutes of real time compared to fractions of a second for an impact event. Consequently the Murnaghan

equation of state is preferred for its ability to have a larger time-step and has thus been chosen for this research.

2.3.6 Density Re-Initialisation

Density is commonly approximated by the particle approximation method. Density is vital for calculations in fluid dynamics, as many of the equations of state used to define a fluid contain a density term (Liu and Liu 2003).

A representation of the density in particle form is:

$$\rho_i = \sum_{j=1}^{N} m_j W_{ij} \tag{21}$$

This definition encounters problems when the particle is close to the domain boundary, as the cut-off distance of the smoothing function will extend beyond the domain, effectively including a partially null volume. The consequence of this is the calculation for the density will be incorrect.

As noted in Liu and Liu (2010), a common way to overcome this resulting error is to normalise the smoothing function at the boundary by the sum of the smoothing function truncated to the domain limits. Recall from Section 2.3.1 that one of the features of the smoothing function is that the integral over its support domain is unity. Hence, if the integral is not unity, then the result is scaled accordingly. This preserves density at the boundaries.

Fluctuations in density are commonly seen in various SPH formulations (Rogers et al 2009). A common technique that overcomes these fluctuations is the re-initialisation of the density field using a Shepard filter (Shepard 1968). Using this filter, which is an interpolation function, the density is periodically reinitialised as:

$$\widetilde{\rho_i} = \sum_{j=1}^{N} m_j \widetilde{W_{ij}} \tag{22}$$

Where:

$$\widetilde{W_{ij}} = \frac{W_{ij}}{\sum_j \frac{m_j}{\rho_j} W_{ij}} \tag{23}$$

Equations 22 and 23 state that the individual density of some particle *i* is reinitialised to the total average density across the domain. Such re-initialisations done regularly during the time-frame in question leads to smoother density gradients, which in turn then leads to smoother pressure gradients throughout the domain in question. The default interval for density re-initialisation in the software used here was every 20 time-steps.

2.3.7 Anti-Crossing Parameter

The anti-crossing parameter is a modifier to the particle displacement that assists in maintaining order amongst particles in high-speed flow and is particularly useful for free-surface problems (Monaghan 1994). Termed “XSPH”, use of the parameter produces more stable simulations and prevent particles from passing through one another, by modifying the

displacement of particular particles such that their velocity is closer to the average within the smoothing length of that particular particle (PAM-CRASH 2009). The particles displacement is modified, conserving momentum, according to:

$$\frac{dr_i}{dt} = v_i + \varepsilon \sum_j \frac{m_j(v_j - v_i)}{\rho_{ij}} W_{ij} \quad (24)$$

Specifically, ε is a factor between 0 and 1, with a value of 0.5 found to work well for many scenarios (Monaghan, Thompson and Hourigan, 1994), and ρ_{ij} is the density of particle j relative to particle i.

2.3.8 Smoothing Length

The smoothing length is a dimension that, in conjunction with the parameter κ described earlier, determines the cut-off distance of the compact support of the smoothing function. The larger the smoothing length, then the larger that the influence domain of a particle will be, producing more gradual changes of parameters with distance, thus making for a more viscous-like behaviour, in the case of fluid motion.

Formulations for compressible fluids can employ a variable smoothing length that aims to maintain a constant number of neighbours within the calculation, thus ensuring effective smoothing behaviour of the material properties. For a quasi-incompressible fluid however, a constant value may be used (Monaghan, Thompson and Hourigan 1994).

2.3.9 Time step

The behaviour of the fluid over time will necessarily involve some form of time integral. The increment in time used therein between consecutive calculations is termed the time step. The original SPH formulations from 1977 of Lucy, Monaghan and Gingold did not include a discussion of time step, but this is an important, indeed a fundamental and critical, feature of any numerical solution. The rules shown here are based on the requirements for a stable implementation of any time integration within the software used for this research.

The time step must be such that:

a) a shockwave moving through a material does not traverse more than one element in a time step; and
b) moving SPH particles do not pass through each other in a time step.

The first requirement is fundamental to dynamic analysis by ensuring that all transient data relevant to that shockwave is both captured and maintained in the calculation at every time-step. The second ensures that all collisions are captured by ensuring the distance traversed by any two moving particles is less than the distance between the two, such that the smoothing rules fundamental to the SPH technique can take effect.

For fluids, a shockwave travels at the speed of sound in the material, given by:

$$c = \sqrt{\frac{\partial p}{\partial \rho}} \tag{25}$$

The critical distance is the smoothing length, and hence the critical time step Δt_c is defined as:

$$\Delta t_c = \frac{h_c}{c} \tag{26}$$

A more accurate determination of the critical time step considers also the artificial viscosity parameters and particle velocities, as defined in Lombardi et al (1999) as;

$$\Delta t_{SPH} = \min_i \left(\frac{h_i}{c_i + 1.2\alpha c_i + 1.2\beta \, \mathrm{Max_j} |\mu_{ij}|} \right) \tag{27}$$

Where:

c_i = speed of sound at particle *i*
μ_{ij} = as defined for equation (18)

The speed of particles approaching one another also has to be considered to ensure that no collisions occur within a time-step. This calculation is similar to Equation (26) in that the smoothing length is the critical distance, except the particle velocity is used in place of the speed of sound. This time step is usually orders of magnitude lower than the time step determined by shockwave rule, as the particles in fluid motion are usually travelling at much less than sonic speeds.

The software employed for this research also applies a Courant-like condition to the smallest time step to ensure convergence and avoid instabilities (PAM-CRASH 2009). This involves multiplying the smallest time-step by a factor typically less than unity.

As both the material properties, the smoothing length and the minimum distance between any two particles may change with time, the time-step will also change throughout a simulation. In the software used here, safeguards to ensure a minimum time step can be defined by the user, or similarly the simulation may cease if the time step becomes less than some predefined value.

In summary, the time step for a group of SPH particles is determined by:

- the smoothing length of the SPH particles, and
- a Courant-like factor, and
- the speed of sound in the material the SPH particle is representing, or
- the maximum speed of the particles.

2.4 *Rigid Bodies in SPH*

The SPH technique has been applied to many fluid and solid mechanics applications (Liu and Liu 2003). Lobovsky and Groenenboom (2009) have demonstrated that both solid and fluid materials can co-exist when described by SPH techniques, i.e. the equations can handle both materials at the same time in the same solution routine.

For studies of fluids and rigid bodies, a rigid body being a body for analysis purposes that is considered perfectly rigid, the rigid body is typically made from SPH particles that are tied together to represent the shape of the rigid body, as in Figure 2-2 from Gonzales et al (2006). Note that in Figure 2-2 the SPH particles are sufficiently small compared to the ship so as to be not recognisable individually, but visible as a textured continuum.

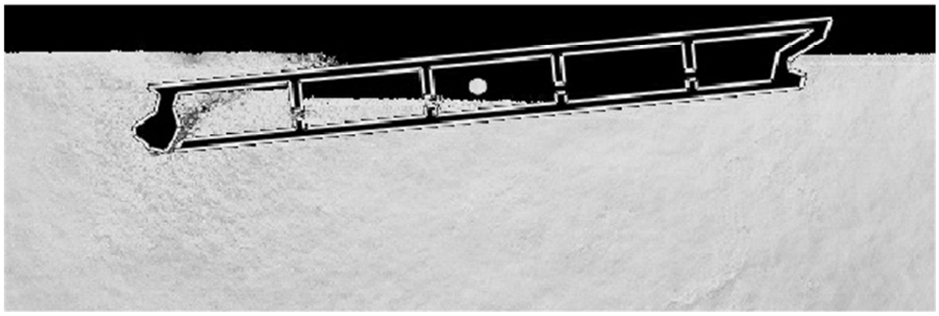

Figure 2-2. Rigid bodies such as ships can be defined by a set of connected SPH particles. (Gonzales et al 2006)

For three-dimensional shapes, such as ships, their representation by discrete particles is tedious to generate, and requires quite small particles to accurately reveal the features. A much more convenient way to represent the ship is to use a series of connected panels and stringers and frames as would commonly be used for the structural analysis of that ship by the Finite Element Method (FEM). Often this type of description of the hull already exists, or is very easily exported from ship hull design software. Hence, it would be convenient to use this panel model of the hull directly in an SPH solver.

Johnson et al (2001), Ubels et al (2003), Cartwright et al (2004a and 2004b), Lobovsky and Groenboom (2009), and Vignevic and Campbell (2009a and 2009b), demonstrate software that include solvers for both SPH and finite elements within the one package. Typically, the fluid behaviour is modelled by SPH, with the structural behaviour modelled by the FEM. The software employs a time step that considers both the SPH and FEM requirements enabling a stable solution for the fluid and the structure to be solved at each time step, and enables interaction of the SPH particles with the finite elements. This is in contrast to the use of two independent stand-alone solvers, one for the fluid and one for the structure, which then require an exchange of data between the two solvers at periodic intervals to achieve full fluid-structure interaction (FSI).

Once finite elements are included in the solver, the existing library of robust finite element material models, including non-linear material definitions and material failure definitions, are able to be employed simultaneously with the SPH analysis (PAM-CRASH 2009). Combining structurally deformable materials with fluids enables complex problems such as hydro-elastic analyses to be performed within the one software package (Toso 2009, Lobovsky and Groenenboom 2009).

2.5 *Interaction of SPH with Finite Elements*

The interaction of the SPH particles and finite elements is controlled by a sliding contact interface, allowing sliding interaction, but not penetration.

Bourago and Kukudzhanov (2005) present a summary of sliding contact interface techniques. In summary, such interfaces enable elements not connected by a mesh to slide past one another without penetration.

Many of these sliding contacts use an artificially applied penalty force to prevent elements from sliding through one another. A development of this sliding contact to cater for the discrete particles interacting with shell-type finite elements is described in Lobovsky and Groenenboom (2009), and is similar to the algorithm employed in this research (PAM-CRASH, 2009). A review of contact algorithms for use between finite elements and boundary conditions is presented in Groenenboom (2011).

The penalty force sliding contact algorithm performs a test for SPH particles that have penetrated within a predefined distance of the shell element called the "contact thickness". Any particles that are within this contact thickness have a penalty force applied to them that is proportional (user-defined to be linear (default) or non-linear) to the depth of penetration. The force is normal to the face of the shell element face and pushes the particle away from the shell element. Particles further away than the contact thickness experience no force from the contact. As the penalty force is proportional to the penetration depth, the sliding contact acts like a spring, such that for a particle that is continually forced against the shell, say due to hydrostatic pressure on the bottom of a ship hull, equilibrium is only achieved with a small degree of penetration. Typically the penetrations for equilibrium are very small, a fraction of a percent of the contact thickness, so that the penetration is negligible on the scale of the particles and the finite element.

Sliding interfaces may also include friction laws. The software used for this research includes a variety of friction laws (PAM-CRASH, 2009), ranging from classical Coulomb friction, friction dependent on either pressure or velocity or both, friction described by standard mathematical functions, through to directionally dependent friction and even user-defined friction models. This research used effectively zero friction between the finite elements by selecting the default Coulomb friction law and then specifying a coefficient of friction of zero. This approach may need to be reconsidered if viscous effects such as drag on the body are to be considered.

2.6 *Symmetry Conditions*

Symmetry is an option available along the major global axes through the use of 'ghost' particles in the software used for this research. When symmetry is selected, a ghost particle is created across the symmetry plane for each real particle within a smoothing length of the symmetry plane. The ghost particles are assigned scalar properties equal to the real particle and mirrored vector properties to ensure conservation across the symmetry plane. This treatment improves the behaviour of the real particles at the border by overcoming issues of the smoothing kernel introducing errors by extending beyond the computational domain into a region of no particles (Liu and Liu 2010).

2.7 *Alternative Momentum Equations*

The scenarios studied in this research considered that the presence of air on the free surface of the water is negligible. Consequently the air has not been included in the SPH simulations.

For situations where the presence of air is important, such as accounting for the cushioning effects of air in a slamming event between a structure and water (Kalis 2007), the momentum equation of Equation (14) does not work well. The reason being the density of the fluids becomes smeared at density inhomogeneities, thus giving spurious results (Liu and Liu 2003). The alternative momentum equation is more suitable for these situations as follows:

$$\frac{D\boldsymbol{v}_i^{\alpha}}{Dt} = \sum_{j=1}^{N} m_j \left(\frac{p_i + p_j}{\rho_i \cdot \rho_j}\right) \frac{\partial W_{ij}}{\partial \boldsymbol{x}_i^{\alpha}} \tag{28}$$

2.8 *Scaling of SPH Particles*

In numerical simulations it is often necessary to use SPH particles of different size. Reasons for this could be any of the following:

a) the domain size is made larger but the number of SPH particles need to remain constant for reasons of CPU effort, or
b) a material calibration that includes the SPH parameter set was performed at one size SPH particle, but a different SPH size has to be used in an application, possibly due to a)
c) the response of a ship model in flooding requires fine SPH, yet the same ship model with forward motion in large waves will also be conducted requiring much larger particles to maintain a manageable model size (number of SPH particles).

To ensure the SPH particles have similar behaviour in numerical models of different scale, the SPH parameters must be scaled according to the factors listed in Table 2-1. This table provides scaling factors according to Froude scaling.

Table 2-1 Scale factors for SPH Models.

Parameter	**Scale factor**
Linear Geometric scale	S
Bulk Modulus of Fluid	S
Alpha coefficient of artificial viscosity, α_{Π}	$1/(S^{1.5})$
Simulation time	$\sqrt{(S)}$
Timestep	$\sqrt{(S)}$

Note that the α term is a factor that has no units, however it requires scaling as it is used in the artificial viscosity expression (Equation 18) that consists of other parameters of dimension that do not scale according to Froude scaling. The scale law quoted here for α maintains viscosity equivalence at the new SPH particle spacing.

2.9 *Key SPH Parameters*

For the Murnaghan equation of state (Equation 19) that has been used throughout this research, the key SPH parameters that have been used throughout this work are given in Table 2-2.

Table 2-2 Typical values of key SPH parameters.

Parameter	Description	Typical Value
Smoothing Kernel Type	Smoothing function	Cubic Spline
Smoothing Length to Radius Ratio	Defines the sphere of influence of a particle	1.6 – 2.5 with a value of 1.8 used in this research.
Artificial Viscosity Terms: Alpha Beta	 Controls shear viscosity Controls bulk viscosity	 0.02 for fluids
Anti-Crossing Force	Modifies particle velocities and helps with stability	0.02
Bulk Modulus	Influences the Mach number and hence the time step of the simulation	Up to 2.2e9 Pa for water, but typically 2.2e6 Pa for benign waves.
Density Re-initialisation	Reduces density fluctuations in the domain	Every 20 time steps (default value).

The values in Table 2-2 are based on the sensitivity studies performed in the same software (Kallis 2007), with small changes based on the author's own experience.

As noted in Section 2.3.9, the bulk modulus of the material influences the speed of sound in the material, and consequently the time-step. For a given duration of event that is to be simulated, the number of time-steps will influence the time to complete the simulation (as does the number of particles in the calculations). Typically it is desirable to complete the calculations as quickly as possible, so having as large a time-step as possible is of interest to provide efficient solutions.

Monaghan (1994) states that if the speed of sound is 10x that of the highest anticipated speed of the particles in the model, then the behaviour of the fluid remains stable and is suitable for the simulation of the bulk flow of the fluid. Hence this rule allows a reduced Bulk modulus to be determined based on anticipated velocities, that will allow a large time-step and the rapid completion of the calculations.

2.10 *Summary of Theory and Implementation*

Mesh-free methods are highly customisable, such that many of the implementations discussed in the literature have been developed for particular applications within the field of fluid or solid mechanics problems.

This chapter has introduced the most common SPH mesh-free formulisations for fluids. Where relevant, detail has been provided on the specific implementation in the software used for this research.

Mesh-free techniques, including SPH as used within this work, are not as mature as the more traditional Finite Difference (FD), Finite Volume (FV) or FEM techniques for fluid and structural mechanics problems. For this reason there is still much development being reported in the literature in the use of these methods for seemingly common applications such as water flow.

The inclusion of finite elements with mesh-free solvers employing sliding algorithms is a powerful capability that conveniently allows structural components to be included in an analysis involving fluids. This has enabled complete fluid-structure interaction to be analysed, including the study of hydro-elastic behaviour (Lobovsky and Groenenboom 2009, Toso 2009).

3 Software

The software used throughout this study has been the commercial code PAM-CRASH from ESI Group, France (PAM-CRASH, 2009). The use of the software has been made available through the Australian distributor Pacific Engineering Systems International, Pty Ltd in Sydney (trading as Pacific ESI Pty Ltd.)

3.1 *PAM-CRASH*

PAM-CRASH is a general purpose finite element code with an explicit solver optimised for dynamic, strongly non-linear structural mechanics. PAM-CRASH contains finite element formulations for thin shells, solid elements, membranes and beams with material models with plasticity and failure for metals, plastics, rubbers, foams and composites. Robust contact algorithms are available in the code enabling the modelling of dynamic contact between various parts within a model. A Smoothed Particle Hydrodynamics (SPH) solver is incorporated into the explicit PAM-CRASH solver, enabling both finite elements and SPH elements to be used and solved simultaneously in the same model. The solver is able to run on multiple processors to achieve reduced computation times.

The origins of the SPH solver within PAM-CRASH are in commercial work for hyper-velocity debris impact analysis on spacecraft and ballistic protection in the mid 1990s (Groenenboom 1997) In the late 1990s the SPH material laws were extended to include fluid laws for the application of bird-strike, fuel sloshing and explosives (PAM-CRASH, 2001).

Continual development of PAM-CRASH focuses on the robust implementation of advances in the field from public literature, ensuring compatibility with the existing software and material models. The direction of the software development is driven by customers who fund specific development, and topic-based research projects for which funding is received on a competitive basis.

The features of PAM-CRASH SPH features are listed in Table 3-1. (PAM-CRASH 2009).

Pre- and Post processing of the PAM-CRASH files has been performed using the Visual suite of software also from ESI Group (Visual, 2009).

Table 3.1 PAM-CRASH SPH Features

Material models available for SPH	Murnaghan Equation of State (Equation 19) Polynomial Equation of State (Equation 20) Elasto-plastic with damage JWL Explosive Johnson-Cook
Kernel functions	W4 B-Spline Q-Gaussian Quartic Quadratic Cubic Quartic Spline
Smoothing Lengths options	Constant or variable
Artificial viscosity in tension	Flag to turn on or off
Symmetry planes by ghost particles	Aligned to global coord axis
Momentum formalism options	Options for co-existence of homogeneous or inhomogeneous material
Density re-initialisation	By use of a Shepherd filter at user-defined intervals
Interaction with finite elements	Both deformable and rigid shell and solid finite elements. Interaction through contact interfaces or tied interfaces.

3.2 *Previous Ship-oriented Applications of PAM-CRASH*

PAM-CRASH has been used commercially to study ship-ship and ship-infrastructure collisions. Much of this work has not been published due to commercial confidentiality requests, but a few reports are available such as a report on a ship colliding with a compliant wharf structure (Kisielewicz et al 1993), and predictions of damage to colliding river barges (Grabowiecki et al 2004). These studies focused mainly on non-linear finite element behaviour in the prediction of damage and puncture of the hulls. SPH was not used in this work.

Some of the earliest papers in the public domain referencing water and waves modelled with SPH and floating structures modelled with finite elements are the works by the author of this thesis with various colleagues.

Cartwright et al 2004a demonstrated severe non-linear motions in six degrees of freedom for a destroyer, a wave-piercing catamaran and a trimaran moving forward into an oblique wave system. The wake in calm water from a wave-piercing catamaran at two different speeds in shallow water as predicted by SPH was also presented. Cartwright et al 2004b demonstrated in greater detail the response of the wave-piercing catamaran in severe oblique waves, including revealing impact forces from wave slamming.

The response of a generic naval Landing Helicopter Dock (LHD) ship was predicted at one wave length and two wave heights using PAM-CRASH (Cartwright et al 2006a). Of greater interest was the prediction of the response of a landing craft within the landing dock. No correlation to model data was made, however, as the response of the landing craft within the dock is particularly difficult to model (Bass et al 2005), the ability to reveal the motion of the landing craft within the well dock from the simulation using SPH was considered a useful outcome.

PAM-CRASH was used to demonstrate the response of a single chine powerboat using SPH in calm water as it transitions from rest through to an equilibrium planing condition at high speed (Cartwright et al 2006b).

Although many of these papers by Cartwright et al did not validate the predictions, the presented numerical simulation concepts were novel at the time.

Validated results of structures in water modelled by SPH based on the concepts presented by the 2006 publications by Cartwright et al include the study of a planning vessel in water (Overpelt 2007) and the predictions of the motions of a free-fall emergency lifeboat (Kalis 2007). Both these reports concluded that correct trends were predicted by the SPH method, however the results were found to be sensitive to the numerical SPH parameters chosen, and it was commented that the role of the SPH numerical parameters was not well understood.

Overpelt et al (2006) took the work of Cartwright et al (2006a) further and correlated predictions from SPH with actual test measurements. They found favourable correlation for the LHD response and the landing craft within the well dock for the sea states examined.

The work of Kalis (2007) was taken further in Groenenboom (2008), to predict the kinematics of a lifeboat when dropped into water modelled using SPH with good correlation.

4 Hydrostatics

4.1 *Introduction*

The concept of hydrostatics is so fundamental to naval architecture that it may seem strange to include a section on it in this thesis.

There are two reasons this section is necessary. The first is that the SPH technique has more commonly been applied to dynamic events than static systems, due to its inherent ability to handle splash and violent free surface events. In hydrostatics the interest is in the static location of the fluid surface relative to the ship features. This is a novel application for the SPH technique, and so a brief study on static events is warranted.

The second issue is that the SPH technique describes a continuum, in this case water, by a set of nodal points that each identify the centre of a discrete volume of water. The location of the water surface is not inherently obvious. For hydrostatics there is a need to accurately locate the surface of the water both adjacent to the air and adjacent to the floating structure, particularly for future studies that may investigate flow into and out of a damaged structure.

This section establishes some rules to address these issues that are unique to the mesh-free methods.

These studies in hydrodynamics have been considered as a subset of the larger problem consisting of a tank sufficient to develop a wave train of many wavelengths for a ship to traverse. Consequently the simulations here may appear to have low numbers of large particles. The longer term aim is to use these same sized particles in the larger tank to maintain a realistic computational effort within the realms of this research. In contrast, the use of a large number of smaller particles in the hydrostatic studies may produce less errors but the findings would not be relevant to a larger tank as the number of particles required would deem the problem size impractical.

4.2 *Buoyancy Force on a Submerged Body.*

4.2.1 2D Studies in a 3D world

The finite element program employed for this research uses a three-dimensional coordinate system. Two-dimensional (2D) studies were conducted in a three-dimensional (3D) space by placing restraints on all entities such that they were allowed to move only in the plane of interest.

The SPH particles used in this research were represented by a single point, which is compatible with a 2D environment. This is shown in Figure 4-1 where the fluid is represented by the sum of all the single dots, each dot being a SPH particle in the 2D plane.

Numerically each SPH particle has a volume associated with it, and is consequently a 3D entity. In the 2D simulations, the volume is a circular cylinder in the 3D environment, of length equivalent to the SPH spacing and with all forces restrained to the 2D plane.

The kernel is usually defined to sum over a spherical volume, centred at a specific particle and applying weighting factors to all other particles within the smoothing length. For a 2D simulation the kernel will only find particles within a plane and so the weighting factors must be modified to ensure the sum of the kernel is still is unity. This modification to the kernel was achieved through a 'switch' in the software that selects the 2D weighting factors instead of the default 3D factors. This switch enables studies in plane strain to be undertaken.

Geometric shapes such as submerged bodies or a holding tank to contain the fluid would suffice as bar elements in a 2D environment. To reliably interact with the 3D volume of the SPH particles, the 2D entities were replaced with 3D shell elements perpendicular to the plane of interest, of depth into the plane approximately equivalent to the diameter of the SPH volume. This is merely a 'numerical etiquette' particular to the software used to ensure that the contact algorithms work efficiently. Again referring to Figure 4-1, the solid lines represent impassable boundaries to the SPH particles, and consequently have a dimension in the direction normal to the plane of the particles such that they are also 3D entities.

4.2.2 Submerged Objects in 2D

The first study investigated the force responses associated with a submerged square, as shown in Figure 4-1. Due to the 2D/3D nature of the code, the forces were reacted only in the plane of the square, and the 2D square was actually a thin 3D box. The thin box was rigid and held at constant depth below the surface to enable the forces acting on it to be examined to understand how the buoyancy forces are generated using the SPH technique.

The forces acting on a stationary submerged box are the buoyancy force of the displaced fluid and the weight of the box. In the studies here the box was held at a prescribed location in space by a displacement boundary condition that perfectly reacts the weight of the box. The only remaining forces acting on the box were those due to the SPH particles.

Penetration of the box by the SPH particles was prevented by a 'contact interface', as introduced in Chapter 2. The contact interface is a numerical tool that allows two materials to come into contact with each other but prevents them from passing through each other in an un-physical way. In this way the water remains on the outside of the box, and the box displaces the water. The net contact interface force is the net force acting on the box due to the SPH particles. For a stationary box in still water, the net contact force is the buoyancy force.

To conduct these tests, a rigid square box shape (in two dimensions) was located above the water, and then forcibly moved to a location where it was fully submerged. The movement of the box was controlled by a displacement boundary condition, that is, a simple function that prescribed the motion of the box with time. The box sides were oriented at 45 degrees to the horizontal, to produce a less-violent disturbance of the free-surface – i.e. if the flat face was presented to the water surface it would create a larger impact event resulting in greater splash and waves that would require more time to dissipate before reaching equilibrium conditions.

The initial and final states for one case of the submerged box are shown in Figure 4-1. In the left image of Figure 4-1 hydrostatic pressures have not been developed, as this was the initial

conditions of the simulation. As gravity was applied to the model and the SPH particles settled a uniform hydrostatic pressure develops. The approach adopted here averaged the hydrostatic pressures over the total surface of the submerged box, and thus the net buoyant force was reported, as shown by the contact interface force in Figure 4-2. The unfiltered contact force is quite noisy in this example, caused by the movement of the SPH particles as they re-arrange themselves into an equilibrium position, each one bouncing off the submerged box. A moving average of 100 samples was used to smooth the force curve to the smooth line shown.

At time zero in Figure 4-2 the box commenced the simulation above the water, and the water began to settle under gravity. The water was largely settled at time of 1 second when the box touched the water and the first contact force is registered. The reaction force of the water on the box increased to a maximum value when the box was fully submerged and moving, then settled to a near-constant value when the vertical motion ceased. The maximum reaction force was the sum of the buoyancy and all hydrodynamic forces (such as drag) acting on the box. The box was decelerated smoothly until stopped and then held at that depth for a suitable length of time to allow the water to settle. For the 2D studies on submerged bodies a simulation time of 20 seconds was found to give a sufficiently steady buoyancy force.

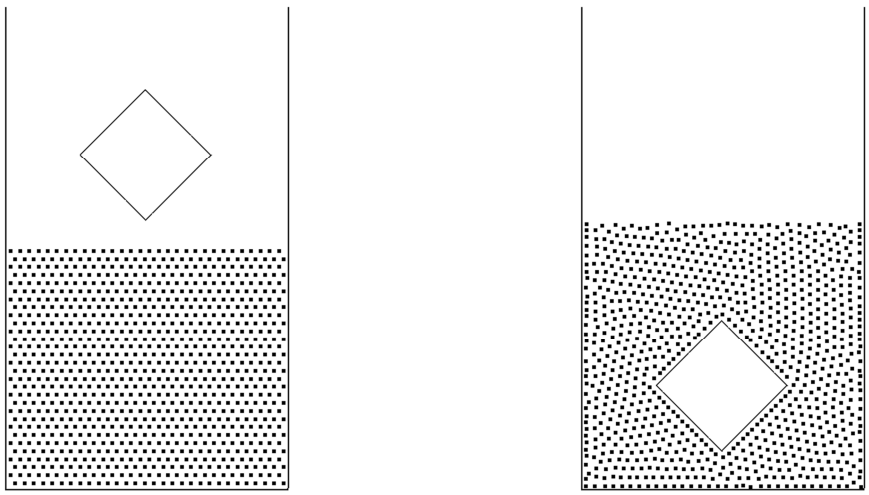

Figure 4-1. Initial and final states for the FE model of a submerged box.

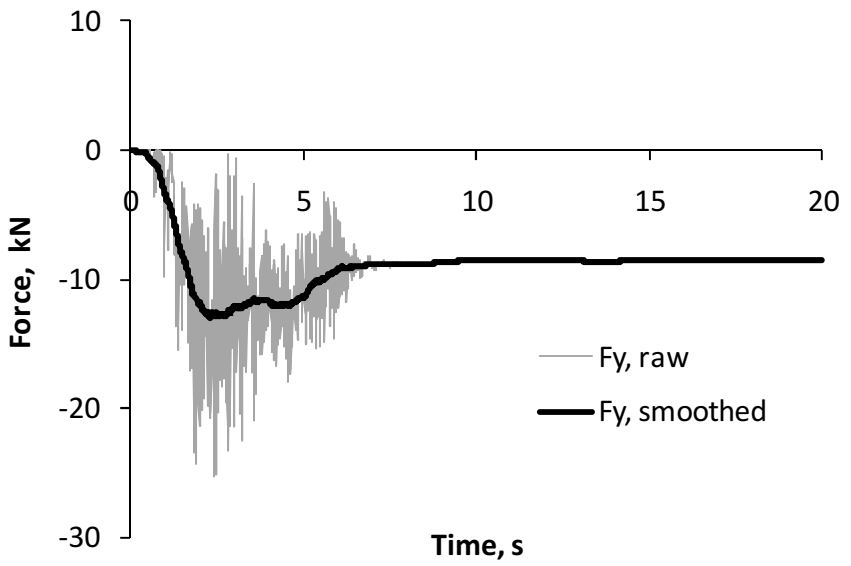

Figure 4-2. Buoyancy force acting on the submerged box. Raw and Moving Average results.

In this model the submerged square was 2m x 2m. The SPH particles were on 0.2m centres. In line with the 3D representation of the 2D model, the FE model had a finite thickness into the page, so that the walls of the box were shell elements with a finite area. The thickness into the page was set to a unit thickness based on the SPH particle spacing.

The SPH parameters used to generate the figures of Figure 4-4 are listed in Table 4-1.

Table 4-1 SPH Parameters used for Buoyancy Studies with 0.2m SPH.

Parameter	Value
Smoothing length/radius	1.6
Smoothing lengths : min , max	0.0001 , 0.08
Artificial viscosity terms : α , β	0.02 , 0.02
Anti-crossing force parameter	0.02
Bulk modulus	2.2e8 Pa
Shepard density re-initialisation	Every 20 cycles

The properties listed in Table 4-1 with 0.2m SPH centres gave a nominal time-step of 120 microseconds. Force output were written to the output file at 100 Hz.

The final buoyant force in this example was 8454N, which is more than the theoretical value from the Archimedes principle of 7848N. The reason for this is that the hole in the water in which the box is sitting is not quite the right size – it is too large, and hence the box is displacing more water than it should. Similarly, the water level in the tank will have risen by the volume displaced.

Figure 4-3 illustrates in detail a box submerged in SPH particles. The main dimensions are shown. The box has side length 'L'. The SPH particles are dispersed on a nominal centre –

centre distance of ‘s’. The distance between the SPH particles and the surface of the submerged box is the contact thickness and defined as ‘h_c’.

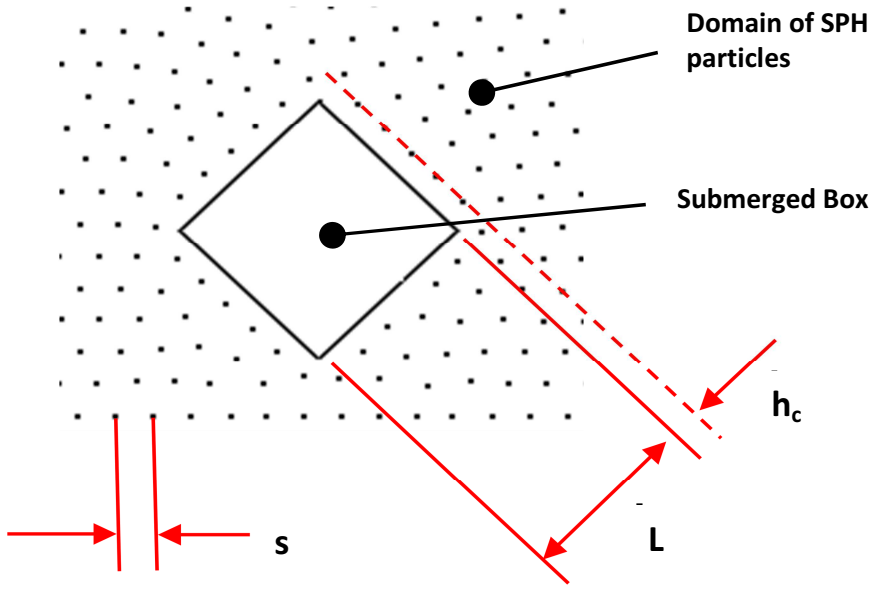

Figure 4-3. Dimensions for the buoyancy tests.

Typically the contact distance, h_c, will be less than or equal to the SPH spacing. As the SPH spacing varies, then so too should the contact distance. h_c/s is a non-dimensional variable used here to describe contact distance effects.

Trials were conducted with different values of h_c and different sized particles to find the value of the contact distance parameter that produced the buoyancy force closest to that obtained using Archimedes principle.

Figure 4-4 shows the error in buoyancy force as a function of the h_c/s ratio. Three different SPH spacings were used, namely L/s of 5, 10, 20 and 100. The error was the difference between the measured buoyancy force and the actual buoyancy force, expressed as a percentage of the theoretical buoyancy force.

In Figure 4-4, the curve for the L/s value of 5 has the steepest slope, indicating that the error in the buoyancy force is sensitive to h_c/s ratio. It is also not very smooth. An L/s of 5 means that there were only 5 particles along the length of the box, which was a very coarse model.

The curve for the L/s value of 10 in Figure 4-4 is much less steep and has less scatter than the curve for L/s of 5. The curve for the L/s value of 100 has the least gradient and is the most linear.

From Figure 4-4 the value of h_c that corresponds to the most accurate buoyancy force is when the ratio of h_c /s (contact distance to particle spacing) is about 0.6 for the square shape studied here.

To have only five SPH particles along the length of a moving body is an absurdly coarse model, but demonstrates some interesting behaviours that will be present no matter how small the particles. The error curve for the buoyancy force is not smooth with changing contact distance, h_c. Intuitively the correct value of h_c is expected to be about 0.5, that is when the SPH particles are at one radius away from the surface of the submerged body, as this is their normal spacing away from adjacent SPH particles. The error curve agrees with this in principle in that the error is least around the value of 0.5 for the particle sizes studied, and significantly away from this value the error is large, i.e. at $h_c = 0$ and $h_c = 1$. The deviation from a straight-line relationship is an interesting feature of the curve.

A likely explanation for the not-quite straight-line behaviour of the curves in Figure 4-4 is the packing of SPH particles against the surface of the body. If the SPH particles pack uniformly against the body, for example if the body length is an exact integral number of SPH particles in length, a particular value of h_c will give the correct buoyant force. If the particles do not pack uniformly against the submerged body, say there is one half an SPH particle too many to fit uniformly, then the particles will not pack uniformly and the particles will not be in their most dense arrangement. Consequently a local variation of fluid density will result and a different value of h_c may be needed to displace a bit more fluid to ensure the exact buoyant force.

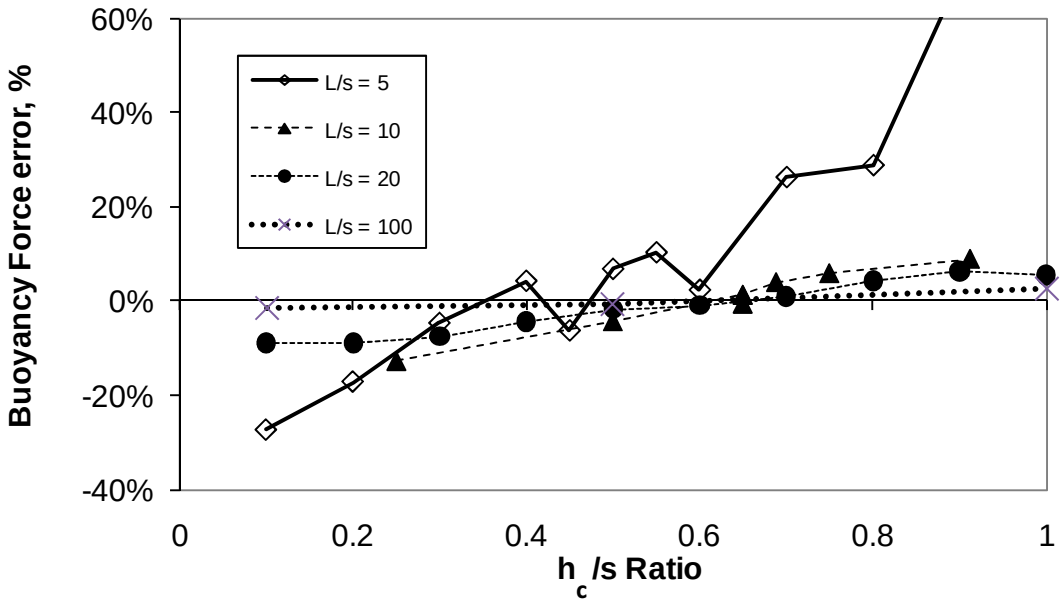

Figure 4-4. Buoyant force error in simulation, for various SPH sizes. (Discrete values of each data set have been joined by lines for clarity.)

This can be illustrated by considering a submerged body of spherical or hexagonal shape, as shown in Figure 4-5. If the body exactly replaces one or more SPH particles, with its boundary exactly half-way between the neighbouring SPH particles, then the neighbouring particles will pack uniformly around the body, in their usual hexagonal arrangement. The value of h_c /s to give the correct buoyant force will be 0.5. If the body is slightly larger, or smaller, then the neighbouring particles are not able to pack uniformly around the body,

producing a reduced local density of the fluid. The value of h_c /s will need to be larger than 0.5 to achieve the correct buoyant force.

A two dimensional study of this packing example was conducted using a 19 cell hexagonal shape, as shown in Figure 4-5. In image a) the submerged shape is exactly of the area and shape that 19 equi-spaced particles would have occupied. The value of h_c /s was 0.5, and the final arrangement of SPH particles around the shape is perfectly regular on a hexagonal pattern.

When the 19 cell hexagonal shape is replaced with a circle of the same area, as shown in image b) of Figure 4-5, the SPH particles cannot pack regularly against the circle, and so arrange themselves as best they can under the forces of gravity. The result is a less dense arrangement of particles. In image c) of Figure 4-5 a square of the same area was also submerged and again the SPH particles were forced to vary from their most-dense hexagonal arrangement to accommodate the submerged shape.

The buoyant force on the circle and square was larger and smaller respectively than for the hex-based shape, indicating that a different value of h_c /s is required to give the correct buoyant force for each shape.

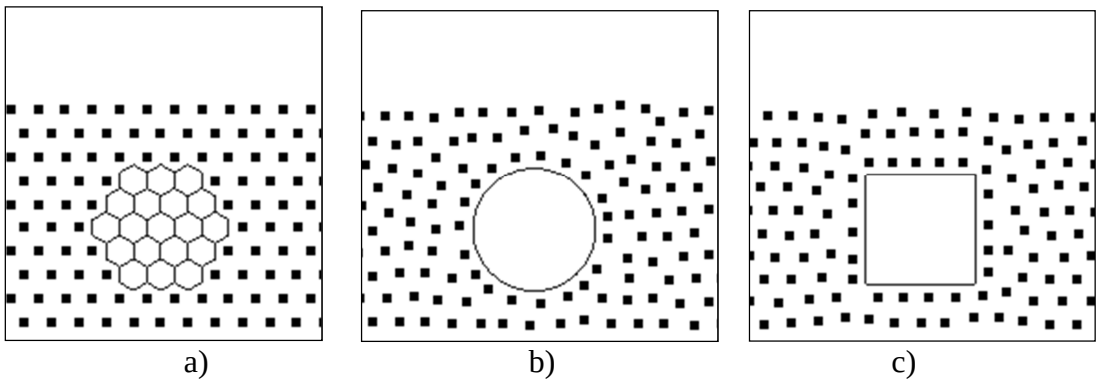

Figure 4-5. Close-up views of packing irregularities around simple shapes.
(Note – image boundaries shown here are not the SPH domain boundaries – these are snapshots within the domain with a focus on the packing around the specific shapes.)

A further observation of the SPH distribution around the shapes of Figure 4-5 is that they are not symmetrical about a vertical axis through the centre of the submerged shape. This creates a net lateral force on the submerged shape. This net force is very much geometry dependent and is significant here only because of the coarse particle sized used to illustrate the nature of the packing problem. In a more research oriented simulation, the SPH particle size would be much smaller and so the corresponding lateral force due to an unequal number of fluid particles on either side of the centre line would be significantly smaller.

The hexagonally-based shape in Figure 4-5 a) suggests that if all submerged shapes were made to conform to some integral number of hexagonal shaped building blocks, then the displaced volume would be correct. This may be possible, but seems impractical. It also relies on the submerged shape to be conveniently located to replace the existing SPH particles in the optimally packed domain.

From these examples it is shown that the contact interface will introduce an error into the buoyancy calculation.

4.3 *Error Limits in the Buoyant Force*

An estimate of the maximum error in the buoyant force as a function of the h_c /s ratio can be derived from the geometry of the submerged shapes and the limits in "reasonable" contact parameters. This estimate can then be used to determine the particle size to ensure a minimum error for a specific shape.

Maintaining perspective of the application of these techniques to a ship in waves, this study in error limits is relevant in that the volume of water for numerous wavelengths will be significanly larger than the volume of water required merely to submerge a body as shown here. There will, by necessity, be a compromise in the number of particles that can economically be solved when a volume of water many wavelengths long is considered, and so understanding the limits on particle size is inherent to obtaining meaningful results.

Figure 4-6 shows the reasonable limits for the contact distance h_c for a submerged square. The maximum reasonable limit is for the SPH particles to be located at a distance away from the box equal to their own equi-distance spacing, giving a value of h_c equal to s. A minimum distance would be a distance of zero, which places the SPH particles exactly on the edge of the box.

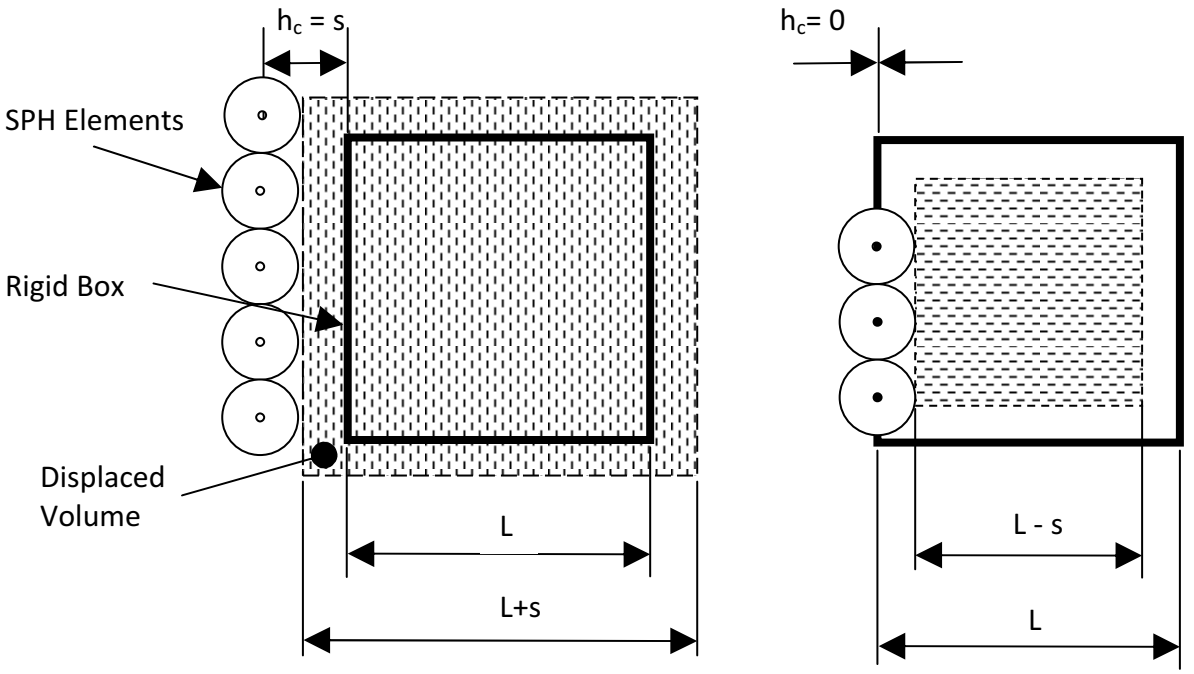

Figure 4-6. Limits of reasonable values of the contact distance.

From these limits, the maximum area is then the area of the box with the sides lengthened by s, represented by the shaded area in the left diagram of Figure 4-6. Similarly the minimum area is a box of sides of length L minus s, as shown in the right image of Figure 4-6.

A comparison of the areas calculated for the two cases shown in Figure 4-6 shows that as s becomes much smaller than L, i.e. s<<L, the error in the displaced box approaches 2s/L. Using this expression, an estimate of the maximum error in buoyancy for a given L/s ratio can be determined, as shown in Table 4-2.

Table 4-2 Maximum Error Estimate for Submerged Squares.

L/s	Error
5	~ 40%
10	~ 20%
20	~ 10%
40	~ 5%
100	~ 2%

These values are in general agreement with the curves of simulation results for submerged squares shown previously in Figure 4-4. The upper right points in Figure 4-4 show an error larger than the estimated 40% error for L/s equals 5. This can be explained by s not being much smaller than L, and also by the errors due to packing of SPH particles against rigid bodies.

In practice it would be advisable to use L/s ratios of 40 or greater to ensure an error of less than 5%.

It can be concluded that the error will approach zero as L/s goes to infinity, if h_c is proportional to s.

These error estimates are the maximum error that would result from using the worst possible value of h_c, which is when h_c is the same as the SPH spacing, s. Intuitively, and from Figure 4-4, the correct h_c value might seem to be closer to a value of s/2. The error with a value of h_c of s/2 would be less than the errors in Table 4-1.

Similar calculations can be made for other 2D and 3D shapes, with the errors as listed in Table 4-3. Table 4-3 indicates that the error is shape dependent.

For common submerged shapes of low aspect ratio, a generic rule of thumb is necessary to provide a starting point for hydrodynamic purposes. For high aspect ratio shapes, like the plate in Table 4-3, it is likely that the generic rule of thumb for low aspect ratio shapes may not be suitable, unless L/s is suitably large.

Table 4-3 Error Estimate for Submerged 2D shapes and 3D volumes.

Dimension	Shape	Error
2D	Square, of side length L	2s/L
2D	Circle, radius R	s/R
3D	Sphere, radius R	1.5*s/R
3D	Cube, side length L	3s/L
3D	Square Plate, L square, t thick	s/t

The study was extended to an L/s ratio of 40 for a box in 2D and the results are shown in Figure 4-7. This simulation was setup a little different to the previous tests as much to check the robustness of the rules and also for convenience. The difference was that the SPH particles were defined in their initial positions on an orthogonal distribution, as is conveniently created in the pre-processor. The particles then re-arranged themselves in the first few seconds of the simulation into the more efficient hexagonal distribution with a corresponding reduction in depth.

The L/s value of 40 required a large number of SPH particles. The computational effort for the large number of SPH particles was reduced by commencing the simulation with the box in the submerged location, and allowing the water to settle around the box.

An h_c /s value of 0.49 was used that allowed the model to be built using SPH particles on an orthogonal basis, and defining the contact thickness to be just less than the initial distance of the particles away from the rigid body.

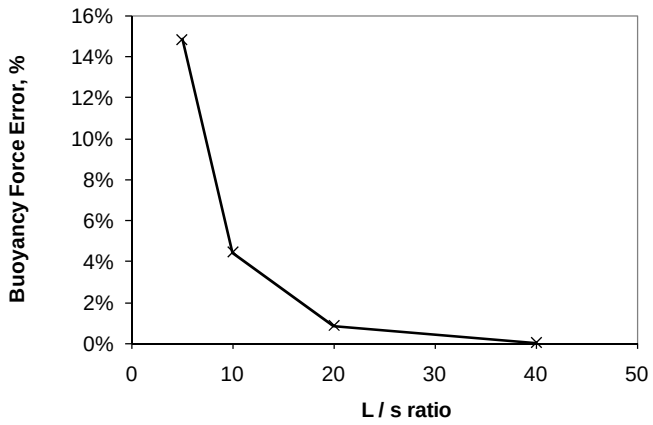

Figure 4-7. Buoyancy Force Error as a function of L/s ratio, for $h_c/s = 0.5$.

Using initially orthogonal spacing implies that the SPH particles will rearrange themselves into a hexagonal arrangement. This rearrangement brings with it an increase of the SPH spacing dimension of about 10%. Hence the actual h_c/s ratio corresponds to about 0.55 of the original orthogonal spacing distance.

The error in the measured buoyancy force was about 1% for a L/s value of 20, and reduced to 0.01% at an L/s value of 40 in this case. This error is less than the Error Estimates of Table 4-2 because the value of h_c /s was closer to the correct value (even though the correct value is not known), instead of the worst case value used for calculating the values in Table 4-2.

4.4 *Spheres and Cubes*

Trial simulations were also conducted in 3D to observe the trend in the measured error. The chosen volumes all had the same overall dimensions. A value of h_c /s of 0.6 was chosen, based on the results for the submerged square. The error in the measured buoyancy force for different SPH particle spacing is shown in Figure 4-8.

The errors in Figure 4-8 are less than the error limits defined earlier in Table 4-3 for the 2D shapes and 3D volumes. This is to be expected as the h_c /s value of 0.6 used here is lower than the maximum value of 1 used to develop the error guidelines of Table 4-3.

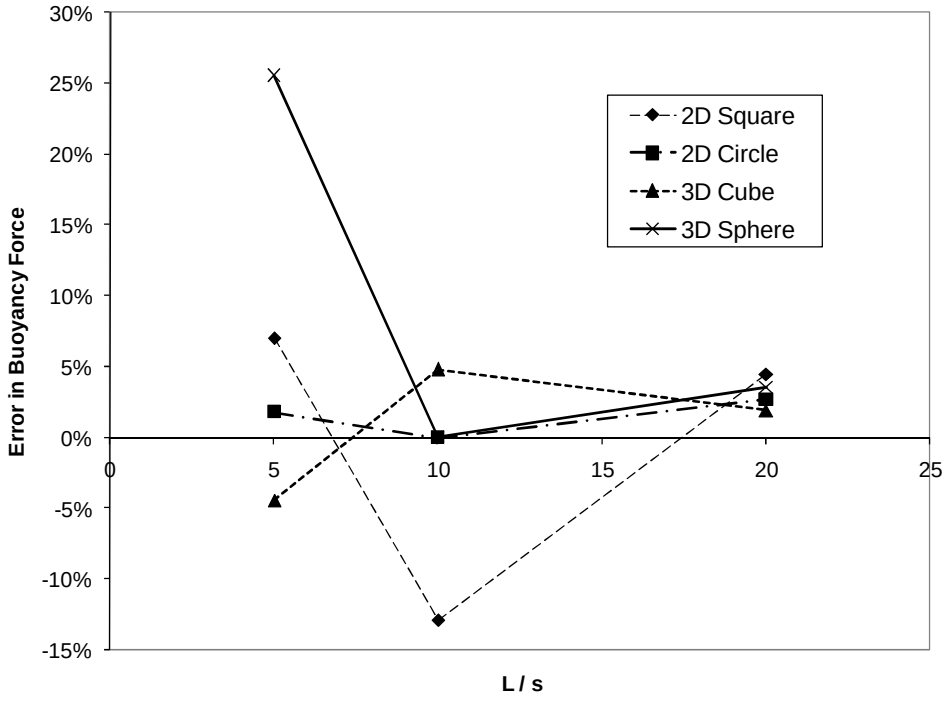

Figure 4-8. Buoyancy Force Error as function of SPH size for h_c /s = 0.6

There is considerable scatter in the results of Figure 4-8, particularly at the lower L/s ratios, and this is most likely due to irregular packing when the particles are only a few times larger than the rigid object, as discussed in Section 4.2.2. Hence the contrary behaviour trend exhibited in the 3D cube error with L/s ratio of Figure 4-8 is possibly a combination of the packing problem when too few particles are used in association with the actual buoyancy reaction force.

Considering Figure 4-4, the errors in the buoyancy force are inversely proportional to the L/s ratio, and are least when an h_c value of 0.6 of the hexagonally distributed SPH spacing is used.

For real world applications, such as ships, it is likely that the displaced volume will tend to be more of a high aspect ratio volume than a low aspect ratio volume, as the waterline length of a ship may be many times its beam. Consequently the critical dimension for determining the error will more likely be the beam of the ship and not the waterline length. It may be possible to develop a more universal description of the buoyancy error for ships based on wetted surface area or girth rather than length, but this has not been investigated here.

4.5 *Orthogonal and Hexagonal Spaced SPH Particles*

Hexagonally spaced SPH particles achieve the highest density when the particles represent a fluid under gravity.

Setting up a simulation with hexagonally spaced particles has been done manually to date, as many pre-processors, including the one used here, do not automatically generate hexagonally arranged nodes to assign the SPH particles to.

The cases presented thus far that have used initially hexagonal spaced nodes were developed by a manual process that used a spreadsheet to calculate the location of the nodes. The nodal coordinates were exported to a text file that was then imported into the pre-processor to have SPH particles assigned.

For a large number of nodes, say greater than 64,000, this becomes quite tedious, as a single worksheet in a spreadsheet such as Microsoft Excel can only handle 64,000 lines of data. It is desirable to have a purpose-built tool to generate this distribution of nodes for simulations requiring large numbers of SPH particles, however that is beyond the scope of this research.

An alternate approach is to use a conventional orthogonal distribution of nodes, as might be produced by many mesh generators or other FEA pre-processors.

When SPH particles on an orthogonal distribution are used, the centre-centre spacing varies between the adjacent nodes, depending on whether the adjacent nodes are on the major axis of the distribution, or on the diagonal. Consequently not all the neighbours of a single SPH particle are equi-spaced. This is shown in Figure 4-9a, where 4 of the 8 neighbours of any central particle will be a distance of 's' away, and the other 4 neighbours on the diagonals will have a distance of $\sqrt{2}$ times the orthogonal distance of 's'.

If the SPH properties allow a sufficiently low viscosity behaviour, then the SPH particles will rearrange themselves as the simulation begins, although sometimes a slight "numerical nudge" is required to overcome the mathematically perfect nature of the initial balance of the forces. In the simulations here, the reaction of the particles due to contact forces at the walls, and the insertion of the box into the water surface, provided sufficient stimulus for the rearrangement of the particles from their initial perfectly orthogonal distribution to the more stable hexagonal arrangement.

The theoretical change in spacing from an initially orthogonal distribution of particles to their stable hexagonal arrangement can be calculated based on constant area for 2D particles. In Figure 4-9a each SPH particle on the orthogonal distribution has an area of s^2. When these elements have rearranged themselves into the hexagonal arrangement of Figure 4-9b, based on consistency of element area, the new nearest neighbour spacing, s', can be shown to be 1.075s, with the next nearest neighbour being $\sqrt{3}$ multiplied by s', or approximately 1.86s.

To confirm this behaviour an initially orthogonal distribution of 1000 SPH particles was allowed to settle over time, and when settled, the neighbour distances of 100 centrally located SPH particles were measured. The 100 SPH particles were chosen from a region of the domain that showed a uniform particle arrangement, i.e. an arrangement that was not influenced by the irregular packing of particles necessary to accommodate the straight boundaries of the domain.

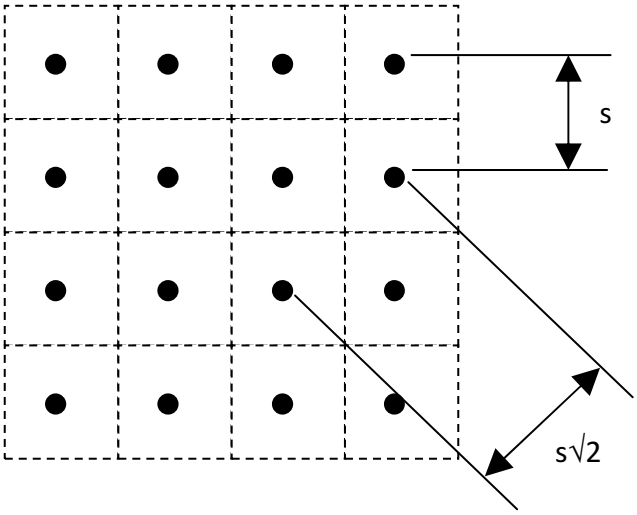

Figure 4-9a. Particle Spacing for Orthogonal Packing.

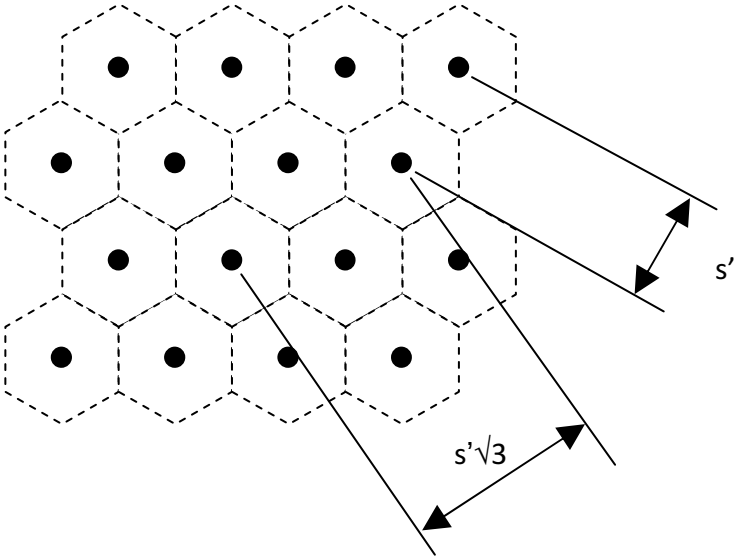

Figure 4-9b. Particle Spacing Hexagonal Packing.

Figure 4-10 and Figure 4-11 show the initial and settled states of the SPH particles. The 100 SPH particles that were studied have been omitted from the view of the Figure 4-10 to highlight their location in the central region of the domain. Figure 4-11 shows a detailed view of these central SPH particles at the same initial and settled states.

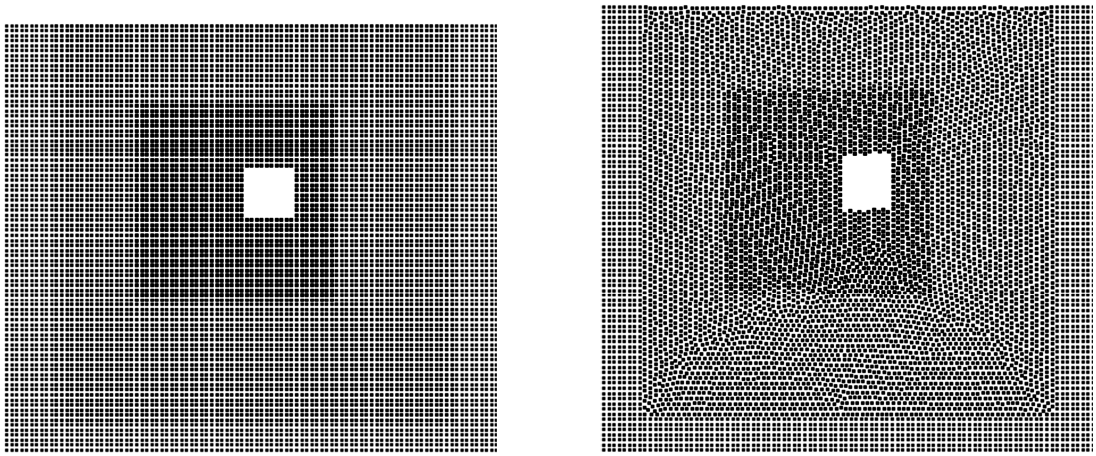

Figure 4-10. Initial and Orthogonal and settled hexagonal SPH particles. The hole in the middles is the location of the particles that were removed to study their neighbour distances. (Outer rows of particles were held fixed for containment)

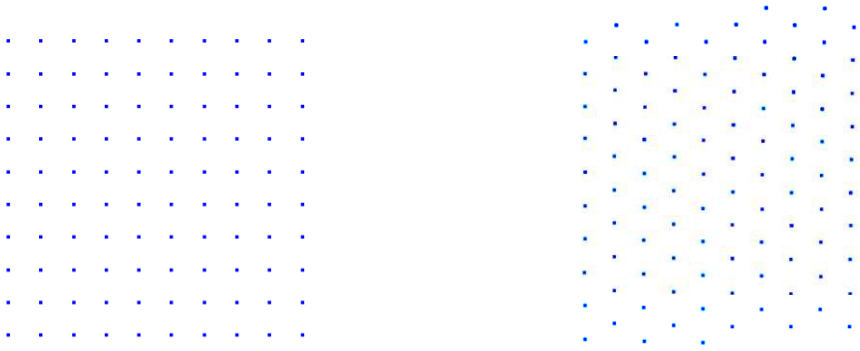

Figure 4-11. Close-up of the 100 SPH particles that were studied for neighbour distance.

The nodal coordinates of each SPH particle were exported to a text file and the distance to neighbours calculated using a spreadsheet. The neighbour distances were normalised by the initial spacing, s, and the frequency of neighbour distances was accumulated into distance ranges to produce Figure 4-12.

In Figure 4-12 the most common neighbour distances for the initial orthogonal condition are the initial spacing of 1.0, the diagonal spacing of $\sqrt{2}$ (approximately 1.4) and then twice the initial spacing of 2.0. A normalised distance of 2.0 is not the nearest neighbour but the next neighbour in the same direction. (Note there is a slight tolerance on the exact distances measured due to the distance range of each interval.)

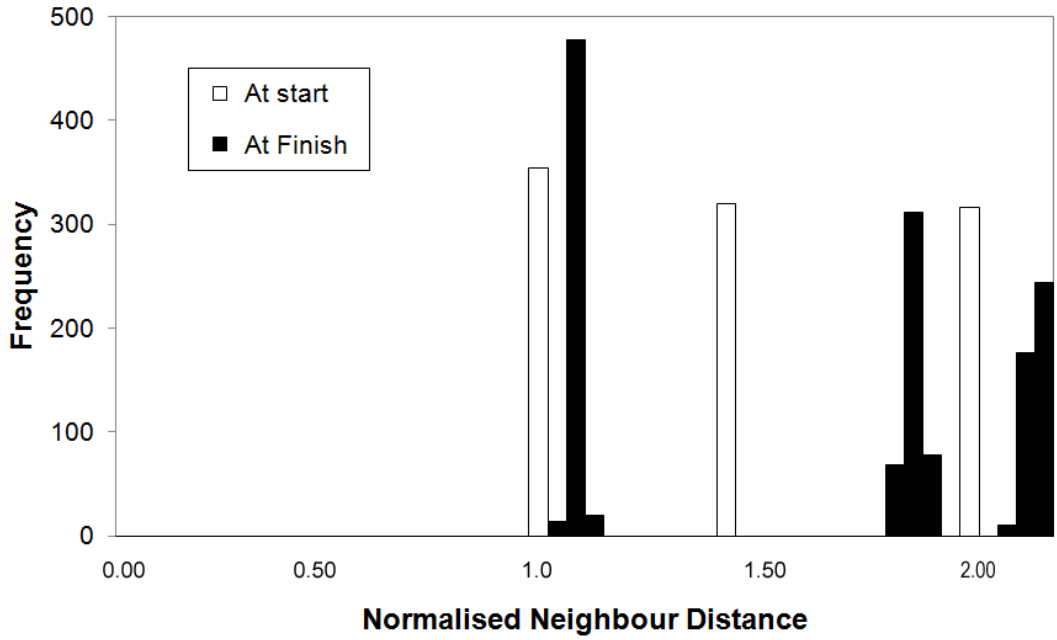

Figure 4-12. Frequency of normalised neighbour distances for orthogonal and hexagonal distributions.

For the settled particles the most common normalised distances are at about 1.09 and about 1.9. (The presence of some distances in the adjacent lower distance bin implies the mean of the settled distances would be slightly lower than the quoted values of 1.09 and 1.9.)

These settled normalised neighbour distances compare favourably with the theoretical values shown in the Figure 4-9b of 1.075s and 1.86s presented earlier.

Following the earlier results, the recommended contact thickness distance, h, is 0.6 times the hexagonal spacing, or 0.55 of the orthogonal spacing.

4.6 *Buoyancy Force as a Function of Time*

As the nature of the SPH simulations are a time-dependent response, a brief comment on the long-duration time-dependency of the solution is worthwhile.

The buoyancy force simulations presented earlier in this chapter were conducted over 20 seconds. At the end of this time the force 'appeared' steady and the results estimated. On closer inspection, it was noted that the buoyancy force was not always constant, but still rising (losing magnitude) very slowly. To study this further, a longer simulation was performed, even though ship motion studies is not inherently interested in quasi-static behaviour of such long duration.

A simulation using 0.4m particles on a 2m x 2m box was extended to 800 seconds, maintaining the same time step, and the result is shown in Figures 4-13 and 4-14. The

interest here is the change of buoyancy force with time, not the absolutely buoyant force. Note there is significant noise in the early stages of the simulation due to the box deceleration at depth not being smooth as shown in Figure 4-2, but was decelerated abruptly resulting in large force oscillations. Similarly, Figure 4-2 shows the unfiltered net force on the box which is inherently noisy.

On the large time scale, the force looks steady with time. Expanding the vertical scale it is observed that the buoyancy force is not steady with time, but is drifting upward (losing magnitude) in an approximately linear fashion with time.

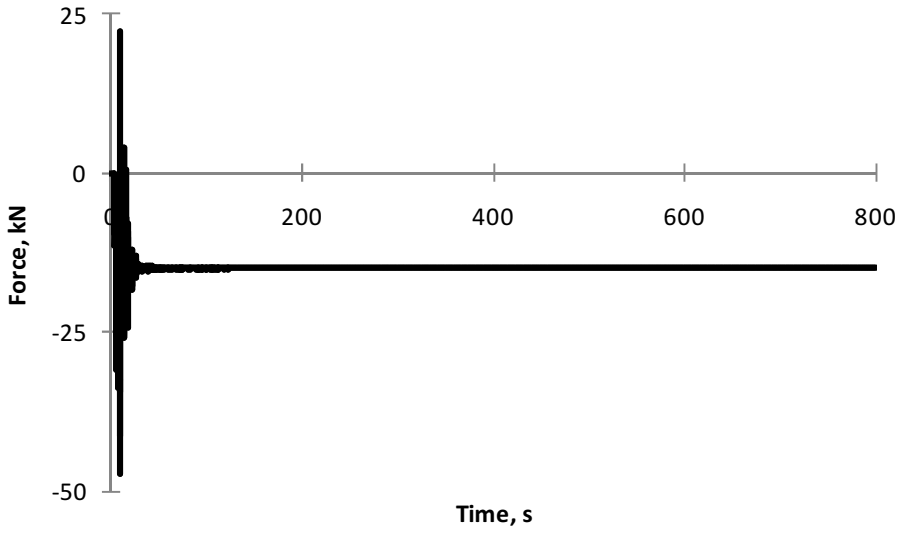

Figure 4-13. Buoyancy force from simulation for a 2D submerged box test over 800 seconds.

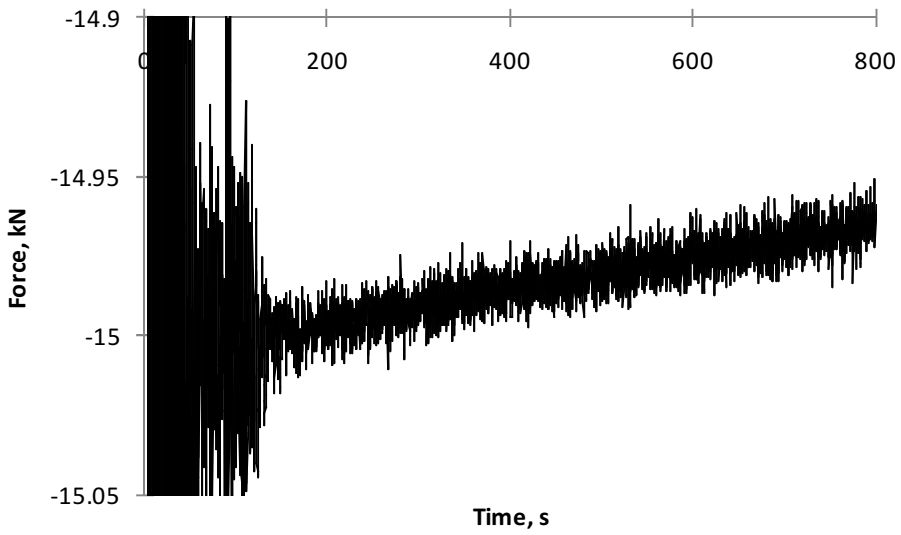

Figure 4-14. Expanded vertical axis of the 800 second 2D submerged box test.

The change in buoyancy force is about 30N over 800 seconds, on an initial magnitude of about 15,000 N. This change is about 0.2% of the buoyant force over 13 minutes, so the effect is evident and measurable, but is likely to be less than the error in the total buoyant force, so is not considered significant to ship motion studies.

The linear nature of this drift suggests that the result is steadily drifting upwards and not approaching an equilibrium value within the time and magnitude shown here. Extrapolating this drift linearly indicates that the buoyancy force would approach zero after about 4.6 days of submersion time. It is seemingly absurd to compute the buoyancy force over 4.6 days, so does not represent a practical analysis that would be performed by the SPH technique, but it is an effect that needs to be understood more comprehensively.

From these results it is not clear why there is a reduction in the force with time. Two likely sources are the SPH algorithms and the contact force algorithms. The SPH algorithm may be at fault due to the approximations inherent in the "smoothing" nature that makes the algorithm so attractive in its simplicity. Conversely the contact force algorithm may be a suspect as these rely on implementations of numerical springs that require some deflection to develop an opposing force. The numerical controls to maintain stability of these springs is a potential source of energy loss, which may manifest itself as a loss of force, as would any deliberate damping applied to these contact algorithms.

It is likely that all simulations performed using this software (and those similar to it) will exhibit some drift as shown here. As the SPH technique is more suited to dynamic events, it would be sensible to be aware of this effect and to consider if the dynamic forces are comparable in magnitude to the drift exhibited here. If, however, the dynamic forces are orders of magnitude larger than the drift, then this drift effect can most likely be safely ignored.

4.7 *Location of the Free Surface*

The aim of this research is to use mesh-free methods to investigate the response of a ship on the water surface in both a static and dynamic situation. To do this requires that the location of the free surface on the side of the ship is known.

4.7.1 Location of the Free Surface

In the graphical post-processing of the SPH results, the particles are represented by a node at the centre of the volume of the SPH particle, as shown in 2D in Figure 4-15. These nodes are the location in space on which all the numerical calculations of the SPH particle are based. The free surface is not at these nodes, but at some distance above these points. For the 2D hexagonal arrangement shown in Figure 4-15, the free surface will be where the area of fluid within the hexagonal particles above the surface equals that of the 'void' between the particles below the free surface line. This can be shown to be at a location of $\sqrt{3}/4$ times the SPH spacing above the nodes.

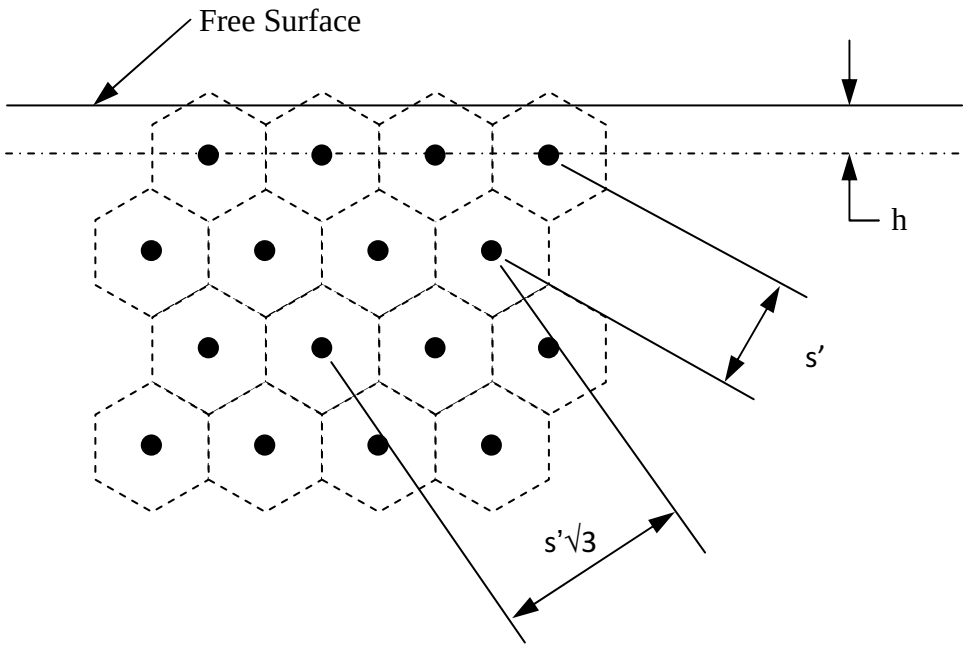

Figure 4-15. Location of the Free Surface for Hexagonally packed SPH particles in 2D.

The concept is similar to the distance used for the contact thickness for the submerged body, except for the submerged body is a rigid surface that is easy to visualise. In the case of the free surface there is no plane or surface to help visualise this location. (This may be a useful feature to include in future versions of the post-processor for SPH and fluids.)

Previously the value of h_c for submerged objects was found to be between 0.55 and 0.6 of the SPH spacing. The value geometrically shown here of $\sqrt{3}/4$, or ~0.433, is smaller, presumably due to the perfect packing of the particles shown here. In the practical cases of submerged objects, the packing is not perfect, and being larger on average than the perfect hexagonal packing, which results in a local reduction to the fluid density, hence requiring larger contact thickness than theory suggests.

If the packing of the SPH particles on the surface is not perfect, then the location of the free surface will be higher than the theoretical value shown here. As the location of the free surface is proportional to the spacing, reducing the SPH spacing will also reduce the error in the location the free surface.

4.7.2 Floating Objects

The location of the free surface for a floating object is now able to be identified.

To demonstrate this, a simulation of a rigid box floating in water was conducted. The tank was fixed in space and the box of known mass was restricted to vertical movement only. The box and the water experience acceleration due to gravity. The model is shown in Figure 4-16. The focus was the location of the free surface and the draught of a floating object. Tank size is irrelevant so long as the tank does not overflow.

The SPH spacing was 0.4m, and the effective 2D simulation had a thickness of 0.4m also. The box was 2m wide and 7.6m tall, being of a size relevant to model tests but also relevant to small vessels. The mass of the box was 1937 kg. The tank was 12m wide and about 5.3m deep and the density of the water was 1000kg/m^3. (A 'marker' node for accurate determining the box location was attached to the bottom of the box, visible as a single small square marker in the illustrations.)

To ensure that no SPH particles were in the box at the start of the simulation, the box was initially above the water surface, and fell into the water when gravity acted on it. As this was a dynamic test case, the result was time-dependent, and showed evolution of splash, waves and dissipation of the motions. Four moments of the process are shown graphically in Figure 4-17.

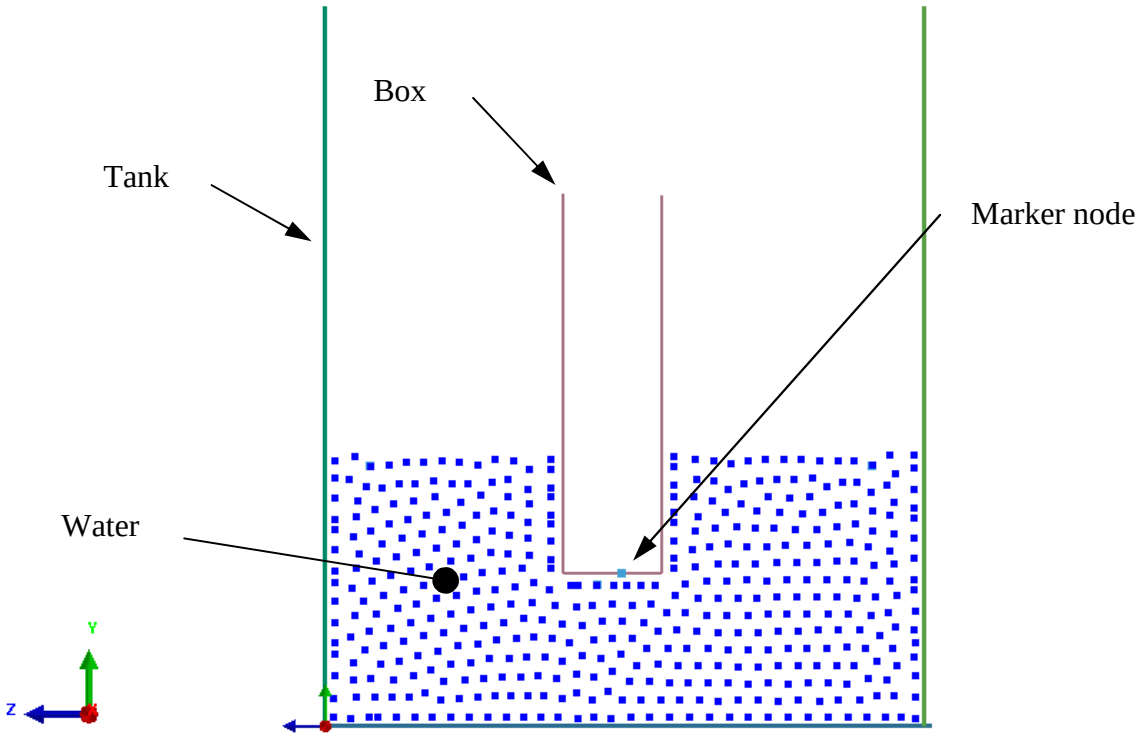

Figure 4-16. A 2D model of a rigid body floating in a fluid of SPH.

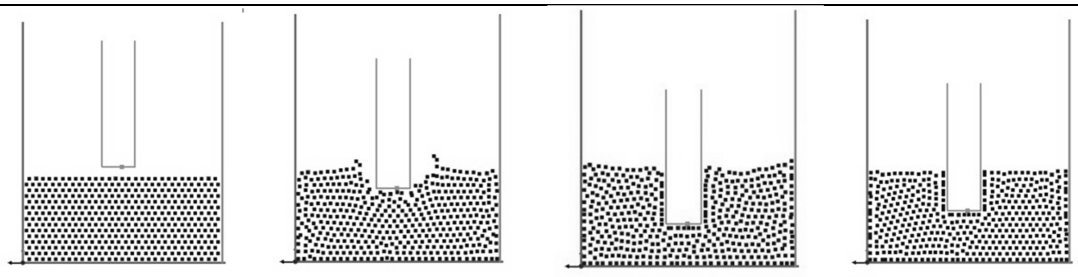

Figure 4-17. Four stages of a box coming to floating equilibrium.

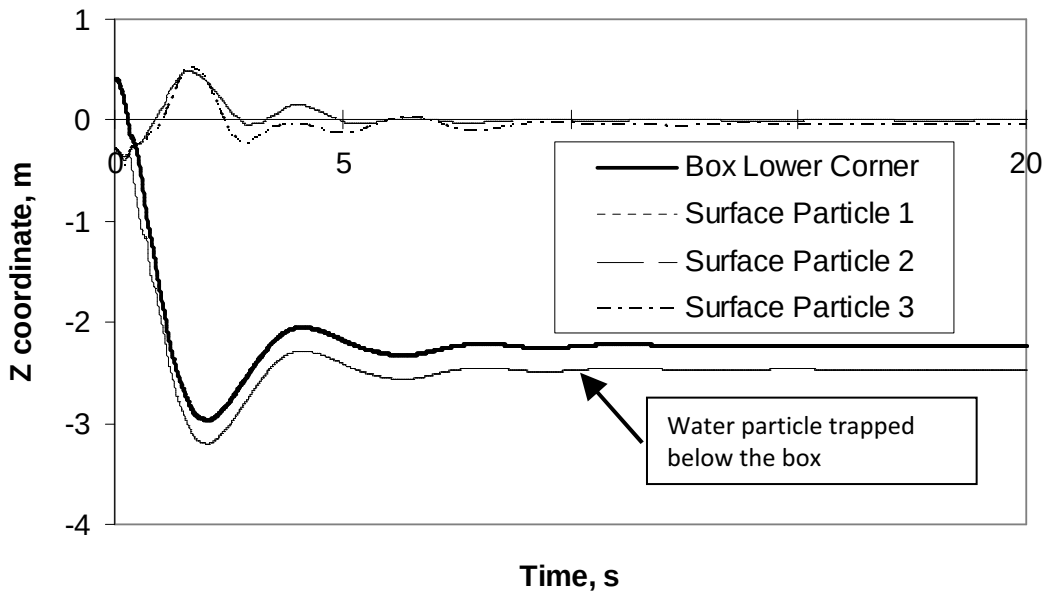

Figure 4-18. Vertical Coordinates of the box lower corner and SPH particles.

Figure 4-18 shows a plot of the vertical coordinates of four points in the simulation with time. The four points are three SPH particles that were initially on the surface, and the marker node on the lower surface of the box. These values enable the sinkage of the box to be calculated. The datum was calculated after the simulation and is the average of all the surface particle coordinates when then the box and water have settled.

Initially the three SPH particles were at the same height on the water surface, and the box was above the water surface. Note the initial vertical position of the surface particles is below the final equilibrium position. From time t = 0, the box began to drop in height, and the SPH particles settle slightly into the tank under gravity, visible as a slight drop in water level at the start of the simulation. At about t = 0.5 seconds, the lower edge of the box came into contact with the water surface, and the mean water level in the tank began to rise, as shown by Surface Particle 1 and Surface Particle 3 rising in elevation. Surface Particle 2 continued downward as it was trapped directly underneath the box, as shown in Figure 4-16.

The water and the box then oscillated for a few cycles before being damped out to a steady state. The slow and steady drift in the equilibrium position identified in Section 4.6 would have occurred after this time, at a slow rate, and so the conditions at 20 seconds were considered as an equilibrium condition for the current purpose.

The rules established earlier defined the free surface to be at approximately 0.4 times the SPH spacing above the surface particles. For this case the free surface as at z coordinate of 0.16m. The depth of the Box Lower Corner was -2.234m, a distance of 2.394m below the actual free surface.

The theoretical draught of the box was 2.421m from the box dimensions and the water density given earlier.

The error in the simulated draught is 0.027m, being an error of 1.1% on the theoretical draught, with an equivalent error in total displacement. Ideally this error would be less, but considering the coarse nature of the SPH spacing, this is acceptable.

These calculations allow the waterline to be located numerically. This is useful for confirming initial static conditions before the response of the ship to a dynamic event is simulated – such as encountering waves, or flooding due to damage.

4.8 *Visualising the Free Surface*

Accurately visualising the water surface is currently not possible in the software used here, as the graphical 'marker' is drawn at the location of the centre of the SPH particle volume, not its surface. As the number of particles increase and the individual particle volume reduces to the point where both are merely a visible 'point' on the image, the visual marker will more closely indicate the actual location of the surface.

For the study of hydrostatics on specific shapes a large number of SPH particles could indeed be used such that the visualisation of the free surface is accurately represented by displaying the centre of the volume. However, it is the study of the dynamic motion of a ship that is driving the size of the SPH particles chosen for this early stage of the research. The SPH particle size must be adequate to fill a tank that is many wavelengths long, and of sufficient depth and width so as to allow a reasonable passage of a ship, yet still be solved economically by today's computing resources. Thus the size of the SPH particle may look coarse for these studies, but the findings here will be directly relevant to a practical engineering solution for the motion of a ship in a larger tank.

For applications where it is not feasible to have sufficiently small and numerous SPH particles, an approximation to the location of the water surface may be obtained by adjusting the 'marker' size of the SPH particles such that they just touch or overlap each other, as shown in Figure 4-19. This is a trial and error process, and is dependent upon the visual extents. This is due to the SPH particles being represented by a 'marker' point at their centre of volume for each particle. It is possible to visualise only the top layer of SPH particles at any one time, and then animate these particles over time. If an SPH particle moves below the surface, it is not automatically removed from the visualisation and will remain visible, as shown in Figure 4-20 (Groenenboom et al, 2009).

Kalis (2007) developed a post-processing routine for the software to map the water surface and this made for visually appealing animations. The cinema industry have recently used various meshfree/particle methods, such as SPH, to model fluid flows with great visual effect (RealFlow 2010, AutoDesk MAYA 2011). The graphic processing of these fluid flows suggest the underlying algorithms to calculate and illustrate the location of the free surface are available, but they may not be as scientifically accurate to be useful for engineering purposes. The emphasis of the software used here is physical accuracy in numerical solutions, and so the graphics of the post-processor are not industry-leading for visualisation niceties.

In contrast to the traditional finite elements, it should be noted that the SPH particles are able to move on a scale much smaller than their spacing, and so the size of the SPH particles does

not provide an indication of the resolution to which the free surface can be located. i.e. the free surface is located at about 0.4 diameters above the centre of the SPH particle, but the SPH particle itself can move in increments much smaller than its diameter. This is similar to the Volume of Fluids (VOF) technique being able to define a proportion of fluid and air within a single element, and so the resolution of the location of the free-surface in VOF techniques is smaller than the finite element dimension.

An option in development for PAM-CRASH is the ability to determine the distance above an arbitrary point in the fluid where the density is half the fluid density (Groenenboom and Cartwright, 2009). By using the SPH functions as elsewhere for the fluid, the density based on the smoothing length and kernel is calculated in an upward direction from the reference point, and the free surface is defined as where this local density is one-half the fluid density. This technique is not yet able to handle multiple surfaces, and so will find the first free surface above the reference point. Further, this development provides a numerical location of the free surface only, and not a graphical representation, but gives insight for another method that could be developed to visualise the free surface.

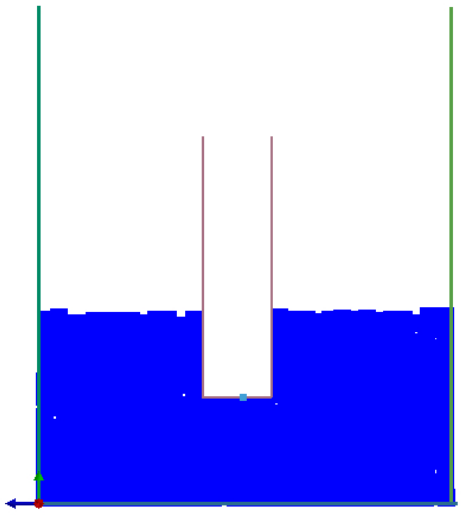

Figure 4-19. Visual representation of free surface by approximation.

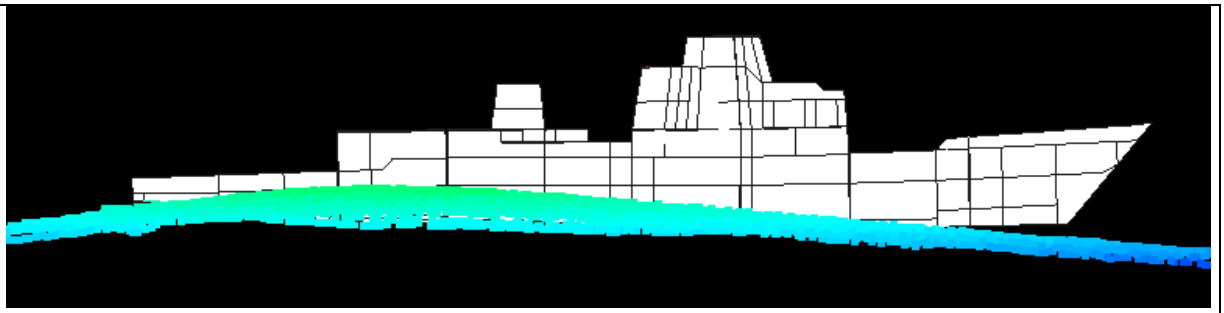

Figure 4-20. Representation of the free surface by the surface SPH only. (Groenenboom and Cartwright 2009)

4.9 *Theoretical Location of the Free Surface*

The location of the free surface relative to the centre of the SPH particles can be determined if the particles are assumed to be optimally spaced. This provides a further check on the sensibility of the 'guidelines' developed earlier.

4.9.1 Two dimensions

For closely packed SPH particles in two dimensions the exact location of the free surface can be found from a geometric study.

Figure 4-21 shows three SPH particles on the surface. The free surface will be at a distance of h_c from the centre of the particle circle when the areas A1 and A2 are equal. At this condition there is an equal "area" of the fluid (in two dimensions) above the free surface but within the particle as there is a void beneath the free surface between adjacent particles.

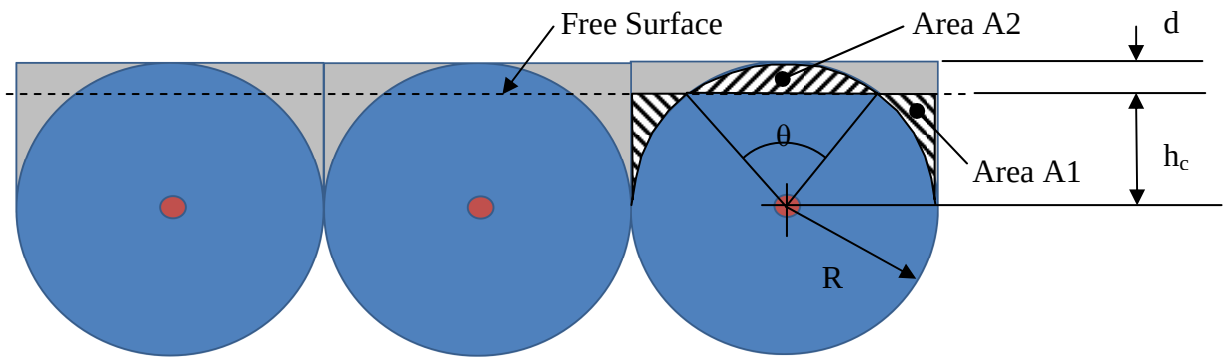

Figure 4-21. Location of the free surface in two dimensions.

For this geometry, R is the radius, θ the angle of the segment, d the depth of the segment. The area of the arc segment A2 is given by:

$$A2 = \frac{R^2}{2}(\theta - sin\,\theta) \tag{29}$$

And the angle, θ, is :

$$\theta = 2\arccos(\frac{h_c}{R}) \tag{30}$$

The area A1 is the area of the rectangle ($2Rh_c$) less the area of the semicircle without the segment:

$$A1 = 2Rh_c - (\frac{1}{2}\pi R^2 - A2) \tag{31}$$

Figure 4-22 shows the curve of areas A1 and A2 as a function of the distance h. The crossover point is at 0.785. This implies that the contact thickness should be 0.785*R*.

The packing density of circles in a plane is only 90.69%, i.e. the voids account for almost 10% of the area. The volume associated numerically to the SPH particles is independent of the spacing and so the volume of each SPH particle should be larger than if they just touch, to account for the volume of the voids.

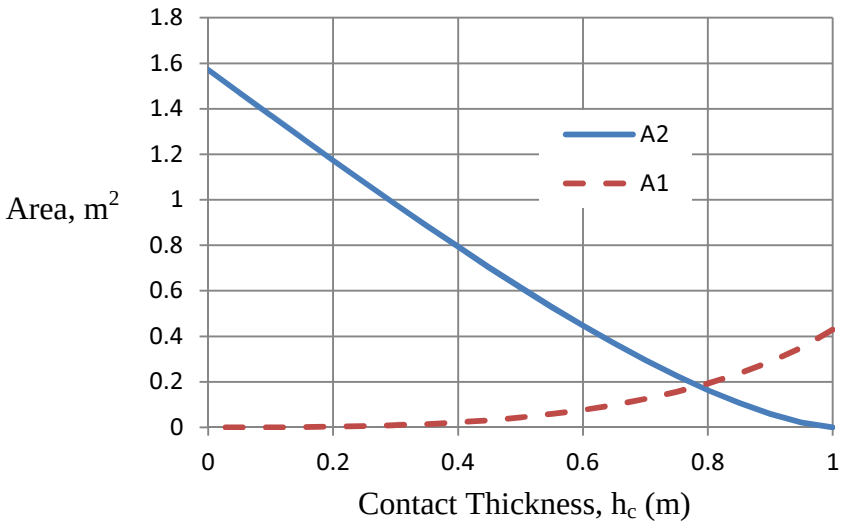

Figure 4-22. Areas of 2D SPH particle above the free surface (A1) and area of void below the free surface (A2) for contact thickness h, assuming an SPH volume based on the centre-centre distances.

Following the above process to find the waterline, but now considering that the area of each SPH particle is 1/0.9069 larger, the cross over point changes to 0.825 of the radius, as shown in Figure 4-23.

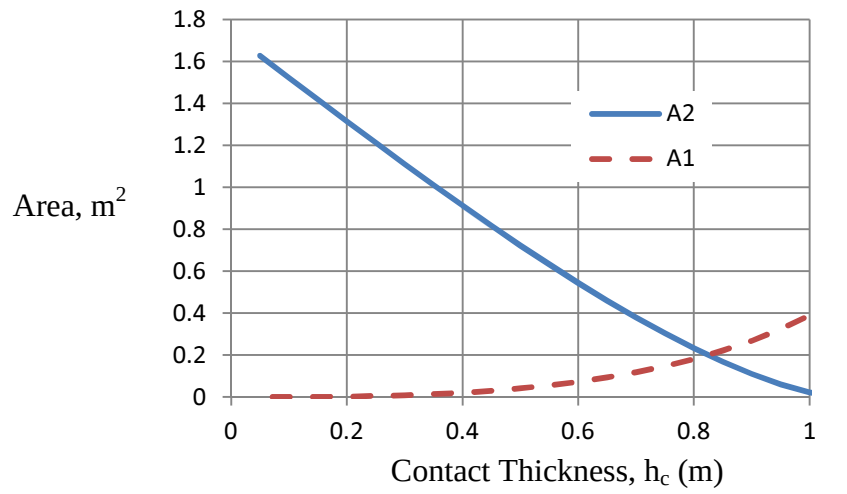

Figure 4-23. Location of the free surface in 2D accounting for the voids between the particles. The surface is located distance h from the particle centres where the two curves cross over.

Expressed as a ratio of the SPH spacing, the theoretical value of h_c/s for the location of the waterline is 0.825 / (2R) = 0.4125.

This theoretical value does not agree with the observed experimental value of approximately 0.6 presented in Figure 4-4. The reason for this is likely to be the assumption of perfect packing for the theoretical solution, whereas in practice, the packing of the SPH particles is not likely to be uniform and optimal, particularly adjacent to the submerged object, as explained earlier. The packing cannot be greater than the theoretical maximum density, and so any other distribution of SPH particles will result in a lower local density, implying a larger contact distance will be required.

Extending this to the free surface, a similar effect can be expected. Consequently it will be difficult to identify exactly where the free surface is, but it should be possible to define a range where it will lie, based on the spacing of the particles.

4.9.2 Three dimensions

A similar study can be made in three dimensions. The definition of the volumes is shown in Figure 4-24.

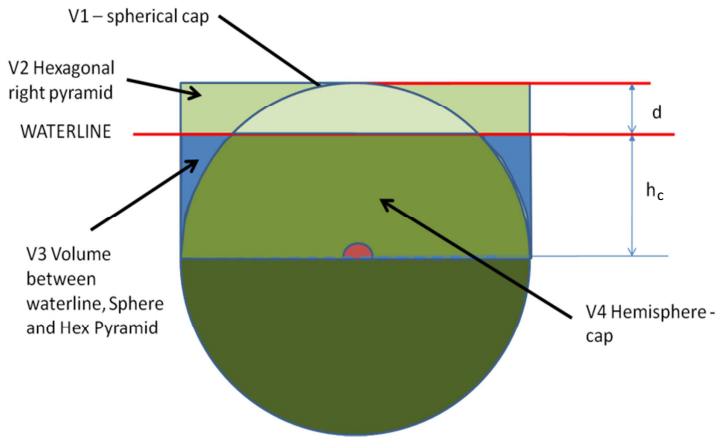

Figure 4-24. Dimensions and volumes for location of the free surface in three dimensions.

Following the concepts for 2D, Figure 4-25 shows a curve of the volume of the spherical cap and the volume of the void below the line that is h_c away from the centre. The cross over point indicates where the free surface should lie, in this case at a distance of 0.605*R* from the centre of the SPH particles.

3D packed spherical particles have a volume ratio of 74.05%, so the actual volume of the particles must be greater than the spacing would allow for touching spheres with a diameter equal to the spacing. The actual volume of each particle should be increased by (1/0.7405) to ensure that the voids are filled. Using a particle radius based on this larger volume, the curve of Figure 4-26 indicates that the free surface will be located at 0.817R from the particle centres.

Expressed as a ratio of the particle spacing, the theoretical values of h_c/s is 0.408 in 3D.

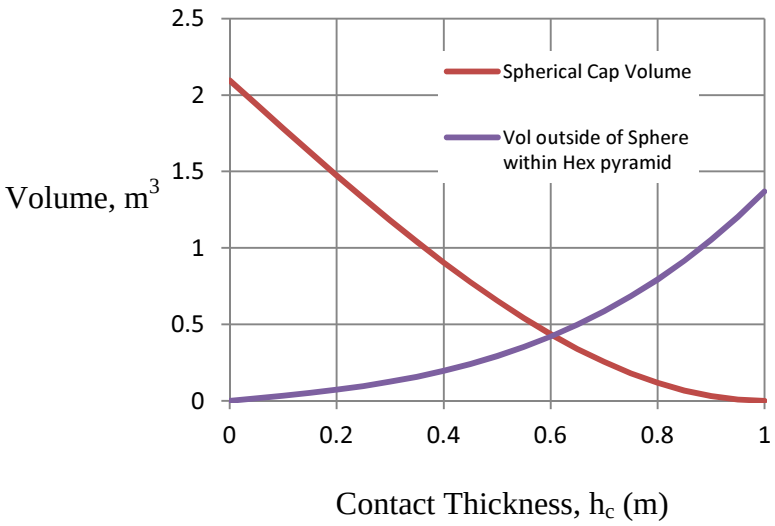

Figure 4-25. The free surface in 3D is located at a distance away from the cente of the SPH particle equal to the cross over point of the two curves, when considering a volume based on the particle spacing.

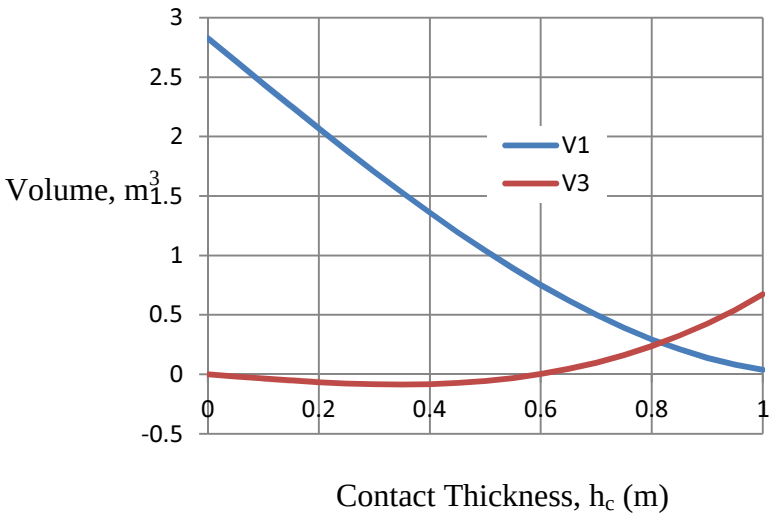

Figure 4-26. The free surface in 3D is located at a distance away from the centre of the SPH particle equal to the cross over point of the two curves, when considering particle volumes accounting for voids in the packing.

4.10 *Recommendations for the Location of the Free Surface*

Relying on the numerical results more so than the theoretical, as the theoretical results only consider perfect packing and not the irregular packing of particles that will inevitably occur, the free surface is located close to 0.4 times the SPH centre-centre distance above the centre of the upper-most particles. This rule is based on the centre-centre distance of hexagonally packed SPH particles.

If the particles are initially orthogonally packed, the resulting rearrangement of particles into a uniform hexagonally packed arrangement will increase this distance to approximately 0.45 times the orthogonal centre-centre distance.

4.11 *Recommendations for Correct Buoyancy*

Using the rules developed earlier in this chapter;

A) for an error of less than 5% in the buoyancy force when settled, the SPH particle spacing needs to be $1/20^{th}$ or less of the principal dimension of the floating object.
B) The contact thickness distance, h_c, should be 0.6 times the hexagonal spacing distance, or 0.55 of the orthogonal spacing distance.

4.12 *Hydrostatics of AMECRC09*

The focus of this work is the response of Model #09 from the AMECRC High Speed Displacement Hull Form Systematic Series. This hull is one of a series of ship hulls developed by the Australian Maritime Engineering Cooperative Research Centre in the 1990s.

The hull series is described in detail in (Macfarlane and Lees 1999). For the work here a Finite Element (FE) model of the hull was required, and this was built from an A3 drawing of the lines. The hull model in the FE software was effectively a surface mesh of shell elements that constituted a rigid body. The rigid body definition ensures no deformations of the hull occur. The FE model was then assigned mass and inertia properties representative of the actual model hull.

The particulars of the original Model #09 and the FE model are summarised in Table 4-4. The model hull had a Waterline Length (LWL) of 1.6m.

Table 4-4 Particulars of the Model #09 and the FE Model.

Model	L/B	B/T	Cb	LCB %*	LCF %*	LWL (m)	Wetted Surface Area (m2)	Displacement (kg)
#09	8.00	2.5	0.5	-5.40	-8.75	1.6	0.3732	12.804
FE	8.00	2.5	0.5	-5.70	-8.80	1.6	0.3766	12.804

* *LCB and LCF are positive forward of amidships*

Lines for the hull are shown in Figure 4-27.

To calculate the hydrostatics using the SPH code here, the hull was placed in a tank and allowed to find its own equilibrium position. The tank size was chosen to be computationally efficient yet sufficient size to adequately determine the location of the waterline. The nominal size of the tank was 1.5 times the length, two time the beam and two times the draught of the hull. The hull commenced the simulation above the SPH particles, and was allowed to fall under gravity into the SPH particles to find an equilibrium. The hull was allowed to settle over 20 seconds, a time sufficiently long to allow natural frequencies of heave (2.26 Hz) and seiche (0.25 Hz) to dissipate, leaving the hydrostatic response of interest.

Simulations using SPH at two different orthogonal spacings were trialled: a particle spacing of 0.04m corresponding to an LWL to SPH spacing (L/s) ratio of 40, and a particle spacing of 0.016m to give an L/s ratio of 100. (As a comparison, if the breadth of the vessel is considered to be the critical dimension, these ratios correspond to B/s of 5 and 12.5.)

As the original arrangement of SPH particles was orthogonal, an h_c/s ratio of 0.55 was used for the ship to fluid contact thickness (refer Section 4.9), and the free surface was estimated to be located 0.45 times the SPH spacing above the centre of the SPH particles when settled.

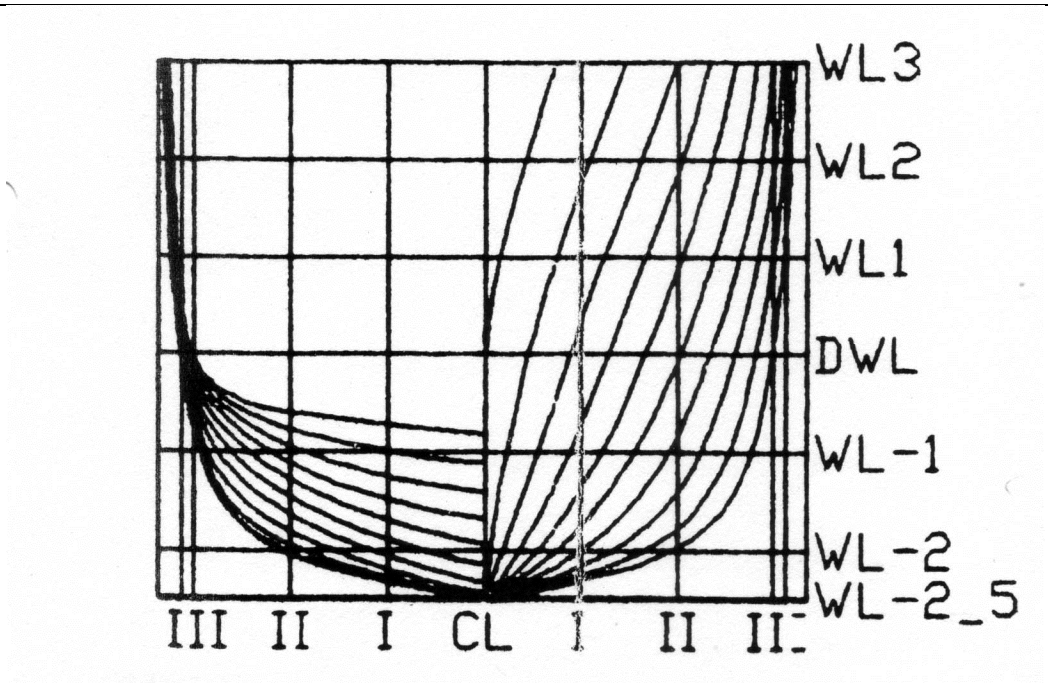

Figure 4-27. Lines of the Model #09 of the AMECRC HSDHF Series. (Macfarlane and Lees 1999)

The average free surface location was estimated by taking the average z coordinate of all the SPH particles on the surface of the fluid at the end of the simulation, and then adding the constant factor of 0.45 times the initial SPH spacing distance.

Table 4-5 lists the location of the free surface at equilibrium, the Design Water Line (DWL) and the error in the DWL from SPH for the two L/s ratios. The DWL was taken as being a horizontal plane through the Centre of Flotation (LCF) at design conditions. The reference DWL was that from the lines of the vessel shown in Figure 4-27.

In Table 4-5 the coordinate values are negative as the reference point was above the free surface. Further the free surface was in a different position for the two L/s ratios because the dimensions of the tank were different, being narrower and shallower for L/s = 100 to allow fewer SPH particles to be used (but still more than in the for L/s =40), to facilitate a quicker solution.

Table 4-5. Displacement Error for AMECRC09 in SPH.

L/s	Time (s)	Coordinate of Free Surface (m)	Coordinate Waterline of Model	Error in DWL from SPH		Equiv error in Displacement
				m	% LWL	
40	20	-0.4234	-0.4261	-0.0027	0.17%	5.4%
100	20	-0.4567	-0.4606	-0.0035	0.22%	7.0%

The design draught of the model was 80mm. The equivalent error in displacement is the percent of design displacement that would provide the same change in draught, calculated from the mass per unit immersion at design conditions. It should be noted that in simulation here, there was no change in the mass or inertia of the vessel.

The error was larger for the smaller L/s ratio, which was not expected. The reason for this is explained in the interpretation of Figures 4-28 and 4-29.

Figure 4-28 shows the change in DWL location with h_c/s ratio for the L/s ratios considered. There was a lower rate of change of DWL for the higher ratio, as expected.

Figure 4-29 shows the trim of the vessel as a function of h_c/s ratio for the L/s ratios used. There was a lower rate of change of the trim angle for the higher L/s ratio. Note that the trim angles are small, at +0.03 degree and -0.11 degree for the fine and coarse SPH spacing, at the h_c/s of 0.55. (0.03 degree is about 0.025% DWL trim by the bow, and -0.11 degree is about 0.1%DWL trim by the stern.)

The trim changes with h_c/s ratio because increasing the contact thickness effectively increases the size of the underwater shape of the hull in a direction normal to the surface of the hull, but without changing the mass or the location of the Centre of Gravity (CG). As the hull effectively becomes larger, the trim will change as the location of the centre of buoyancy and the location of the centre of flotation will change at different rates unless the hull is symmetric about the LCF. In the case here, the AMECRC09 hull vessel is more full in the aft sections than in the bow, and so the trim will change as contact thickness changes, as shown in Figure 4-29.

The distance of the mean water surface to the DWL for the simulation results in Table 4-5 were determined at the location of LCF at the design condition of level trim. For each of the particle size simulations the vessel did not trim level at equilibrium; for the fine particles the vessel trimmed by the bow, and for the coarse particles the vessel trimmed by the stern. For each of these cases the location of the LCF at equilibrium would have been different from the level trim condition, and so the measurement of the DWL would not have been accurate.

Locating the LCF for the vessel using the software for SPH simulation is not trivial, as it is a general purpose FE tool. Consequently the true DWL calculations have not been performed.

A conclusion that can be made is the error in displacement will be less than that shown in Table 4-5. Also, the error in displacement in Table 4-5 is within the bounds defined earlier when the breadth instead of length of the vessel is used as the principal dimension.

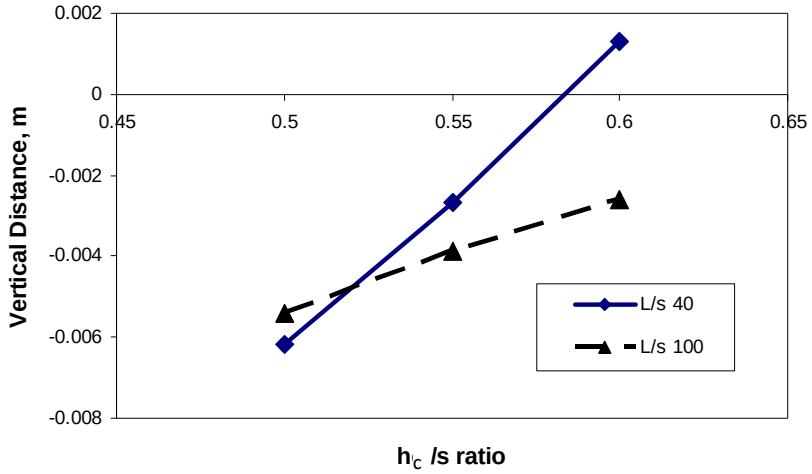

Figure 4-28. Effect of h_c/s ratio on location of DWL of AMECRC09.

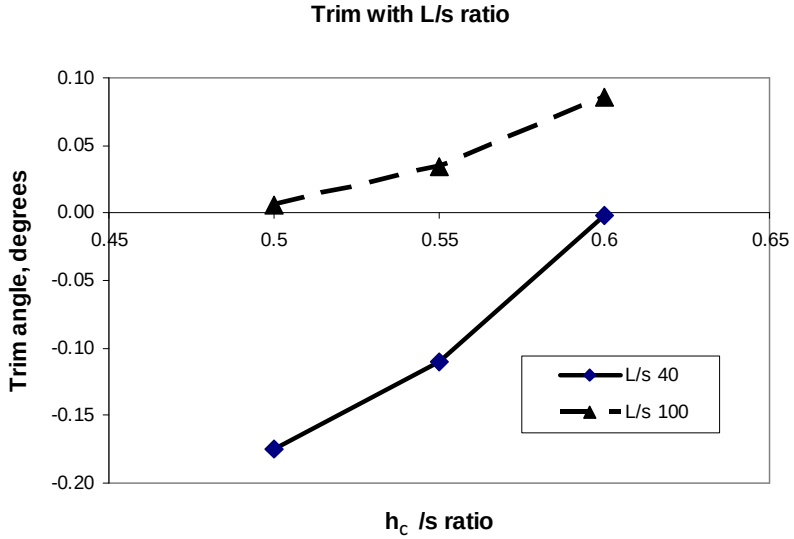

Figure 4-29. Effect of h_c/s ratio on Trim of AMECRC09 .

Figure 4-30 shows the vertical location of the CG with time for the different L/s ratios for the hydrostatic test simulation. Figure 4-31 shows the trim angle with time for the L/s ratios for the hydrostatic test simulation. These figures show the response of the vessel is less sensitive to the value of h_c/s when the particles are smaller.

Although not important for hydrostatics, the oscillations apparent in Figures 4-30 and 4-31 indicate less damping of the motions for the L/s value of 100. This is important for the response of ships in waves. In the simulations here, the SPH parameters were held constant and not scaled according to the guidelines of Section 2.8 to ensure equivalent viscosity, hence the finer SPH particles display a lower "apparent" viscosity.

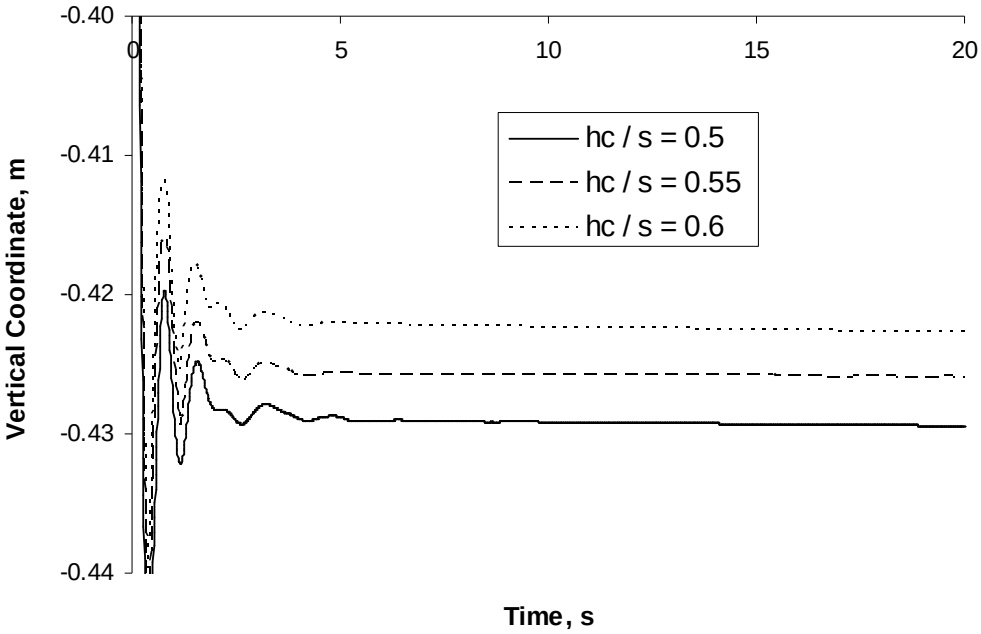

a) L/s = 40

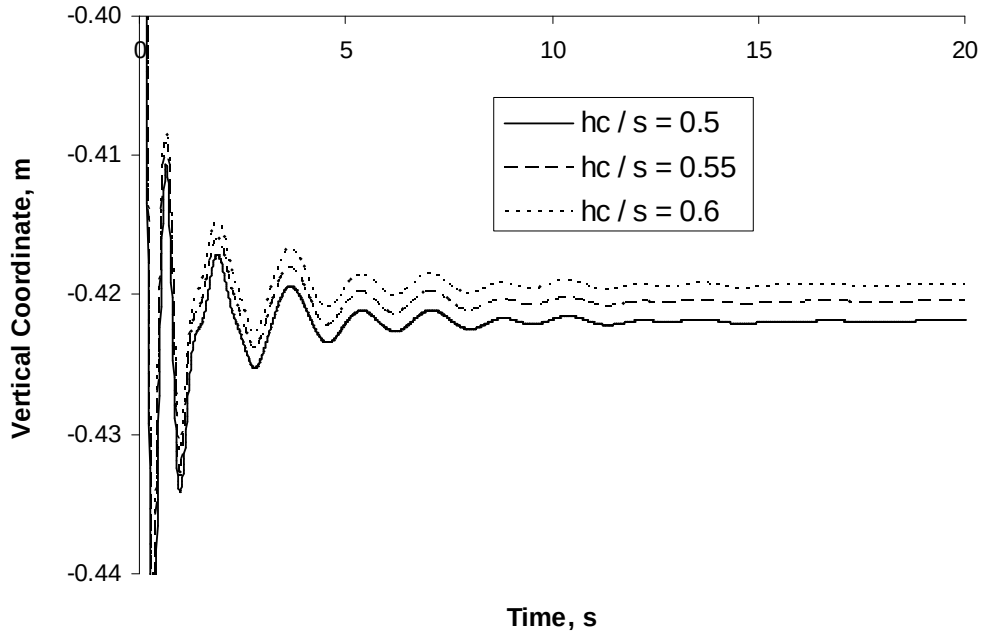

b) L/s = 100

Figure 4-30a) and 4-30b). Vertical location of the CG with time for h_c/s ratios of 0.5, 0.55 and 0.6.

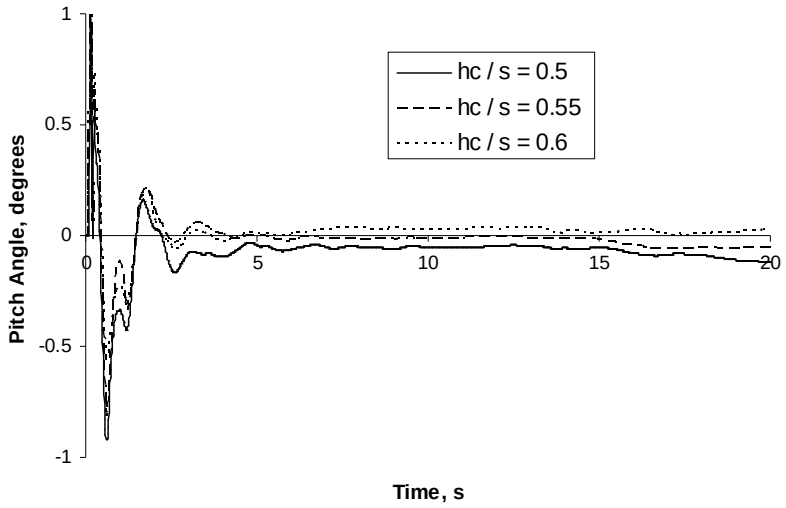

a) L/s = 40

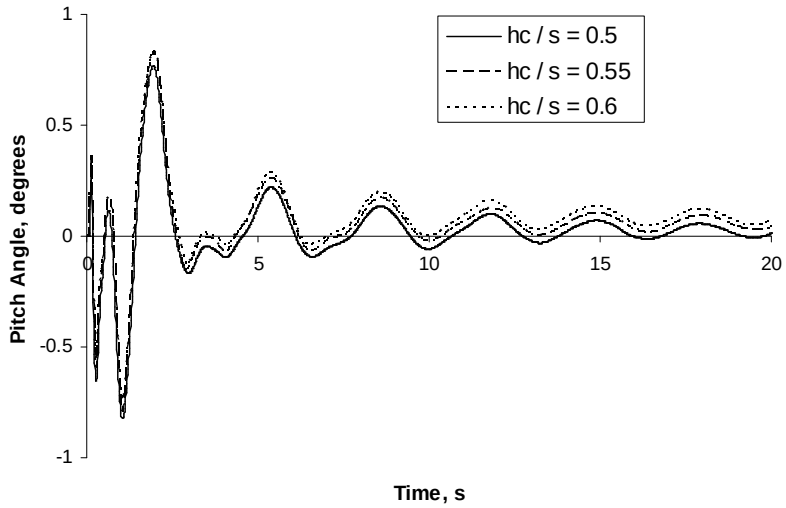

b) L/s = 100

Figure 4-31a) and 4-31b). Trim with time for h_c/s ratios of 0.5, 0.55 and 0.6.

McCue et al (2006) reported that finer particles give less damping when modelling fluids with SPH. The difference between the L/s ratios of 40 and 100 provide some guidelines as to where the practical limits for particle size lie for this particular problem. The SPH parameter set can also influence the damping, implying that particle size and SPH parameters need to be chosen to produce consistent behaviour, as discussed in Section 2.8.

4.13 *Total Vertical Force of a Vessel Moving Forward in Calm Seas*

A brief study of the AMECRC09 hull as it transitioned from a stationary equilibrium to a steady forward speed in calm water was made to ensure the SPH technique and rules developed for hydrostatics remain effective for a hull moving forward.

The simulation process had the hull lowered into the water under the action of gravity for 5 seconds during which the hull achieved hydrostatic equilibrium. From 5 to 7.5 seconds the hull was accelerated to 2m/s by a velocity boundary condition acting on the CG of the vessel. From 7.5 to 15 seconds the vessel was at a constant speed of 2 m/s (Froude number of 0.5).

Figure 4-32 shows the speed of the hull with time and the net vertical force (moving average of 100 data points at a sampling frequency of 100 Hz) of the water on the hull. The net vertical force commenced at zero at time zero, when the hull was out of the water. The force then increased and fluctuated briefly until the boat floated in hydrostatic equilibrium at about 2 seconds. The vertical force on the hull then remained essentially constant as the hull was accelerated and retained a constant forward velocity.

The key observation here was that the net vertical force acting on the hull remains essentially constant across the range of speeds considered. Small fluctuations in the vertical force are expected as the hull achieves dynamic equilibrium – sinkage and trim. The contact force algorithm has no ability to determine the components of this vertical force, ie it cannot distinguish between the force due to displacement and the force due to dynamic lift acting on the bottom of the hull. The important feature is the net vertical force was equal to the weight of the vessel as the balance between displacement and hydrodynamic forces varied.

The net vertical force from Figure 4-32 was 62.8 N, which corresponded with the weight of the half-model of 6.4 kg.

Figure 4-33 shows a plot of the sinkage of the hull with forward speed for experiment and predictions by SPH. The sinkage has not been normalised for these plots. Up to Froude number of 0.5 the sinkage predicted by SPH is comparable to the experimental results, but beyond Fr 0.5 the sinkage by SPH is severely overestimated.

Figure 4-34 shows a plot of the trim of the hull from experiment and by SPH. Here the results above Fr 0.5 are close to the experimental results, whereas below 0.5 the SPH grossly over predicts the trim of the hull.

The reason for these discrepancies is not immediately known. A possible cause stems from the different configuration used for the experimental work compared to the SPH model setup. For example, in the experimental work the total forward thrust was applied through the forward towing post located on the waterline of the vessel (Bojovic 1995). For the SPH model the velocity boundary condition had to be applied to the Centre of Gravity of the model, which was located about 25mm above the waterline.

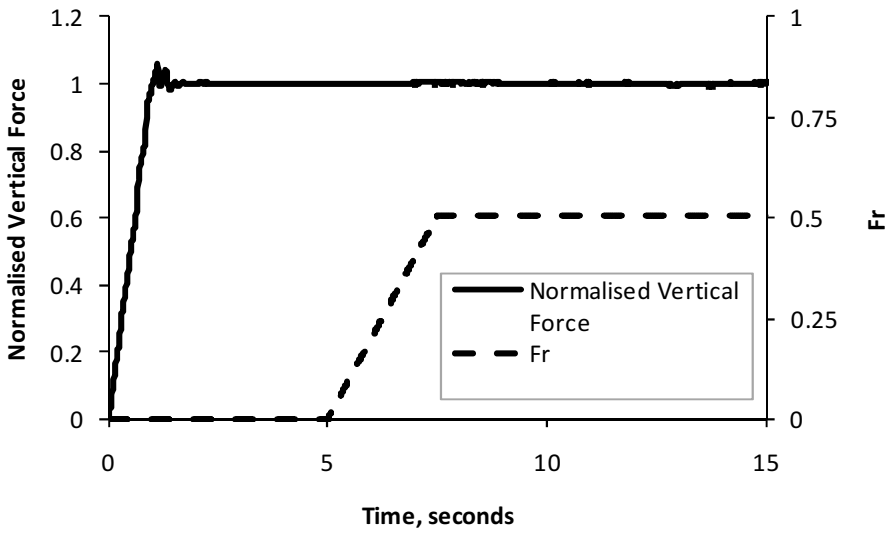

Figure 4-32. Normalised vertical force on the hull and forward speed from SPH predictions with time, as the hull transitions from stationary to steady forward speed.

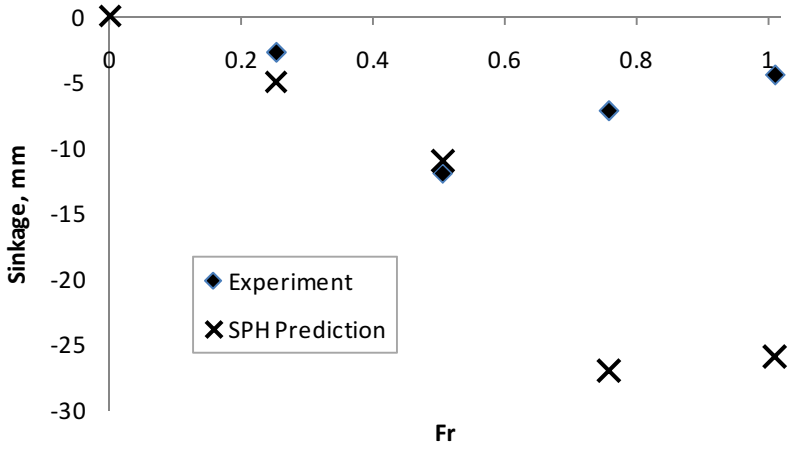

Figure 4-33. Sinkage of the hull at forward speed, experiment and SPH predictions.

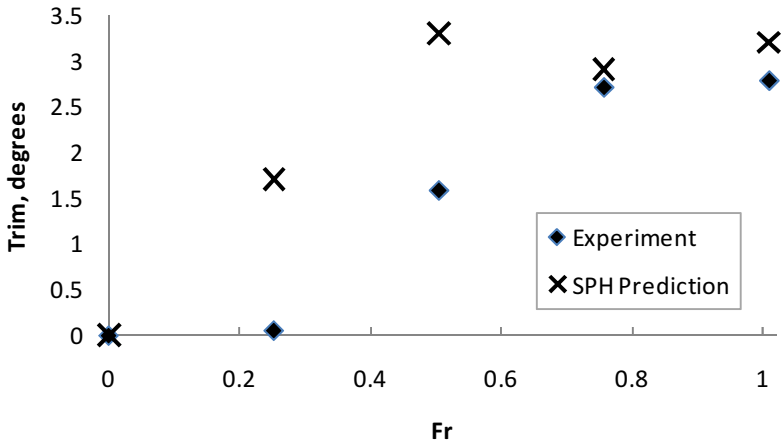

Figure 4-34. Trim of the hull with forward speed, experiment and SPH predictions.

4.14 *Summary of Hydrostatic Studies*

In conclusion, it was found that achieving the correct buoyant force for a submerged body was primarily dependent upon two geometric ratios:

a) principal dimension to the particle spacing; L/s, and
b) contact thickness to particle spacing ratio, h_c/s.

Of these two parameters, the first ratio, the object size to particle spacing ratio, L/s, had the greatest effect on the accuracy of the predicted buoyant force. The larger this ratio, the more accurate was the predicted buoyancy force. The L/s ratio also determines the number of particles required for the simulation model (assuming consistent sized SPH particles throughout the fluid domain), with a doubling of the L/s ratio producing an 8-fold increase in the number of particles required in the simulation model. Finding a suitable value of this ratio was necessarily a compromise for practical computing with the resources available.

The second ratio, the contact thickness to particle spacing ratio, h_c/s, had a smaller effect, but still influenced the accuracy for a given L/s ratio. Although the true value of the h_c/s ratio was found to be shape dependent, it was shown that a generic value of h_c/s equal to 0.55 times the initial SPH spacing (for orthogonally arranged particles) produced consistently accurate results for common shapes.

Using a slightly less than optimal h_c/s ratio of 0.5 (for reasons explained in Section 4.4), the accuracy as a function of L/s was shown in Figure 4-7 to be about 1% for an L/s of 20, reducing to an error of about 0.01% for an L/s of 40 for a typical ship shape, taking note that the critical dimension L is likely to the be the beam of the vessel.

Hence the L/s ratio can be used to estimate the error in the buoyancy force from the simulation, or conversely if a desired accuracy is required, the approximate L/s ratio can be determined.

The same rules were applied to objects floating on a free surface, however the buoyancy force was not influenced by the h_c/s ratio. Instead the draught of the vessel and the trim changed, as the h_c/s ratio effectively modified the underwater shape of the vessel in a direction normal to the vessel surface, as demonstrated in Section 4-12.

In summary it is recommended to use an L/s of not less than 20, with an h_c/s of 0.55 for initially orthogonal particle distributions. A greater L/s ratio should be used if computational resource allow.

As outlined at the end of Section 4.4, and as experience is acquired with the simulation technique described here, it may be evident that the length of the vessel, L, is not the best parameter to use for the rule of thumb to determine the SPH spacing dimension. It is likely the ratio will be case dependent – it is envisioned that for narrow hulls the critical dimension may be the beam, or for shallow vessels it may be the draught.

5 Non-Linear Free Surface Flows

Two physical scenarios that develop complex and violent free surface flows are breaking waves and green-water on deck. These flows are often quite challenging to model with conventional finite element CFD techniques. The SPH method is well-suited to the modelling of such complex free surface flows, as will be demonstrated by the controlled "dam-break" benchmark case.

The test case presented here, and others similar to it, have previously been solved using SPH (Issa and Violeau 2006, Abdolmaleki 2007). The presence of a dry or wet floor to the dam break tank has also been shown by the SPH technique to influence the developed wave behavior. For example, a wet floor causes the advancing water surge to have a notable hump and the wave velocity is slower than for a dry bed (Violeau and Issa 2007, Crespo *et al.* 2007, Crespo *et al.* 2008, Groenenboom and Cartwright 2009).

The aim here is not to re-validate the SPH technique for these non-linear flow scenarios, as they are not directly relevant to ship motions in regular waves, but the aim is to provide a tangible demonstration that the SPH technique being used here may one day be extended to the study of ship motions in non-linear waves.

5.1 *Reference Data*

The reference "dam-break" data is Test Case 2 from the "SPH European Research Interest Community" (SPHERIC, Test Case 2, 2006, Issa and Violeau 2006). The reference provided a detailed schematic of the experimental setup, a video of the experiment, pressure sensor and height gauge data as a function of time, and the results of an SPH solution to the problem. The SPH and finite element representation used for this work is shown in Figure 5-1.

The setup consisted of a rectangular tank with water constrained to one end of the tank by a vertical wall, the vertical wall in essence being the dam. The "dam-break" was simulated by rapidly removing the vertical wall, allowing the water to flow into the empty end of the tank. A small box fixed to the tank floor provided an obstacle to the oncoming fluid, producing a complex flow pattern with a mixture of spray and solid water. The small box was representative of a container on the deck of a ship.

The schematic with dimensions is shown in Figure 5-2. The tank was 3.2m long, 1m wide and 1m tall. Four height probes on the centreline of the box recorded the water height at the locations shown. Pressure sensors were located on centreline of the front (facing the dam) and top faces of the small box at the locations shown in Figure 5-3.

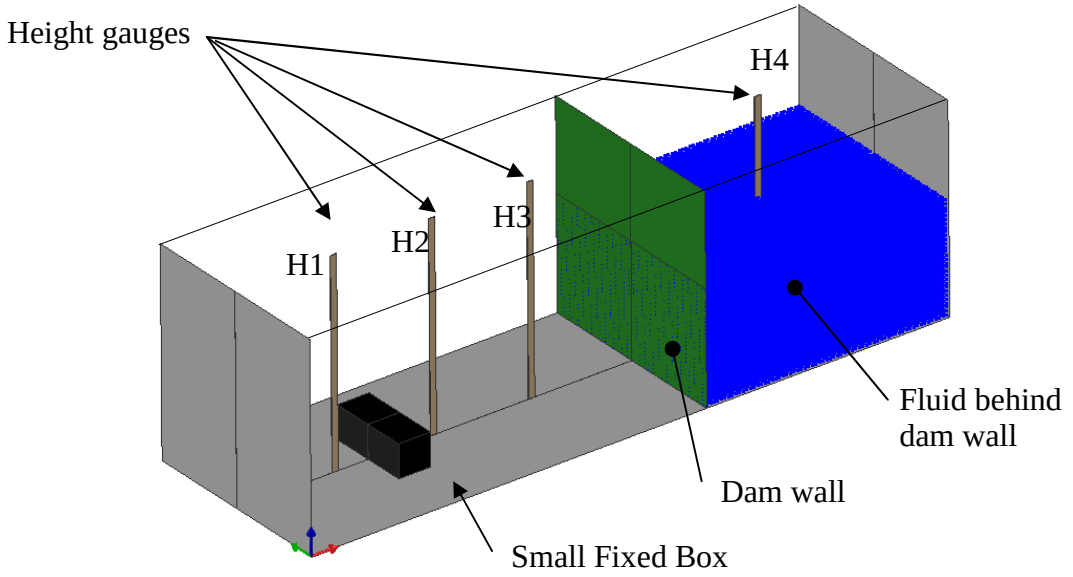

Figure 5-1. SPHERIC Test Case 2, 3D Dam Break problem.
(The tank side walls have been removed for clarity.) (Issa and Violeau, 2006)

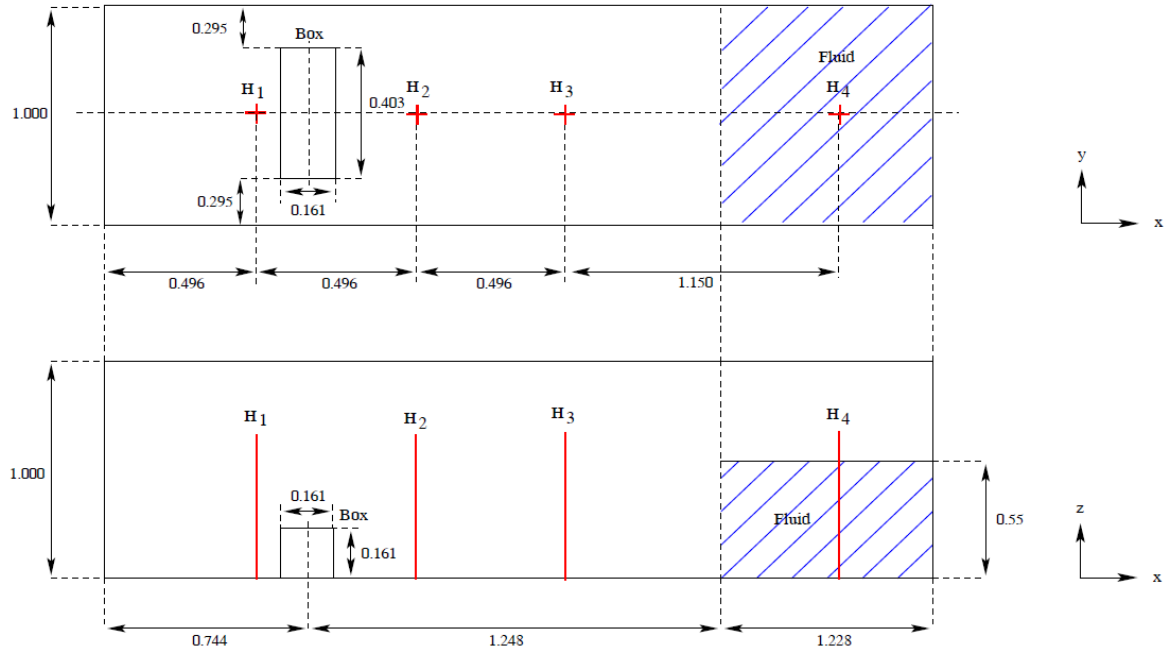

Figure 5-2. Schematic of SPHERIC Test Case 2 from Issa and Violeau (2006). (Dimensions in metres.)

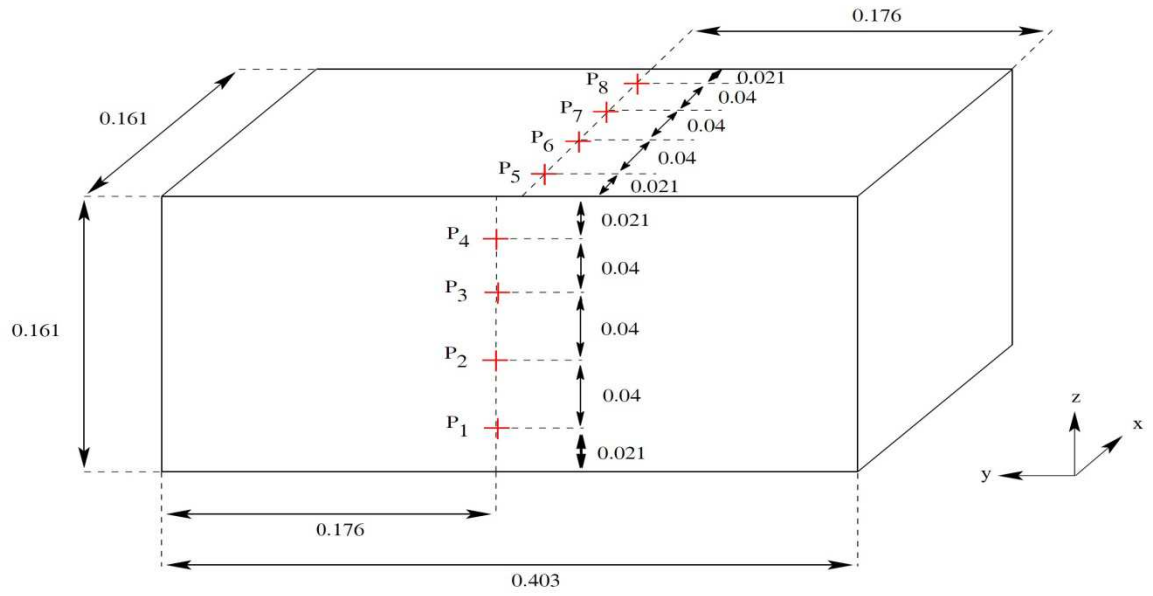

Figure 5-3. Location of pressure sensors on the small fixed box from Issa and Violeau (2006). (Dimensions in metres.)

5.2 *SPH Model of the Dam-Break Scenario*

The model shown in Figure 5-1 was constructed using SPH particles and finite elements according to the dimensions of the schematic in Figure 5-2. This numerical model was a half-model in three dimensions (3D) with symmetry along the centre-line. The tank and box were modelled using shell elements. The dam wall that was physically raised in the experiment was also modelled with shell elements. In the numerical model, instead of raising the elements to allow the water to flow underneath as in the experiment, the contact algorithm that prevents the SPH particles moving through the wall was turned off after the water had settled, and this allowed the water to proceed as if the door had been instantaneously removed.

The simulation was run for 6 seconds in total, with the first 0.5 seconds allowing the SPH to settle, at which time the dam wall was released. Numerical results (for producing graphs) were output at 1ms intervals and graphical results (images) were output at 50ms intervals.

The predicted water depth at each gauge was derived from the area of each gauge in contact with the SPH divided by the width of the gauge. The predicted pressures on the front and top faces of the box were derived from the respective component of the contact force of the SPH to appropriate box face divided by the area of the box face. The noise in the raw data was smoothed using a moving average, as shown previously in Figure 4-2.

The reference document (SPHERIC, Test Case 2, 2005, Issa and Violeau 2006) provides results of a prediction using SPH with a spacing of 18.3 mm for the SPH particles. The basis for this spacing was that it provided a “reasonable” number of 30 SPH particles in the vertical

height of water behind the dam wall. It should also be noted that the tank and small box in the reference were constructed using fixed SPH particles because the research code used by Issa and Violeau (2006) did not have capability for shell elements. Hence all the physical features within their numerical model had to be represented by SPH particles. In contrast, the tank and the small box were modelled using flat shell elements in the work presented here.

5.2.1 2D Model of the Dam-Break

A brief study on the effect of SPH particle spacing was conducted in two dimensions (2D) for computational speed. A SPH spacing nominally equal to the reference data was used as a benchmark, with half and twice the spacing also used for comparison. The actual spacings used were 9.03 mm, 18.06 mm and 36.12 mm.

The detail of the predicted gauge height at gauge 4 was used to assess the suitability of the water discretisation into the SPH particles. i.e. the smoothness and relative feature clarity of the predicted wave height was used to assess the adequacy of the SPH particle size.

Allowing the 3D model to behave as a 2D model was achieved by having SPH particles in the XZ plane of the model, and restricting the SPH particles to move only in this XZ plane. The summation characteristic of the SPH algorithm was adjusted also to ensure that the weighting function was normalised over the plane instead of a 3D volume.

SPH parameters and material parameters were also adjusted with SPH size to ensure the behaviour scaled correctly as explained in Chapter 2.

Figure 5-4 shows the predicted water heights in 2D as functions of time at gauge 4 for the three different SPH spacings in non-dimensional form. Water height has been non-dimensionalised by dividing by the initial water height of the dam, h_w, and time has been non-dimensionalised by $\sqrt{(h_w/g)}$, where g is gravity, as used in Nielsen (2003).

Gauge 4 is located within the dam, and so the water height at this gauge begins at a height equal to the water depth in the dam.

The shape of the curve of Figure 5-4 is characterised by the initial drop in water height after the dam is “released”, followed by two small upward steps in water height. These smaller upward steps occur as the water surge passes the gauge location, firstly from the reflection from the far wall, and then the near wall.

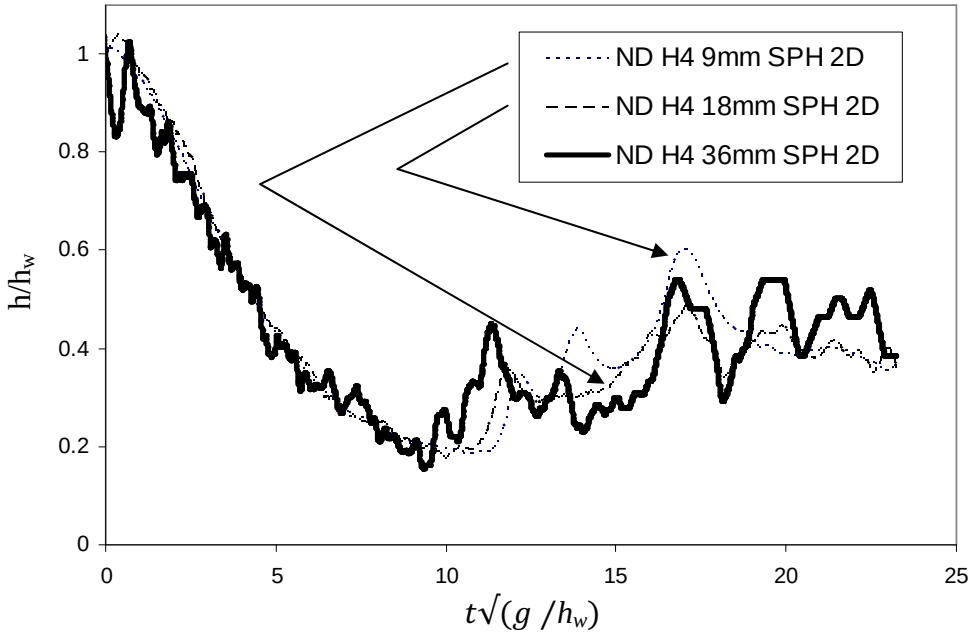

Figure 5-4. Water height at gauge 4 of 2D simulations with different size SPH particles.

The predicted water height at gauge 4 using 36 mm particles in Figure 5-4 was not a smooth curve as function of time, whereas the predicted height using 18 mm or 9 mm spacings are comparatively smoother. Similarly the visual representation of the reflected wave was better defined for the smaller particles, whereas the shape was less well-defined for the 36 mm particles. Both of these effects are most likely due to the 36mm spacing being too coarse.

From this comparison the 18 mm particles were considered to be adequate for the 3D simulation, in agreement with the SPHERIC reference document for this test case. 9 mm SPH would give much better resolution of splash and water height, but at a cost of eight times the CPU effort, which was considered prohibitive for this study.

5.2.2 3D Model of the Dam-Break

The 3D finite element and SPH particle model is shown in Figure 5-1. SPH particles fill the volume behind the dam wall to a height of 0.55m requiring 54,270 SPH particles on a spacing of 18.06 mm.

The 2D and 3D SPH predictions and the experimental results for the water height at the location of gauge 2 are compared in Figure 5-5. Gauge 2 is just in front of the small box. Figure 5-6 makes the same comparison for gauge 4, which was in the centre of the dam.

The 3D predictions using SPH have the correct magnitude and behaviour, although the details are not perfectly aligned in time. The 2D results generally show a different profile with non-dimensionalised time due to the change in topography in 3D that is not present in the 2D simulation.

The reference data contained a movie of the experimental results to allow a visual comparison with the SPH predictions. The most obvious difference between experiment and SPH results was that the experiment exhibited a large amount of splash and spray, whereas the SPH prediction did not develop as much splash and spray, due to the discrete size of the SPH particles being much larger than the very fine droplets of the water in the experiment. The presence of spray in the experiment could be influencing the measured gauge heights and may contribute to the difference seen between the experiment and the predictions using SPH, for example in Figure 5-5 for Gauge 2, which is immediately in front of the small box where much spray was developed from.

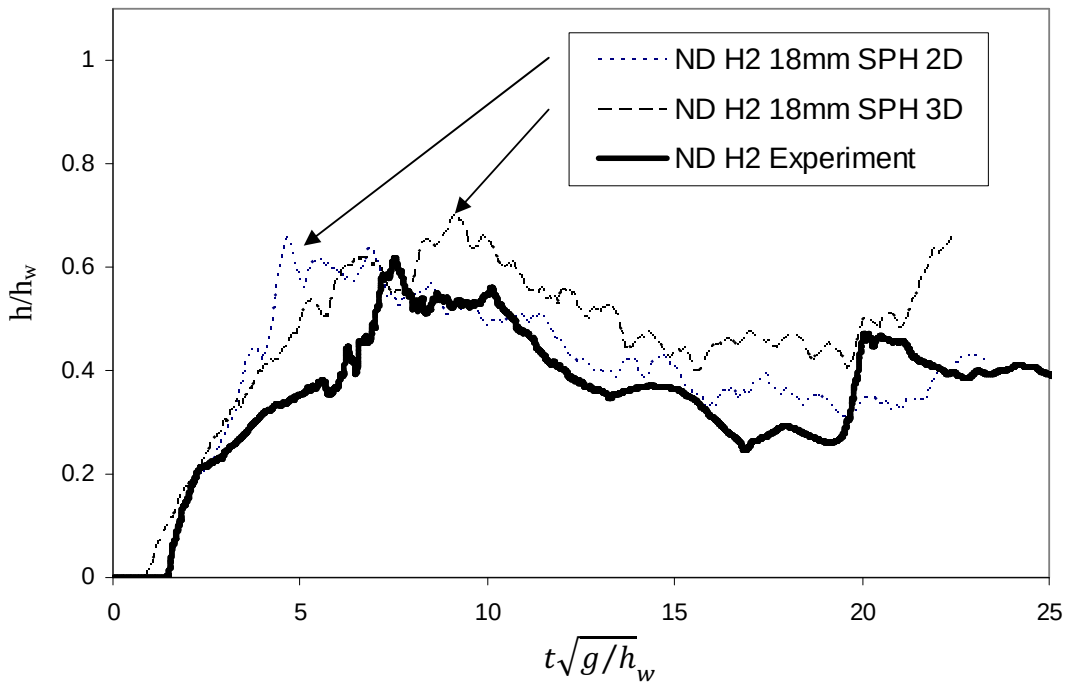

Figure 5-5 Height Gauge 2 - Experiment and SPH results.

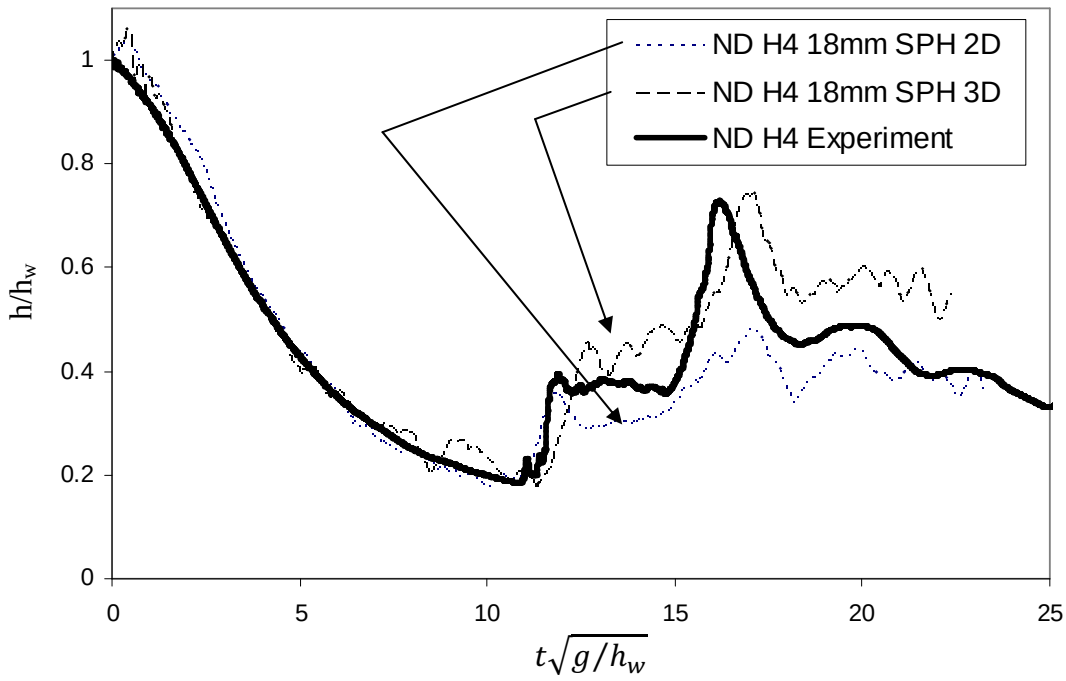

Figure 5-6. Height Gauge 4 - Experiment and SPH results.

Figures 5-7 and 5-8 show the predicted pressure on the front (P2) and top (P7) faces of the box using SPH and the experimentally measured pressure as functions of time. The predicted pressure was derived by dividing the contact force by the surface area of the face. A moving average of 20 samples was used to reduce the noise from the force signal. The predicted pressures compare well to the experimentally measured pressures in magnitude, although after 4 seconds the predicted values lag the measured results. (The frequency response of the experimental data was not stated in Issa and Violeau (2006).)

Figure 5-9 shows a few states of the SPH prediction of the dam break as it progresses. The splash forming around the box is well defined. The vertical strips are the location of the height gauges.

Figures 5-10a and 5-10b show the experimental result and the prediction by SPH at a few discrete times. Of note is the extent of fine water spray associated with the splash in experiment. In SPH the level of this spray development is restricted by the discrete size of the SPH particles, and so the SPH prediction does not develop a visually compelling spray in comparison to the experiment.

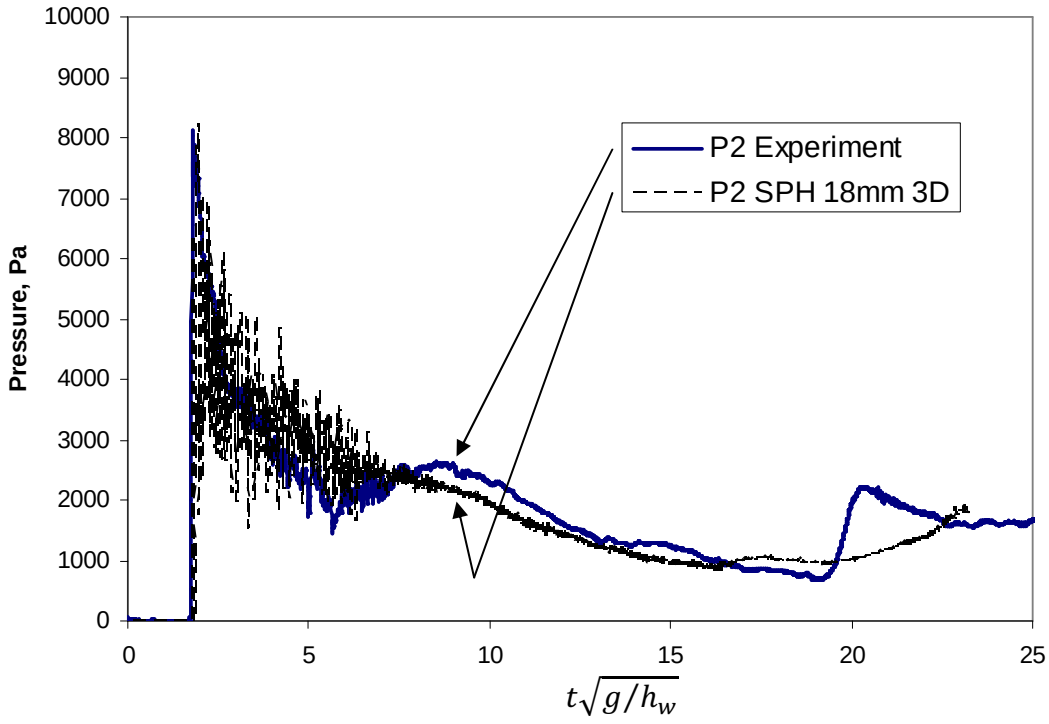

Figure 5-7. Pressure on the front face of the box in the path of the breaking dam from experiment and as predicted by SPH.

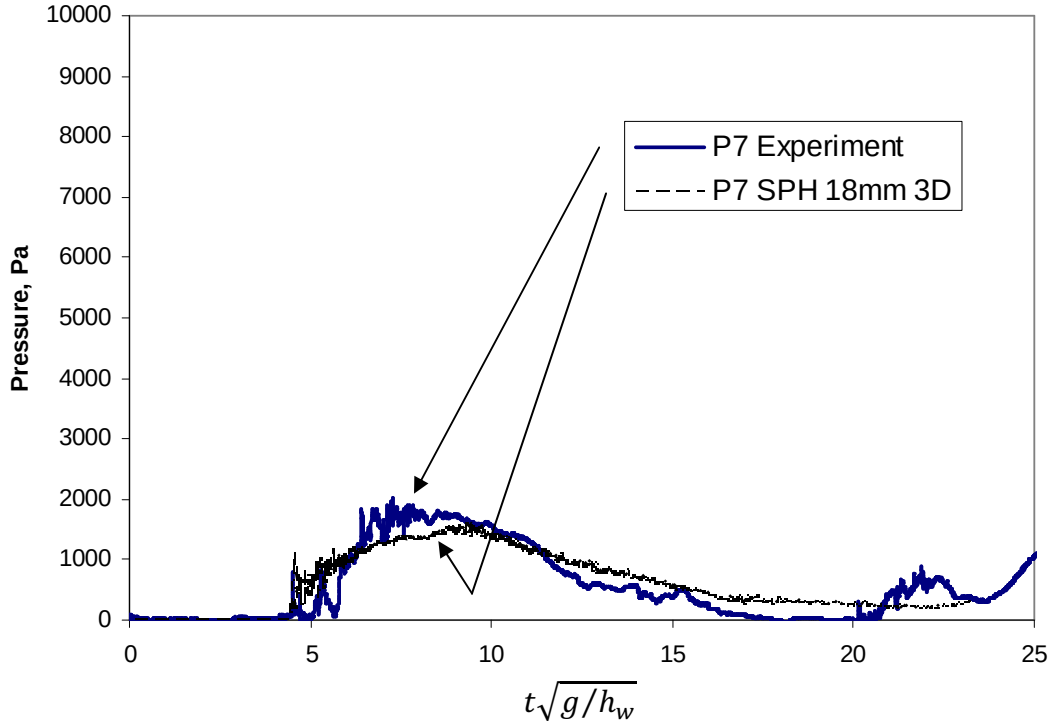

Figure 5-8. Pressure on the top face of the box in the path of the breaking dam from experiment and as predicted by SPH.

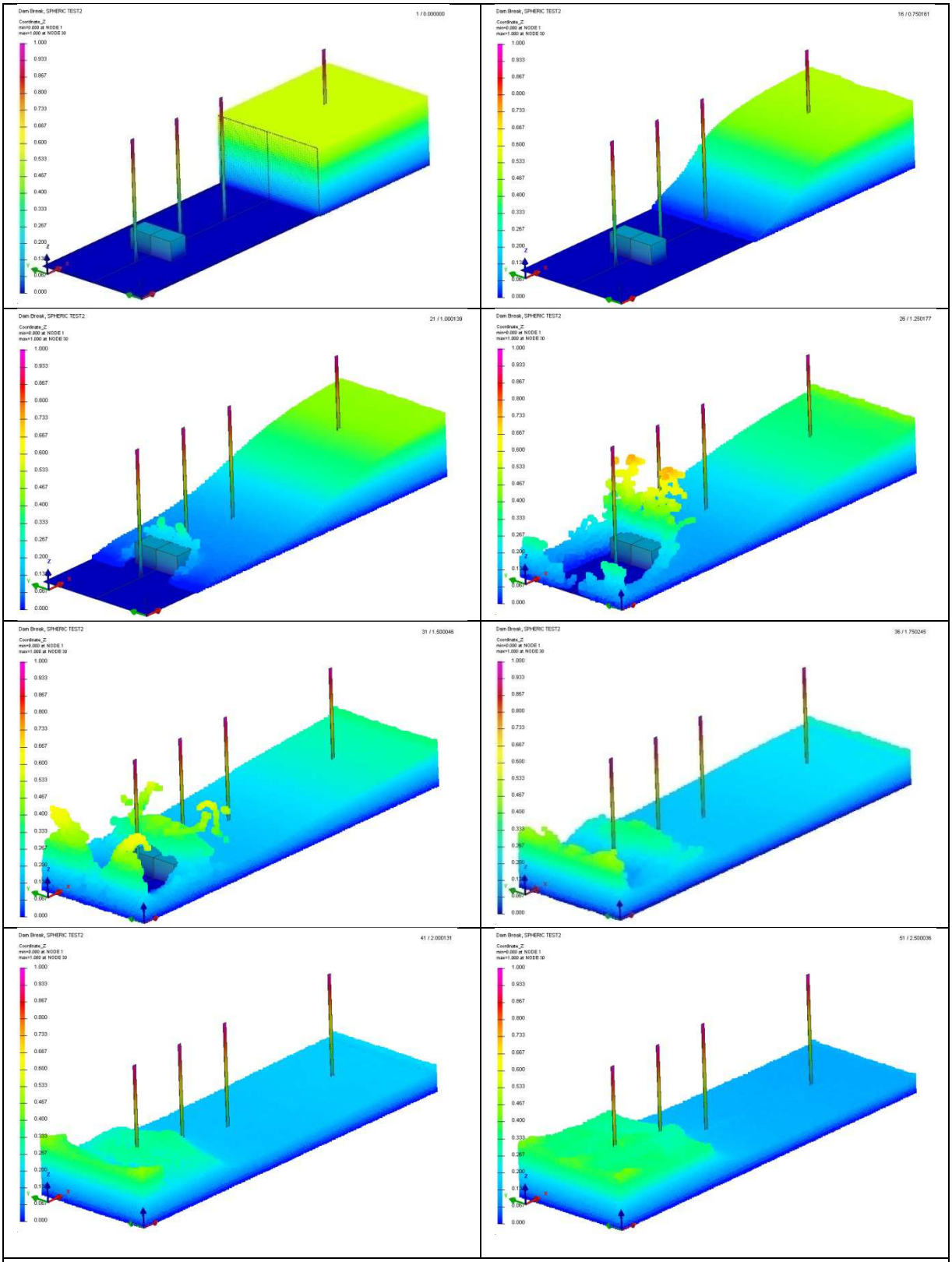

Figure 5-9. States of the Dam Break at 0.25 second intervals. Colour is vertical height.

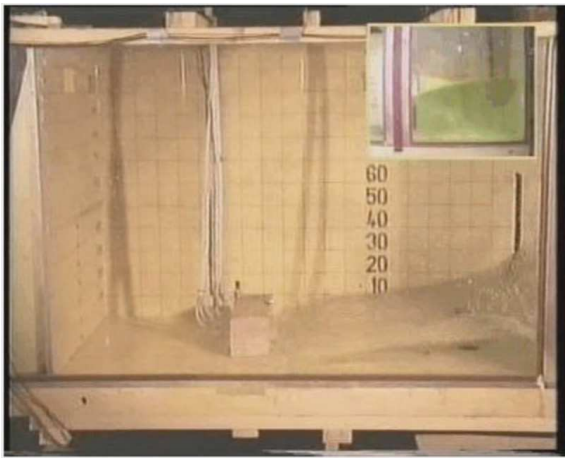

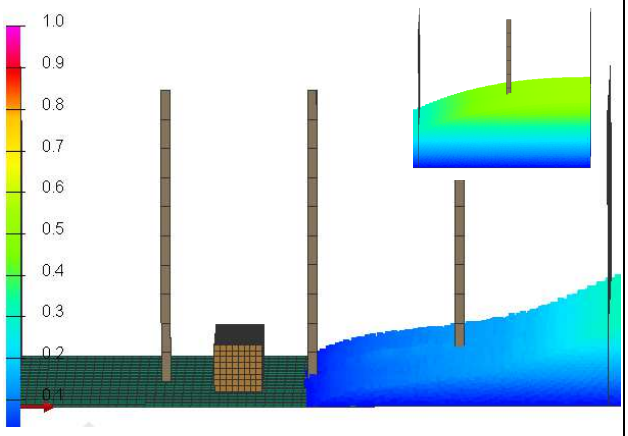

0.4 seconds

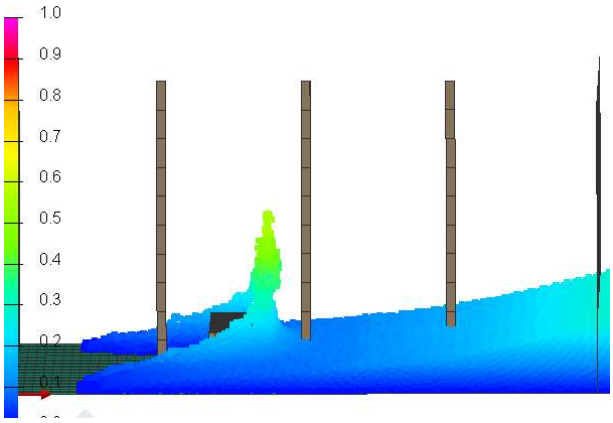

0.6 seconds

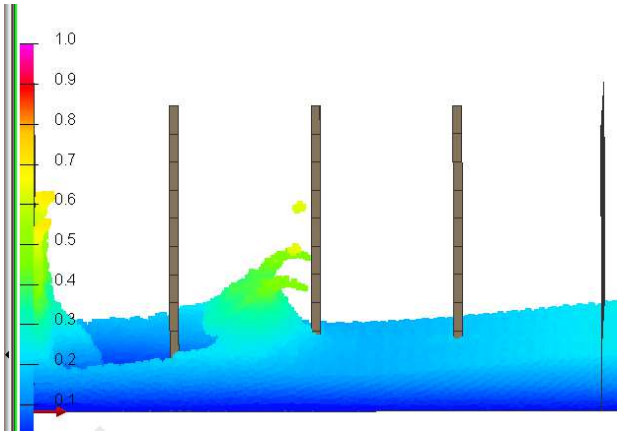

1.0 second

Figure 5-10a. Visual comparison of the experimental and SPH prediction at a few specific times. Colour is vertical height.

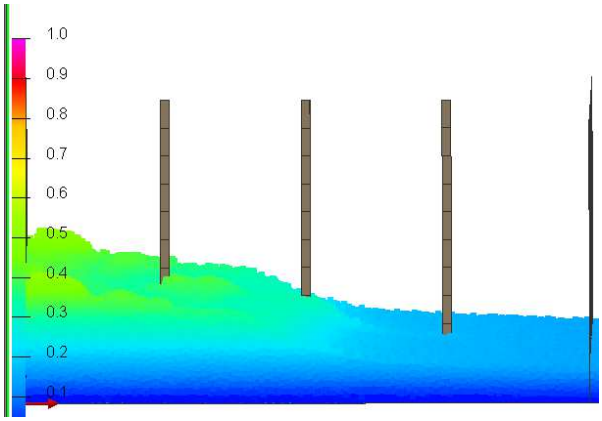

1.8 seconds

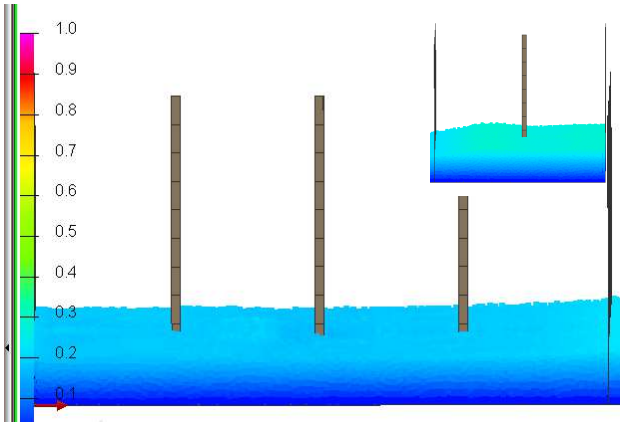

4.5 seconds – surge in SPH prediction lags that of the experiment.

Figure 5-10b. Visual comparison of the experimental and SPH prediction at a few specific times. Colour is vertical height.

5.3 *Summary of Free Surface Flows*

The dam-break simulation has demonstrated that the implementation of SPH to be used for this research is capable of capturing the wave-breaking and water-slamming characteristics with reasonable accuracy in terms of pressures and free-surface profiles.

Predicted pressures on the fixed box agreed with the results from the experiment for the early part of the simulation where the pressures were largest. Wave profiles predicted by SPH also showed reasonable agreement with the experiment. Splash development by SPH was not as well-developed as in the experiment because the SPH particles used were much larger than the fine water droplets that can develop in a real splash.

The predictions using SPH shown here had a distinct lag compared to the experiment, particularly in the later stages where the lag was up to 4 seconds. The reason for this progressive lag was a slower wave velocity, resulting in a greater lag as time progressed. This slower wave velocity is likely due to the artificially over-viscous behaviour of the SPH required for stability, as has been observed by DePadova et al (2009). Numerical stability is very relevant to the violent flow-regime with large pressure impulses seen in this example.

A brief study on the compromise between accuracy and computational effort for a 2D dam break confirmed that smaller SPH particle will reveal greater detail and smoother results for the flow evolution and pressures, albeit at greater computational effort. Smaller SPH particles also allow lower apparent viscosity whilst maintaining computational stability in the violent water impacts, and this could also reduce the lag that developed in the later stages of the numerical simulation.

6 Regular Waves in a Mesh-Free Environment

Work by the author in conjunction with others (Cartwright et al, 2004a and 2004b) illustrated that waves could be generated using the SPH technique. It was also shown that ship-like shapes of conventional and novel form expressed as a rigid finite element model could interact with the SPH waves.

At that time, the focus of the work was on severe waves, and the aim of the work was to demonstrate a capability in numerical analysis, rather than to validate one.

One of the more useful applications of the mesh-free applications is still thought to be the study of the response of ships and structures due to interaction with severe waves. However, as a precursor to that application some validation with regular waves for which there is ample data for correlation is required to build confidence in the technique.

This chapter reviews the characteristics of regular waves developed by SPH.

6.1 *Numerically Modelling the Towing tank*

As a first approach to modelling waves, a numerical simulation was prepared to generate regular waves by replicating the setup of a tow-tank. The initial study was in two dimensions, as shown in Figure 6-1.

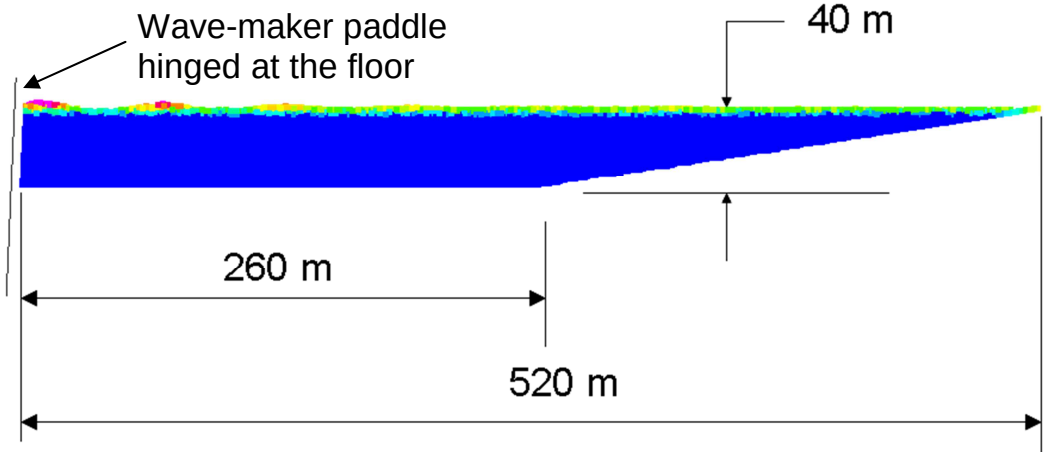

Figure 6-1. Full size tow-tank model for the wave study.

The tank was 520m long and 40m deep. It employed a rigid floor-hinged paddle wave maker at one end and a gently sloping beach at the other to reduce reflections. A wavelength of 60m was chosen to ensure deep water conditions for the depth of tank, yet retain a reasonable number of particles per wavelength. In this case, particles of 2m diameter were used. As noted in the Chapter 4, the location of the free surface can be determined to a location smaller than the diameter of the particles.

The paddle was oscillated about the tank floor to generate the waves. The paddle amplitude was chosen to give a wave height of 2m close to the paddle. The simulation was run for 120 seconds, which was about 20 periods of the 60m wavelength.

The numerical simulation successfully generated waves, however, the wave height reduced significantly along the length of the tank. This is shown visually in Figure 6-2, where the upper 10m of depth has been magnified about 100 times to show the diminishing 2m wave height over the 520m length of the tank. Note the SPH distributions are not representative of anything very much due to the vertical magnification (they are in fact still largely hexagonal in distribution). Normalised wave height as function of distance from the paddle is shown in the curve of Figure 6-3.

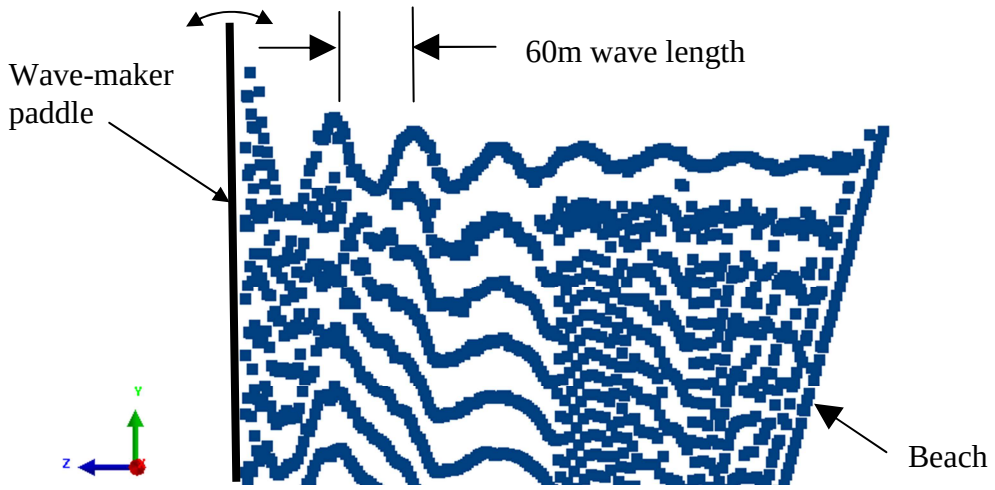

Figure 6-2. Wave height from the full-size wave tank decreased with distance from the wave-maker. (Wave height has been exaggerated in this image. The maximum wave height was about 2m.)

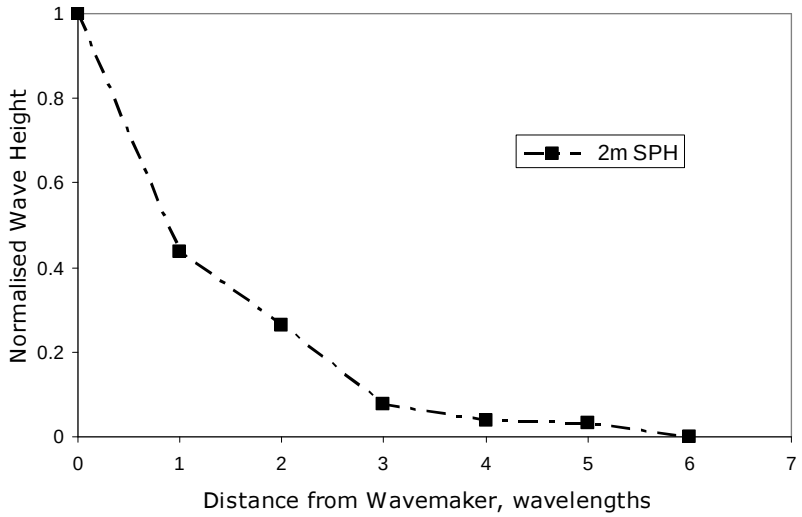

Figure 6-3. Normalised wave height with distance from the paddle for a 60m wave and 2m particles.

It is understood that the loss of wave height exhibited in Figure 6-2 is due to small amounts of energy being lost at each of the many numerical smoothing calculations performed (McCue et al 2004) as the wave propagates along the tank.

The parameter set used provided a reasonable compromise between the numerical stability and damping and was developed over many cases in the course of this work. The parameter set used is shown in Table 6-1. It is slightly less-damped (lower smoothing length to radius ratio, and lower artificial viscosity parameters),than those arrived at by Kalis (2007) for his work on free fall lifeboats using the same software.

Smaller SPH particles were reported by McCue et al (2006) to provide less dissipation. The use of smaller particles requires more computational effort, and so a compromise is required.

Table 6-1 SPH Parameter Sets

Parameter Set	Smoothing length to radius ratio	Smoothing length limits		Anti-crossing parameter	Artificial Viscosity coefficients	
		min	max		Alpha	Beta
Cartwright	1.8	0.0	4 x spacing	0.02	0.02	0.02

For the regular wave setup of Figure 6-1, different size particles were trialled to observe the effect of particle size. Figure 6-4 shows the wave height with distance from the paddle for 1m, 2m and 4m particles for a 60m wave length. Less energy dissipation is observed for the small particles, agreeing with the findings of McCue et al (2004), but is still unacceptable for ship motion studies.

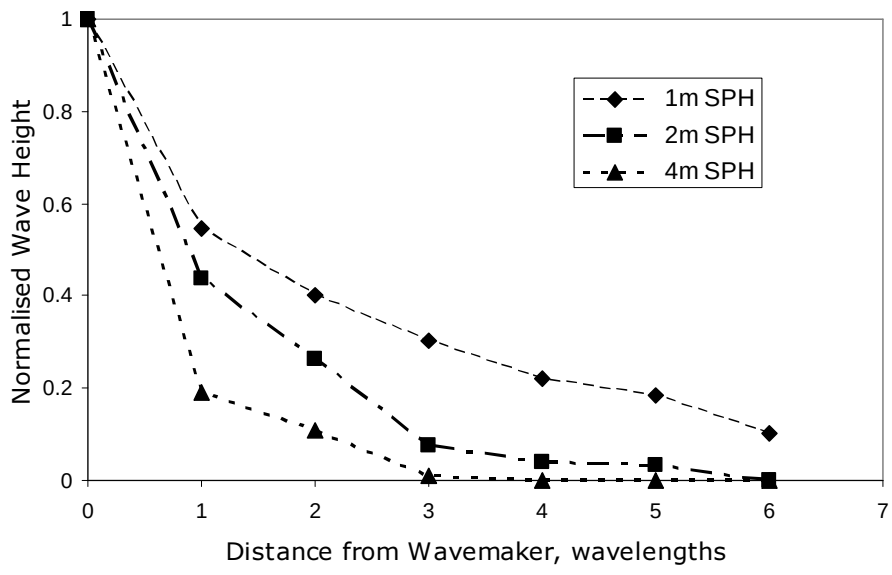

Figure 6-4. Normalised wave height with distance from the paddle for 1m, 2m and 4m particles.

The effect of SPH particle size on computation effort is shown in Figure 6-5, where the number of SPH particles and CPU time (in seconds) is shown for the 1m, 2m and 4m

particles. The CPU effort is linearly related to the number of SPH particles for these simulations. The CPU time for the 1 metre SPH simulation was 4300 CPU-seconds, or about 72 minutes on one CPU (Intel Xeon 2.4 GHz), or at best 18 minutes on a 4-CPU (reduction in CPU-time is less than linear with number of CPUs for the code used here).

Extrapolating the trend exhibited in Figure 6-4 to a particle size that would limit wave height loss to about 10% over the 6 wavelengths modelled here would require an SPH particle size of about 0.1m. Extrapolating the trend for CPU effort shown in Figure 6-5 to a simulation with 0.1m SPH would require 7,200 minutes (5 days) of CPU effort for a similar simulation in 2D. If the model was a 3D wave tank, of dimensions 100m wide, this would be 1000 particles wider than the present 2D model, requiring an estimated 7.2 million minutes of CPU time. This is impractical with the computing resources available to this project.

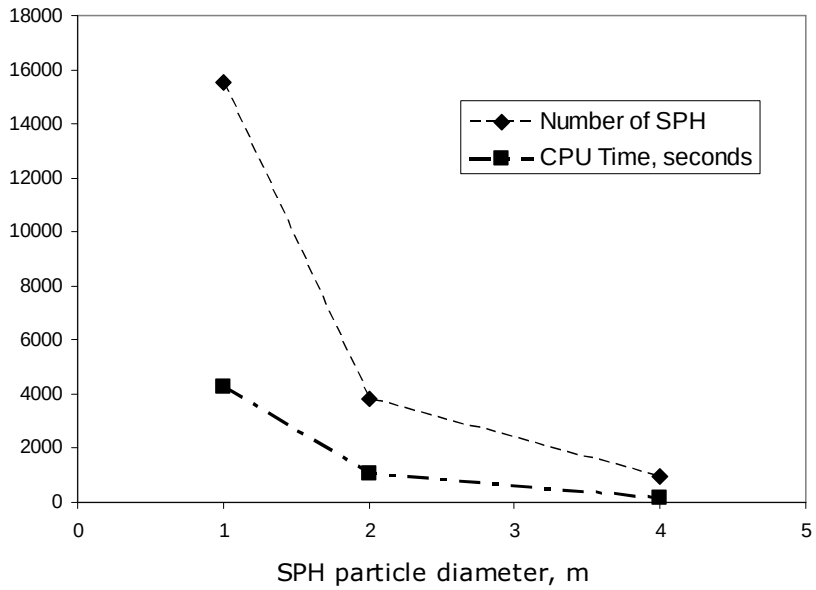

Figure 6-5. Computation time for 2D simulations using 1m, 2m and 4m particles.

More recent work (Jones and Belton 2006, Guilcher et al 2007) suggested an improved time-stepping algorithm as a possible solution to reducing the wave decay in the propagation of free surface waves, however this was not demonstrated. A still more recent work (De Padova et al 2009) also showed dissipation in the waves modelled by their custom code which presumably incorporated many of the improvements of recent publications. The simulated waves of De Padova et al (2009) included both regular and irregular waves, but were in a tank with a sloping floor, which ultimately led to breaking on a shore, so even those waves were not directly comparable to a constant depth wave tank for ship motion predictions. DePadova et al (2009) concluded that a small value of the empirical alpha coefficient of the artificial viscosity was required for numerical stability, but the result was still too dissipative for accurate wave reproduction.

Consequently, the generation of waves by replicating the wave tank physics with current SPH formulation and currently affordable computer power is not a viable approach to predict the response of a ship, as the waves developed are not sufficiently consistent in height along the tank.

6.2 *Moving Floor Technique*

A novel technique to generate non-decaying waves over any number of wave lengths has been developed for this work.

The approach is based on Airy wave theory (Lamb 1932) and the finite element modelling concept of sub-domains.

Sub-domains are a modelling technique used in finite element analysis and are merely smaller regions of a larger domain with controlled boundary conditions. Critically, the response of the sub-domain will be the same in isolation or if part of a larger domain so long as the conditions (say, forces and displacements for a mechanical system) on its boundaries are the same in each situation. Hence to study the response within a sub-domain, it is not necessary to solve the solution to the entire domain, but merely the solution to the sub-domain with appropriate boundary conditions.

Airy wave theory (or linear wave theory) states the water particles in a wave will follow the path of an orbit that is a function of depth and wavelength and sufficiently far from the floor.

Combining the concept of sub-domains and Airy wave theory, a wave tank was considered a sub-domain of an infinitely deep body of water with surface waves. The tank floor was considered as the boundary to the sub-domain and as such was divided into segments and were prescribed motions according to the Airy wave conditions at that depth. The paddle at the upstream end was retained and given motions according to the Airy wave conditions at that location also. This is shown in Figure 6-6 for a sub-domain that does not contain a beach.

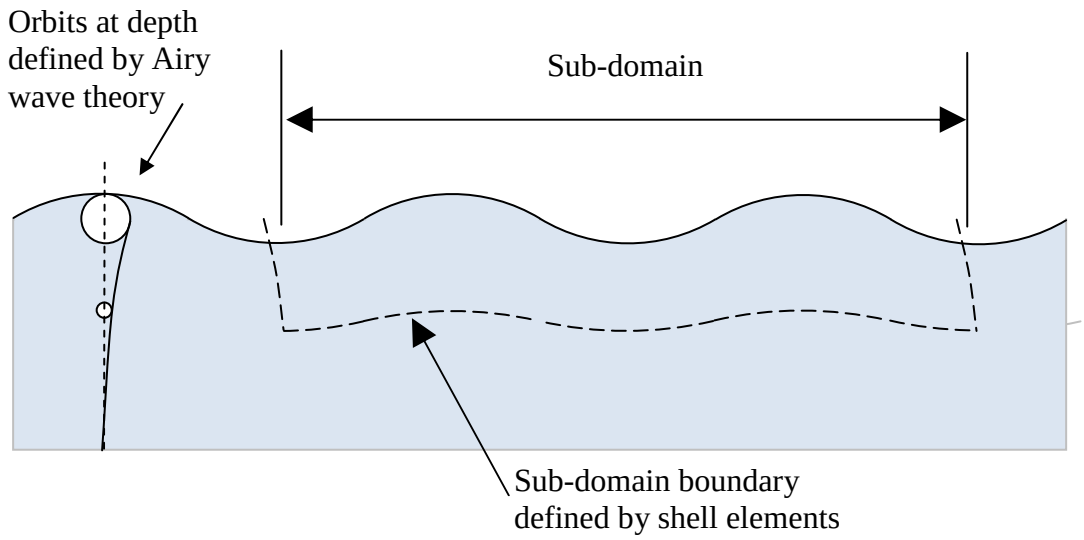

Figure 6-6. Concept of sub-domain boundary motions defined by Airy wave theory.

Applying this concept to the configuration of Figure 6-1, a sub-domain boundary was defined using shell elements at a depth of 15m. Eight shell elements per wavelength were defined for the floor, and the nodes of these elements were prescribed time-dependent dimensional

boundary conditions to enable a “moving floor”. Similar shell elements were described for the paddles at the up- and down-stream ends of the sub-domain.

The boundary conditions assigned to these moving shell elements were displacements as s function of time about a central point consistent with the Airy theory orbits for the water at the depth of interest. The rigid sloping beach was retained as in Figure 6-1. SPH particles adjacent to the moving floor shell elements had motion imparted to them by the contact interfaces described earlier.

The result was a wave that showed no loss of wave height along the tank, as shown in Figure 6-7 (expanded vertical scale).

Of particular interest is the near-uniform wave heights, and the SPH particles that are adjacent the moving floor elements that are neatly conforming to the shape of the moving floor. There is a rapid loss of wave profile over the rigid beach where there is no influence from the moving floor.

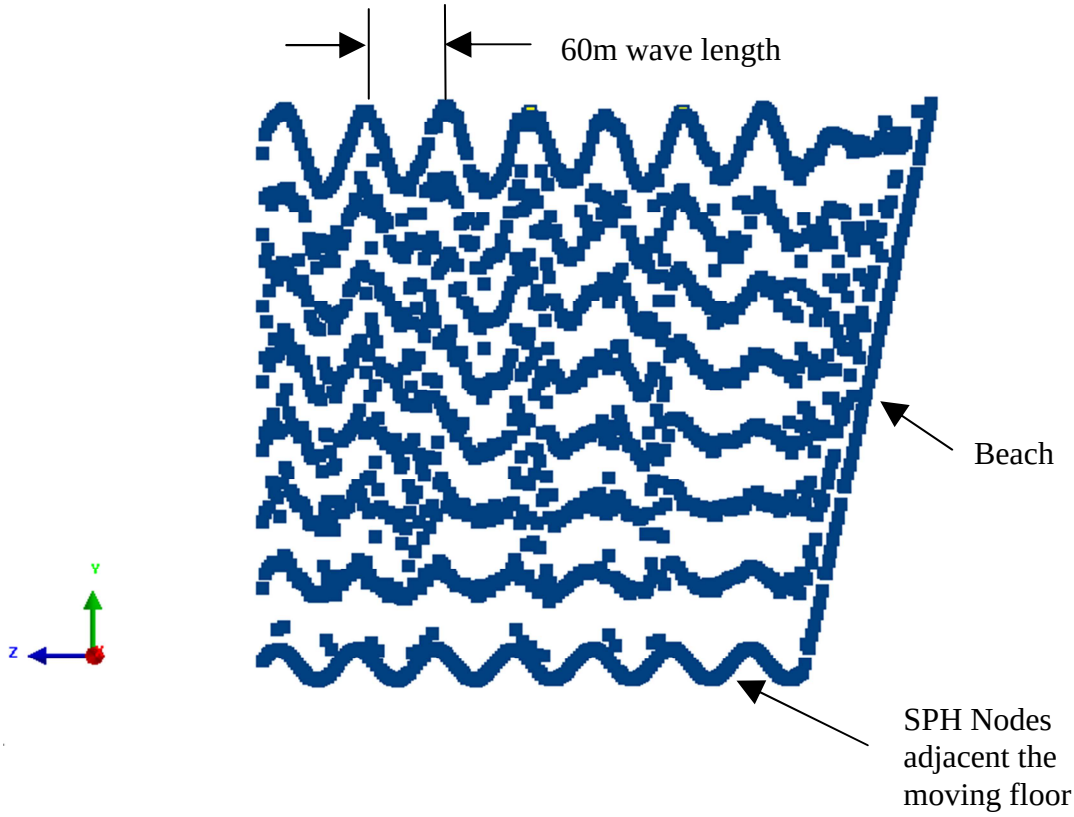

Figure 6-7. 2m wave height developed by the moving floor concept – exaggerated vertical scale.

In the simulation shown in Figure 6-7, the waves developed simultaneously everywhere along the tank in response to the moving floor. This reduced the time for fully developed waves to fill the tank. This was because the waves due to the moving floor are developed through the depth of the water, and not along the length of the tank as is the case for a single wave-maker at one end of a tank.

The moving floor technique does not overcome the losses inherent in the SPH formulations used here. Instead the moving floor relies on the interaction of a wave with the floor in shallow depths, but instead of taking energy out of the wave through interaction with a passive floor, the moving floor imparts energy into the wave. The motion of the floor determines the nature of the surface wave that is generated.

Waves are able to be developed at considerable distance from the wave maker paddle because the waves at those locations are being generated through the depth of the wave by energy from the moving floor. Hence the energy present in the surface wave has only propagated through the depth of the water, and hence the distance for energy loss through particle interactions is greatly reduced compared to a surface wave that has travelled along the tank from the wave maker.

The concept of developing the wave through the depth is unconventional, and is not obvious at all as to why it should work, when the floor amplitudes are considerably smaller than those that develop on the surface.

To demonstrate that the surface waves are generated from the motions of the floor, a wave tank without a paddle-type wave maker, and without a beach, was developed in simulation. For this model, periodic boundary conditions were used to give the behaviour of an infinite length of tank. Periodic Boundary Conditions (PBCs) are numerical domain boundaries where reactions are translated in the model space, so that particle interactions at one end of the tank are reproduced at the other end of the tank, so as to give the numerical effect of an infinite length of tank. Energy is input into the water from the motions of the floor. The result is shown in Figure 6-8, where 7 wavelengths of 2m waves are shown. The same wave is shown in Figure 6-9 with an amplified vertical scale for comparison to Figures 6-2 and 6-6.

The surface profile is not perfectly smooth. This is due to the discretisation of only 7 particles through the nominal depth of 15 metres. Due to the requirement that the particles develop a hexagonal packing arrangement, the packing of the particles must continually adjust for the varying depth between crest and trough. With particles of nominal 2m diameter, this necessitates continual rearrangement with the consequent un-evenness displayed. This effect is smaller with smaller SPH particles.

Figure 6-8. A 2m wave height on 60m wave length developed by the moving floor concept using periodic boundary conditions and no wave paddle-type wave maker.

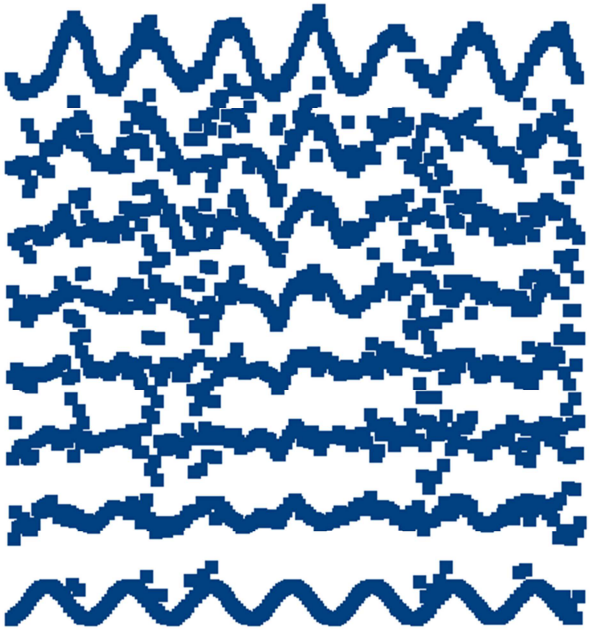

Figure 6-9. The same wave train from Figure 6-7, with the vertical scale exaggerated. The surface wave height was nominally 2m and the floor movements were 0.88m in diameter.

For this technique to generate waves the moving floor must be at a depth of less than one half a wavelength. Once the floor depth is defined the spectrum that can be generated will be restricted due to this depth. The work here is restricted to single frequency waves.

6.3 *Waves Generated using the Moving Floor Technique*

6.3.1 Wave Descriptions

A wave of frequency of 0.8 Hz and 50mm wave height has been developed using the moving floor technique. This corresponds to a h/λ of about 2% on a wave length of 2.43m. This wave is relevant to the model ship response of the AMECRC09 hull regular wave response (Macfarlane and Lees 1999) that is used for comparison to predictions obtained using SPH in Chapter 7.

A wave tank of a single wavelength with periodic boundary conditions was used. The floor was one wavelength long and divided into 8 segments. Floor depths between 2.5% and 15% of the wavelength were used.

Figure 6-10 shows a typical wave with a wave height of 2%, SPH particle size of 0.5% of the wavelength and a moving floor at a depth of 10% of the wavelength. Note that the shell elements of the moving floor extend beyond the domain of the SPH particles, as the floor nodes have orbits that traverse the fixed location of the periodic boundary that contain the SPH particles.

Figure 6-10. A fully developed wave developed by a moving floor.

6.3.2 Surface Profiles

The non-dimensionalised surface profile of the wave from Figure 6-10 is shown in Figure 6-11 for one instant. The surface profile is characterised by smooth regions and rough regions. The roughness is due to the particles packing irregularly on the surface at a region where the depth is not an integral number of particle diameters. Note that the step in the profile irregularity is less than one particle diameter, which in this case was 0.5% of a wavelength.

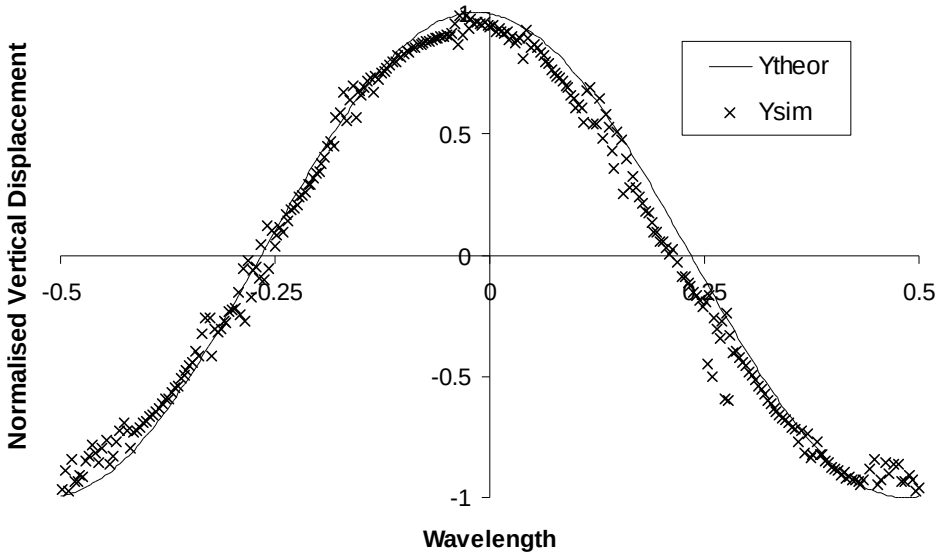

Figure 6-11. Normalised vertical surface profile of a wave developed with the floor at a depth of 10% of the wavelength, comparison of Airy theory to simulation results.

Figure 6-12 highlights the slightly irregular spacing of the SPH particles at the crest, which coincides with the roughness of the crest in Figure 6-11.

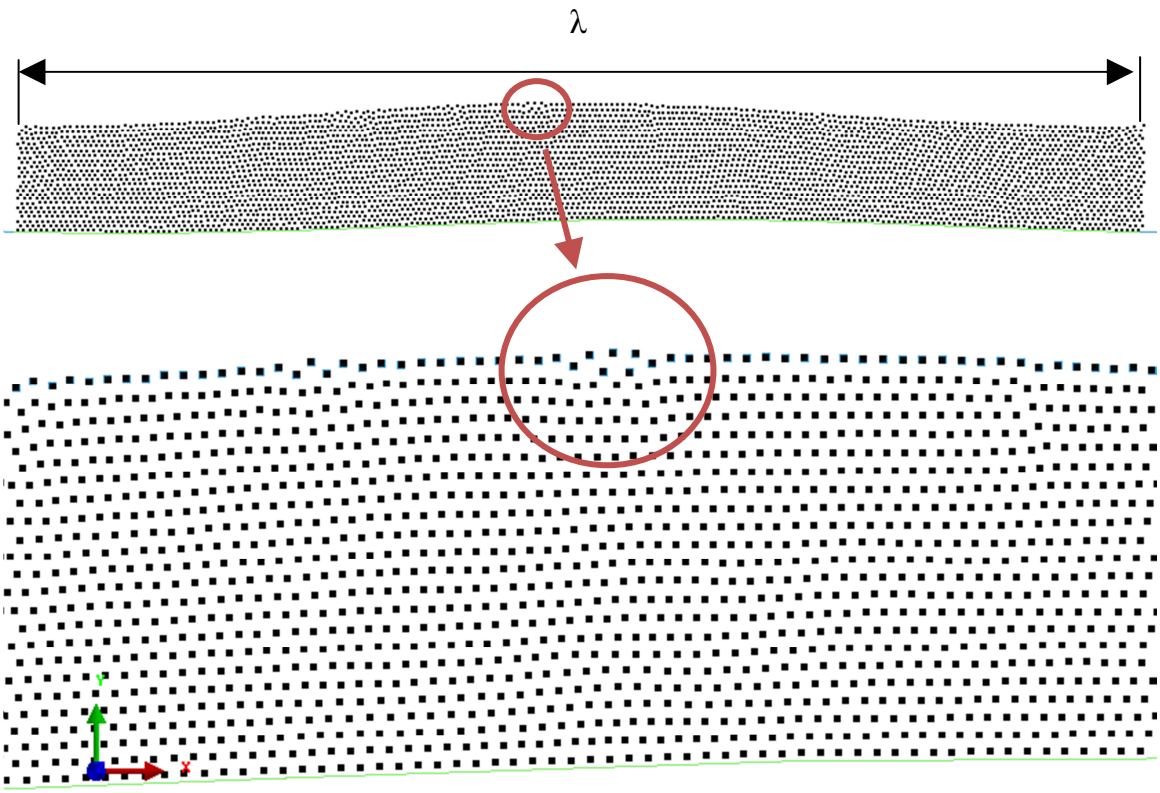

Figure 6-12. Surface roughness in the profile of the wave is due to irregular packing of the SPH particles as they accommodate a depth that is not an integral number of SPH diameters.

Figure 6-13 shows the surface profiles for each of the floor depths from 2.5% depth to 15% depth. Each profile has been normalized to its actual wave-height of 2% of wavelength. The profiles are very similar in shape for the floor depths studied. There is greater irregularity in the profile on the face of the wave (the waves are moving from right to left) than there is on the back of the wave. Waves with deeper floors tend to have a leading phase angle compared to the shallower waves, even though the phase of the floor was the same at the instant the data was recorded for each wave. This phase difference between the wave surface and the floor is evident in Figure 6-12 also, where the surface crest visibly leads the crest in the floor orbits.

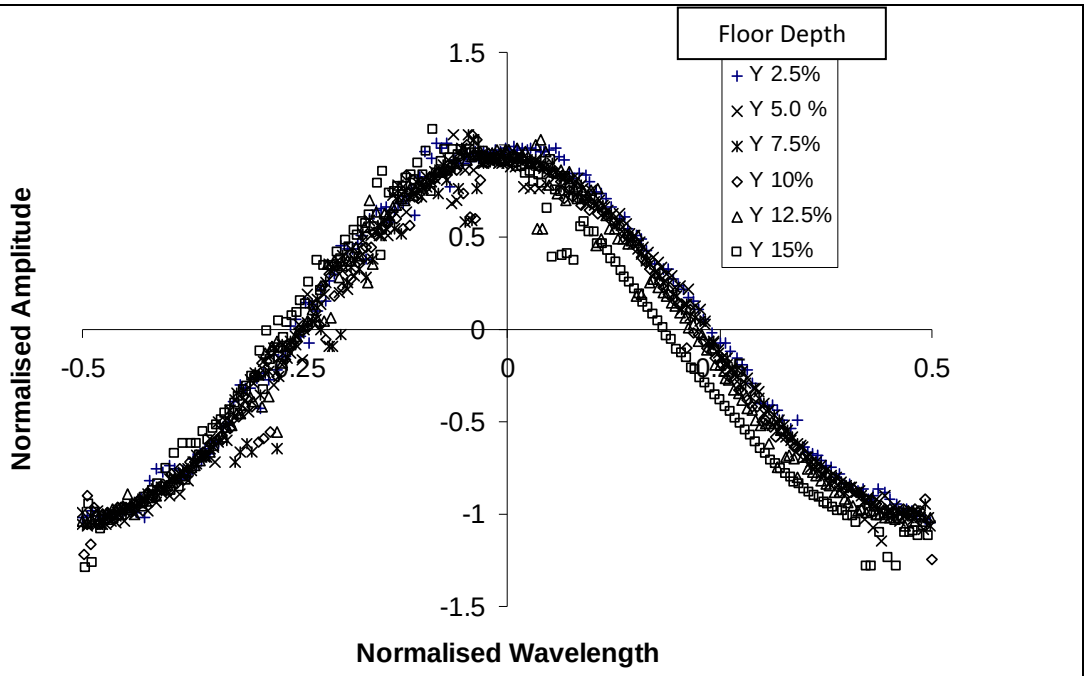

Figure 6-13. Surface profiles for each of the depths studied. Wave height was 2% of wavelength.

6.3.3 Through-Depth Velocity Profiles

Through-depth velocity profiles in the horizontal and vertical directions for the 10% depth wave are shown in the colour contours of Figure 6-14 and 6-15. The distribution of velocities is similar for the other depth floors, and does vary slightly with time. The distribution shown in these figures is typical.

Figure 6-14 reveals the maximum magnitude horizontal velocity is below the surface of the wave, which is not in agreement with the theoretical distribution. The vertical velocity profile of Figure 6-15 has the maximum magnitude velocity on the surface of the wave, which agrees with the theoretical distribution.

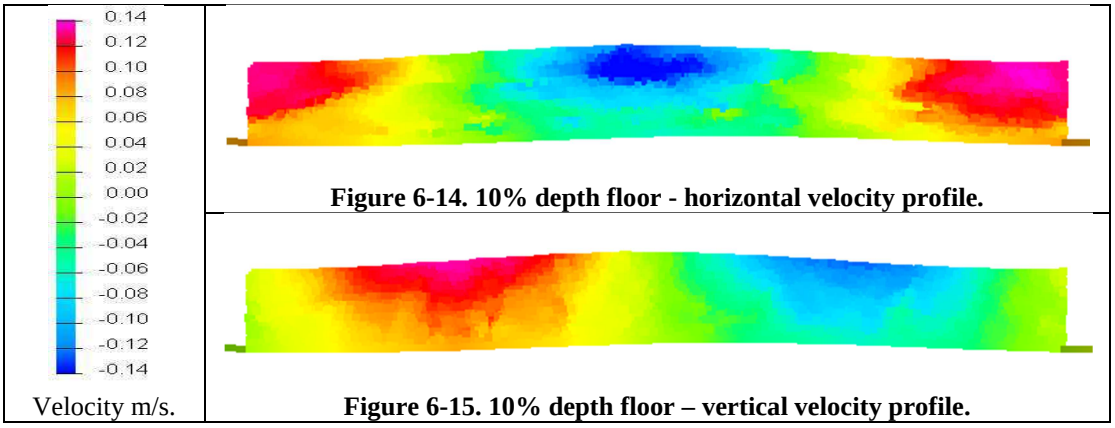

Figure 6-14. 10% depth floor - horizontal velocity profile.

Figure 6-15. 10% depth floor – vertical velocity profile.

A more comprehensive review of the velocities within the 10% depth wave is depicted in Figure 6-16 where the distribution of velocities with depth is shown for vertical and

horizontal directions. The velocity is normalised by the theoretical surface velocity for wave of interest, and the depth is normalised by wavelength. Figure 6-17 is the distribution for an Airy Wave of the same characteristics.

The horizontal distribution of velocity from simulation shown in Figure 6-16 has considerable deviation from the theoretical distribution of Figure 6-17. The vertical distribution of velocity in simulation deviates less from the theoretical than the horizontal distribution.

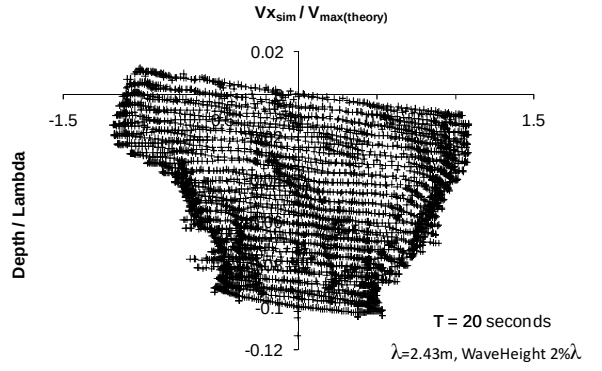

Normalised horizontal velocity as a function of normalised depth – SIMULATION.

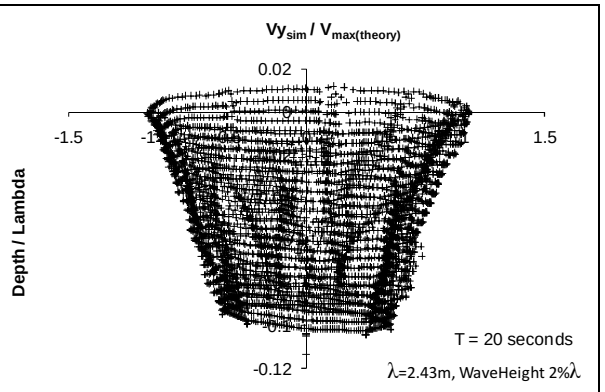

Normalised vertical velocity as a function of normalised depth – SIMULATION.

Figure 6-16. Normalised horizontal and vertical velocity of all SPH particles within a wave for the floor at 10%wavelength.

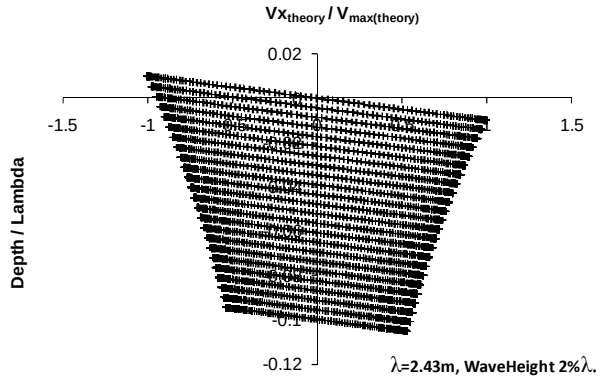

Normalised horizontal velocity as a function of normalized depth – AIRY WAVE THEORY.

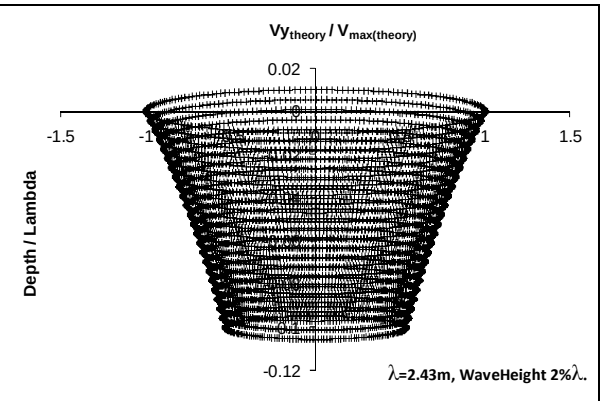

Normalised vertical velocity as a function of normalized depth – AIRY WAVE THEORY.

Figure 6-17. Normalised theoretical horizontal and vertical velocity within a wave for the floor at 10%wavelength.

The deviation in the horizontal velocity requires more investigation and so this has been studied in greater detail in Figures 6-18 through to 6-22.

The horizontal velocity of a single particle on the surface of the wave with floor at 10% wavelength is shown in Figure 6-18 . The theoretical maximum surface velocity is indicated by the dashed lines. The maximum particle velocity varies slightly around the theoretical value, in both positive and negative directions.

In Figure 6-18 there is a slight bias of the velocity curve in the negative direction, with an average of -0.004 m/s, or -3% of the maximum velocity. The result is a net movement with time of all of the SPH particles in the direction of the wave propagation, which could be interpreted as drift for the wave modeled here. This drift effect is highlighted in Figure 6-19 where the x coordinate of the same SPH particle is plotted with time. The mean position of this particle moves approximately linearly with time in the period between 10 and 20 seconds, indicating constant drift velocity. ie after the wave has become developed and stable. The use of "periodic boundary conditions", as used here, would allow this behaviour to be maintained for the duration of the simulation. Although not explored here, as it is not particularly relevant to ship motions, this 'drift-like' behaviour suggests that drift could be modeled with this approach also – in which case the floor motions would need to accommodate this effect (currently they do not, as the orbits are defined around a fixed reference that does not move with time.)

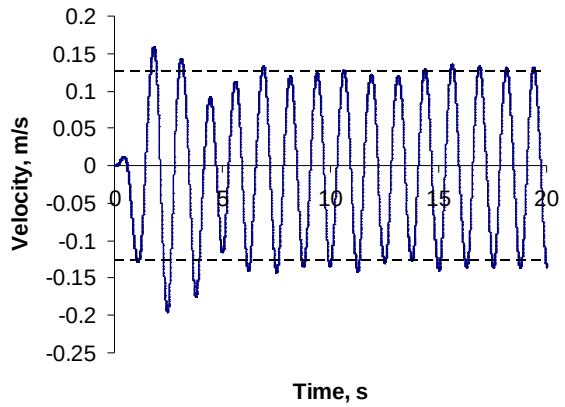

Figure 6-18. Horizontal velocity with time of a single SPH particle on the surface.

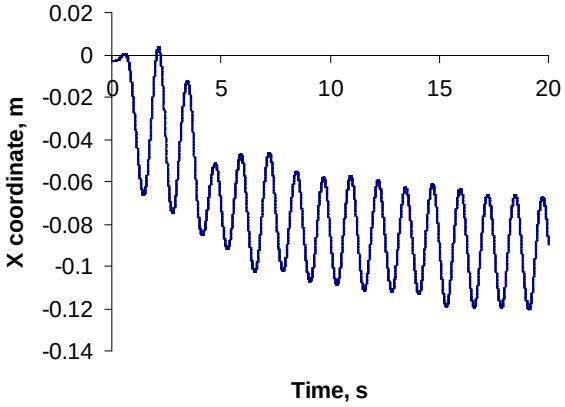

Figure 6-19. X coordinate with time of a surface particle, showing effective drift.

Figure 6-20 is a set of plots each showing the horizontal velocity at a single instant within waves at each of floor depths studied from 2.5% to 15% of wavelength. There is some scatter in the results as the values of individual SPH particles locations have been measured at one instant in time. Despite this scatter, and despite only a vertical selection of particles being used to generate the suite of curves in Figure 6-20, the correlation of the distribution at 10% depth shows strong similarity to the maximum values for the entire wave at 10% depth shown in Figure 6-16, giving confidence that these curves are a good representation of the distribution with floor depth at this wave condition.

In general the horizontal velocity has a maximum value at a depth of about 2-4% wavelength depth below the surface, with this maximum as high as 15% above the maximum surface velocity for one case observed. The velocities immediately above the floor are less than the theoretical values, but by a lesser amount.

It should be emphasised that these observations are for the conditions modelled. It may be possible to reduce these errors by increasing the number of moving floor segments per wavelength (8 was used here), and better understanding the required interface conditions between the floor and the water, such as the ‘cohesiveness’ between the floor and the water.

Figure 6-21 is a plot of the horizontal velocity as a function of depth down to the 15% wavelength depth for all the floor depths. Figure 6-22 is the same plot with the depth shown to a full wavelength of depth. Both plots indicate the level of scatter in the results, but also that the results generally follow the theoretical velocity with depth.

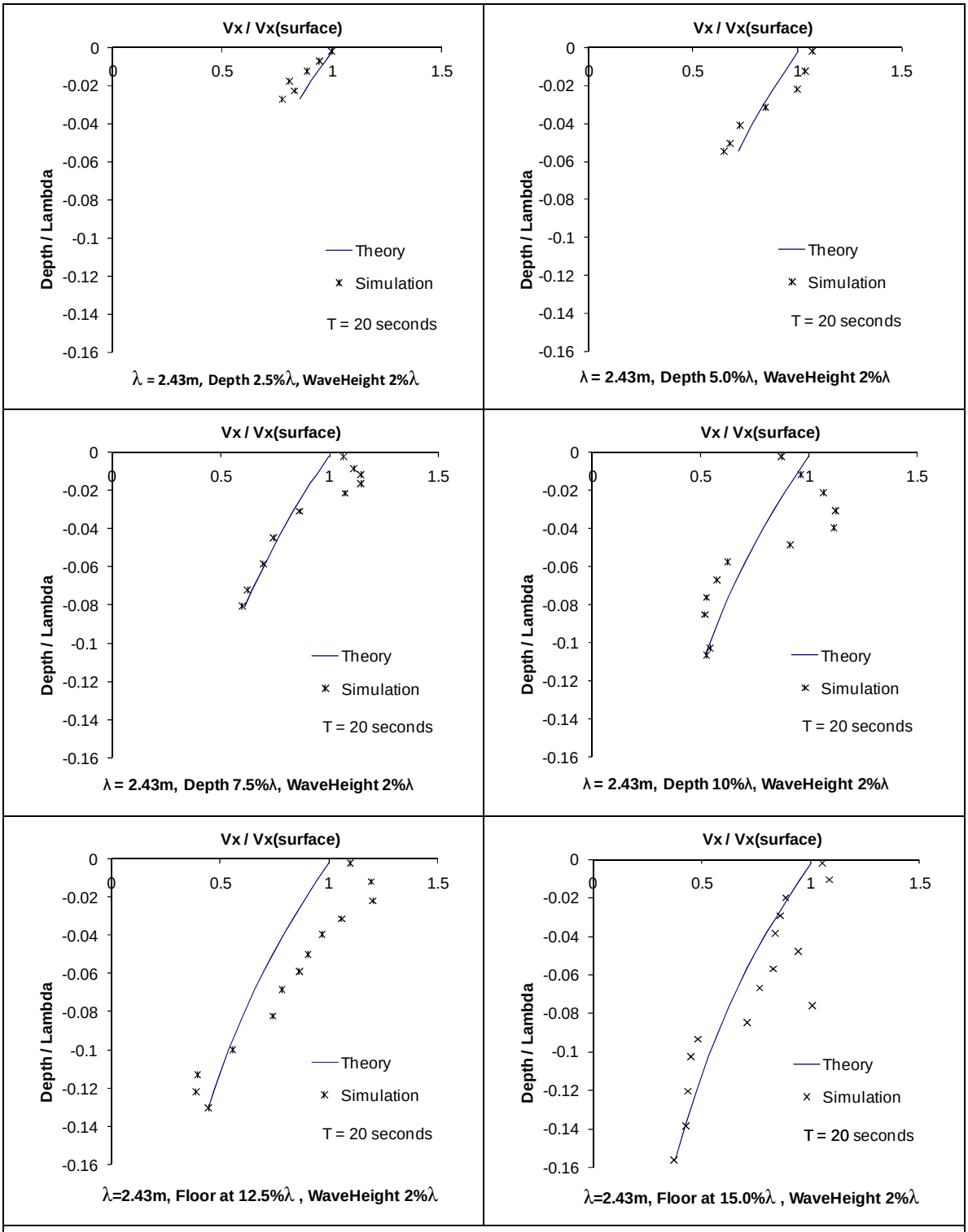

Figure 6-20. Normalised horizontal velocity as a function of depth for floors at a depth of 2.5 to 15% wavelength.

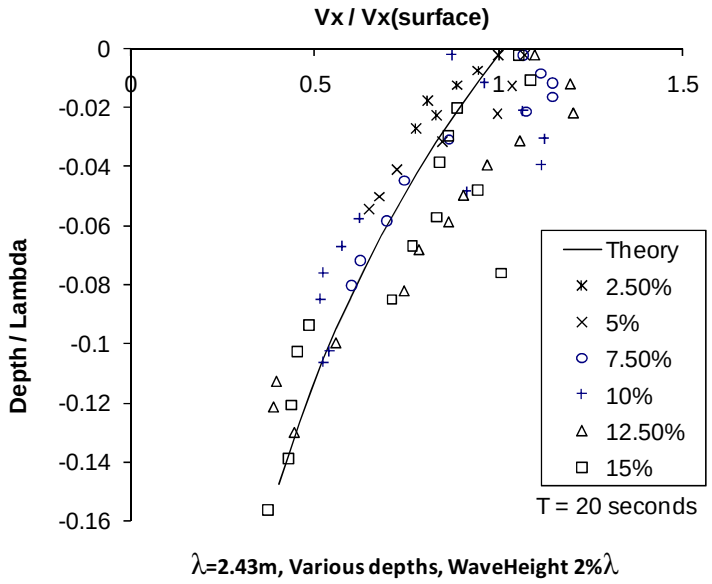

Figure 6-21. Summary of Normalised horizontal velocity for all floor depths studied.

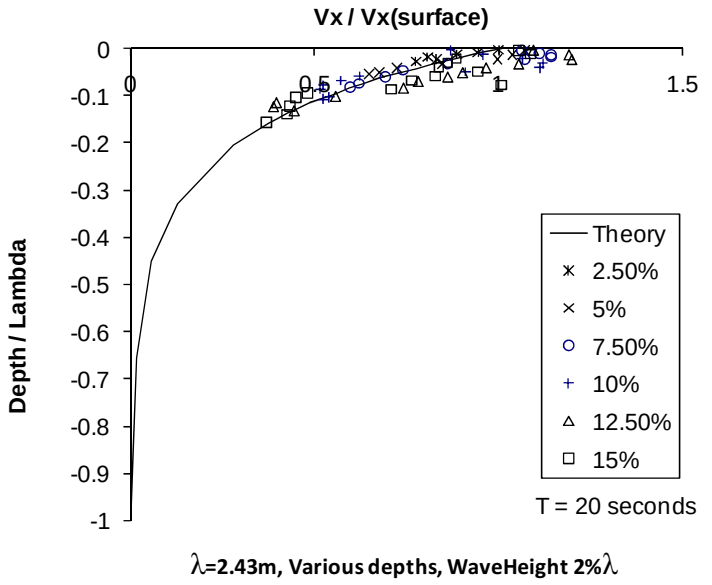

Figure 6-22. Summary of Normalised horizontal velocity for all floor depths studied, with the depth axis extended to one wavelength

6.3.4 Through-Depth Pressure Profiles

The theoretical pressure distribution through the depth is given by the Bernoulli equation as follows:

$$\frac{\upsilon^2}{2} + gz + \frac{p}{\rho} = \text{constant} \tag{29}$$

Rearranging (29) for pressure, p, the hydrostatic pressure and the dynamic pressure components are respectively:

$$p_z = \rho g z \tag{30}$$

$$p_\upsilon = \frac{\rho \upsilon^2}{2} \tag{31}$$

The normalised dynamic pressure is dependent on the local velocity of the water. It was shown in Section 6.3.3 that the velocity profile within the waves obtained using the moving floor technique deviates from the theoretical velocity profile.

Figure 6-23 is a plot of the dynamic pressure profile for the wave developed with the moving floor at a depth of 10% wavelength. The curve shows similarity to the velocity distribution as the dynamic pressure contains a velocity squared term.

Figure 6-23 was developed from the peak horizontal velocity profile. As the horizontal velocity profile is further from the theoretical than the vertical velocity profile, this dynamic pressure profile is likely to be representative of the worst case for the floor at this depth.

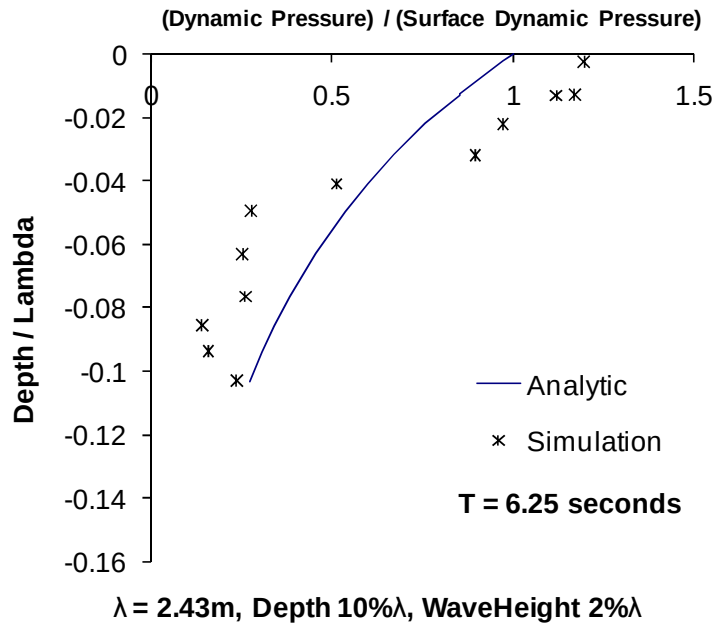

Figure 6-23. Normalised dynamic pressure with depth for the floor at 10% wavelength.

6.4 *Effect of Floor Depth*

The diameter of the orbits of the water motion decrease exponentially with depth. Typically there are no significant wave-to-sea-floor interactions when the water depth is greater than half a wavelength. If the floor is moving, then it was presumed that the depth would need to be less than one half a wavelength for the floor to influence the surface.

Simulations were performed with the moving floor at various depths to observe the effect on the surface waves generated. Periodic boundary conditions were used, with the SPH parameters of Table 6-1 used in all simulations. The floor depth was varied from 5% to 40%. Floor amplitudes were prescribed according to the orbit at each floor depth for an h/λ of 2%.

Figure 6-24 shows the normalised wave height as a function of floor depth. At shallow floor depths the wave height was very close to the theoretical wave height. The curve shows a distinct peak in surface wave height when the moving floor was at a depth of 22.5 % of wavelength. Beyond this depth the surface wave height diminishes rapidly.

The correct wave height at very shallow floor depths was expected, as the water was literally following the moving floor. The reduction in wave height for depths close to 50% wavelength was also expected due to the conditions for deep water waves and requirements for no tank floor interference.

The peak of Figure 6-24 at 22.5 % of floor depth was unexpected. It could be a resonant characteristic of the conditions chosen. The cause of this peak has not been investigated, but is important to notice its presence as an unusual and unexpected characteristic worthy of further exploration.

Figure 6-25 shows the phase angle between the surface wave and the moving floor for the various depths trialled. The zero datum is the crest of wave at the floor. At shallow floor depths the surface wave is ahead by 50 degrees, decreasing to about 35 degrees at 15% depth, and then increasing continuously up to 176 degrees at the maximum depth trialled of 40%.

The change in phase angle with depth implies a deviation in velocity vector of the orbits that may be part of the deviation seen in the horizontal and vertical velocity components in Section 6.3.3.

The leading phase angle between the surface and the floor is as though the driving mechanism for the wave generation is the floor effectively lifting a mass of water, and the water moving ahead of the oncoming crest in the floor. Hence the surface must always lead the floor by some amount, but not so much that it runs up the back of the next wave crest. It is plausible this lag has some response time and so is depth dependent. The maximum leading phase of 176 degrees is interesting in that the surface and floor are almost exactly out of phase, yet propagating in the same direction. This further suggests some resonant behaviour, either in the dimensions and frequency or the SPH conditions chosen here.

The nonlinear nature of the surface wave height as a function of floor depth suggests that a trial should be run to ensure the desired wave height is being generated.

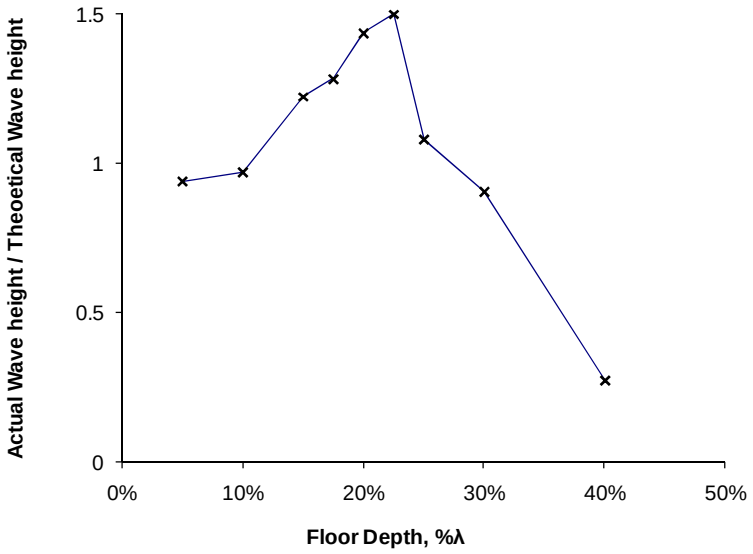

Figure 6-24. Normalised wave height as a function of floor depth.

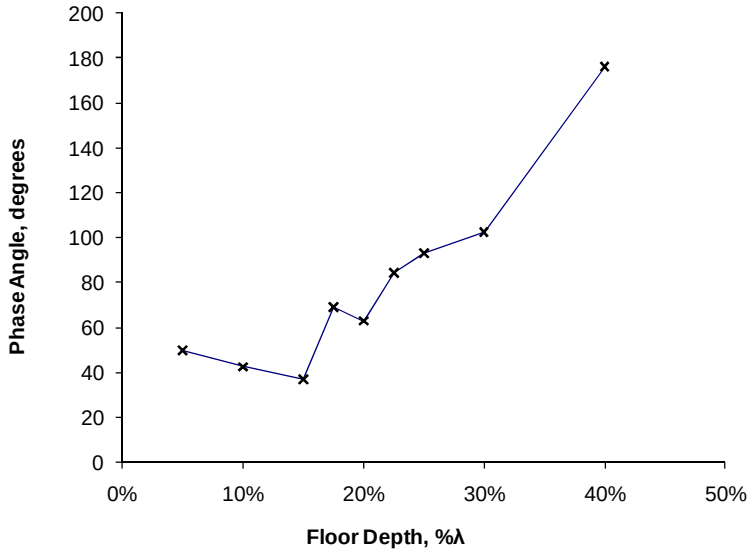

Figure 6-25. Phase angle between surface wave and moving floor.

6.5 *Summary of Regular Waves in a Mesh-Free Environment*

The software used here, when modelling a wave tank with a single paddle at one end produced a wave train in SPH particles that decayed too quickly for ship response predictions. The excessive decay was due to numerical damping that is inherent in the fundamental SPH algorithms to ensure a stable solution, i.e. without the damping the SPH would tend to fly apart and become 'unstable'.

A technique that generated a more uniform wave height for any length of wave tank has been developed. The technique uses floor segments that move according to the linear wave theory motion for the motions of water within a deep-water wave at that depth. The depth must be less than one–half a wavelength.

The waves developed simultaneously along the entire length of the tank, indicating that the surface waves are developed by energy transfer from the floor. Although the inherent dissipation losses with the SPH algorithm are still present, the wave energy is input along the entire length of the tank through the motions of the floor. The losses in energy transfer are then only through the depth of the tank. This is in contrast to the conventional paddle-type wave generator where the surface wave at any distance along the tank has had to propagate along the length of the tank from the wave-maker, and so lose energy due to the SPH interactions all along that path of propagation.

The surface profile of the wave generated with this moving floor technique is quite close to the sinusoidal driving function. Interestingly, and not shown here as it is not relevant to regular small amplitude ship motions, is that the surface wave can be made to grow beyond the linear conditions, to a quite steep profile, and even to breaking, merely by increasing the orbit diameter of the floor. There is a distinct relationship between the floor motions and the surface motions, such that non-linear surface waves can be generated through the use of non-linear floor functions (Groenenboom and Cartwright 2010).

The velocity profile through the depth of the wave is of the correct general form in both the horizontal and vertical directions, however significant deviations from the theoretical distribution are evident, more so in the horizontal than vertical direction. In general the horizontal velocity has a maximum value at a depth of about 2-4% wavelength depth below the surface, with this maximum as high as 15% above the maximum surface velocity for one case observed. The velocities immediately above the floor were observed to be up to 10% less than the theoretical values at this depth.

It is not known if the deviation from theoretical profiles of velocity and dynamic pressure are a result of the fundamentally different way the wave is generated in the present technique, or if the deviation is due to a less than ideal material behavior by means of the SPH parameters chosen.

A benefit of the moving floor technique is that the wave develops simultaneously along the length of the tank. For a very long tank this could represent a significant reduction in computational effort compared to a traditional wave tank where the wave must propagate along the entire length of the tank before the steady state condition is reached.

Another advantage of the moving floor technique is that no dispersion of the waves will develop along the tank, because the surface waves are generated by energy transferred from the floor through the depth. There may be small components of energy that travel in the direction of the wave propagation along the surface, but due to the (current) inherent losses within the SPH technique itself, these components will decay quite rapidly and not traverse more than a few wavelengths. Hence for a very long tank, it is possible with the moving floor to have the exact same waves represented at all positions along the tank.

7 Prediction of Ship Response in Regular Waves using SPH

The aim was to produce a subset of results that could be directly compared to a subset of the towing tank results for the AMECRC09 model hull from Macfarlane and Lees (1999).

The AMECRC09 hull was described in Chapter 4 Section 10. The principal dimensions of the physical model are summarised again here in Table 7-1 and Table 7-2.

Table 7-1 Particulars of the AMECRC09 hull and the FE Model.

Model	L/B	B/T	Cb	LCB %	LCF %	LWL (m)	Wetted Surface Area (m2)	Displacement (kg)
AMECRC09	8.00	2.5	0.5	-5.40	-8.75	1.6	0.3732	12.804
FE	8.00	2.5	0.5	-5.70	-8.80	1.6	0.3766	12.804

Table 7-2 Mass properties of the AMECRC09 hull and the FE Model.

Model	Radius of Gyration	Mass kg	Ixx $Kg.m^2$	Iyy $Kg.m^2$	Izz $Kg.m^2$
AMECRC09	0.4m	12.804	Not stated	2.048	2.048
FE Full-model	0.4 m	12.804	0.106	2.048	2.048
FE Half-model	0.4 m	6.402	0.053	1.024	1.024

The pitch and heave response at Froude numbers of 0.25 and 0.5, for a nominal wave height of 2.5% of L have been compared. The wave frequencies chosen for comparison were those around the characteristic features of the transfer function curves, namely non-dimensional wave frequencies expressed as $\omega/\sqrt{(L/g)}$, of 1.5 to 2.8.

7.1 *Reference Data*

The reference data was from Macfarlane and Lees (1999). Data was presented for towing tank experiments and linear strip theory predictions.

The experimental reference data was presented as pitch and heave transfer functions extrapolated to zero wave height, and non-dimensionalised pitch and heave as a function of wave height. For comparison to the results by SPH here, the response at actual wave height was used.

The linear strip theory predictions were produced by the Wolfson Unit Software Package of the time, circa 1999, hereafter called the linear strip theory results (Macfarlane and Lees 1999).

7.2 *SPH Simulation Setup*

The SPH simulations were conducted at model scale. The tank used for the SPH simulations was nominally 24m long, 3.55m wide and produced deep water waves.

The actual length of the tank varied with each wave frequency used because the method of wave generation required the length of the tank be an integral number of wavelengths. The width used was 1.75m wide with symmetry on the centreline of the vessel. An image of the simulation setup is shown in Figure A5-1.

A nominal SPH spacing of 0.04m was used for all cases. This gave an L/s (hull length to SPH spacing ratio) of 40, according to the rules developed in Chapter 5. The L/s of 40 produced smooth CG motions of the vessel at all conditions studied here, and so was considered further evidence of an adequate SPH spacing.

The model hull was a rigid finite element model as described in Chapter 4. The model was free to move in pitch and heave. Surge was restricted by the velocity boundary condition prescribed on the hull to attain the forward test speed. All other motions were fixed. Pitch and heave were measured at the centre of gravity. The centre of gravity was located at the same location on the FE model as on the physical model, producing a level trim at zero forward speed for both the FE model and the physical model.

Mass and inertia were assigned to the rigid body finite elements of the hull. Rotational inertia was confirmed in the finite element environment by conducting a bifilar suspension numerical simulation, as described in Appendix A1.

At the start of each run four processes were initialised. These were:

1) settling of the water particles from their initially orthogonal arrangement into a three-dimensional hexagonally packed arrangement;
2) development of surface waves;
3) settling of the vessel onto the water surface; and
4) acceleration of the vessel to the desired forward speed.

The first three processes commenced simultaneously from the start of the simulation. The acceleration of the vessel commenced after 2.5 seconds (at model scale) to ensure the vessel was reasonably stable in the water prior to being accelerated.

At the start of the simulation the water particles inherently re-arranged themselves into the three-dimensional hexagonal arrangement due to the gravitational acceleration acting on them. (From a practical perspective, a mathematically perfect orthogonal distribution of water particles has been observed to remain that way even with gravity acting on them until disturbed somehow. In the case here the disturbing influence comes from the moving floor to create the waves, and the impact of the vessel onto the surface.)

The orbital motions of the floor elements to generate the surface waves were developed from stationary to full amplitude over one wave period. The surface waves were typically fully developed after a further period. After two wave periods from the start of the simulation the surface waves were developed over the entire length of the tank.

The vessel commenced the simulation just above the water surface, and "fell" into the water due to the action of gravity acting on its centre of gravity at the start of the simulation. A balance of buoyancy and displacement was typically acquired in about one second at model scale, displaying some oscillation in the process. The process of dropping the hull into the water was a numerical modelling shortcut to obviate the need to create a hole in the water for the vessel to sit in, and consequently avoided the more painful checks to ensure no water was within the hull.

The vessel was allowed to "settle" onto the (moving) water surface for 2.5 seconds before being accelerated to the test speed over a further 2.5 seconds. The forward motion was controlled by a velocity boundary condition function that prescribed the velocity applied to the centre of gravity. For this setup, forward speed of the vessel was constant and no change in forward speed was allowed due to wave conditions.

A typical vertical motion of the CG of the model hull for a complete simulation is shown in Figure 7-1 for example. The response due to the above-mentioned processes can be seen in the first 5 seconds. From 5 to about 10 seconds the vessel was achieving a dynamic equilibrium in the waves. The vessel response was then calculated from the latter half of the simulation.

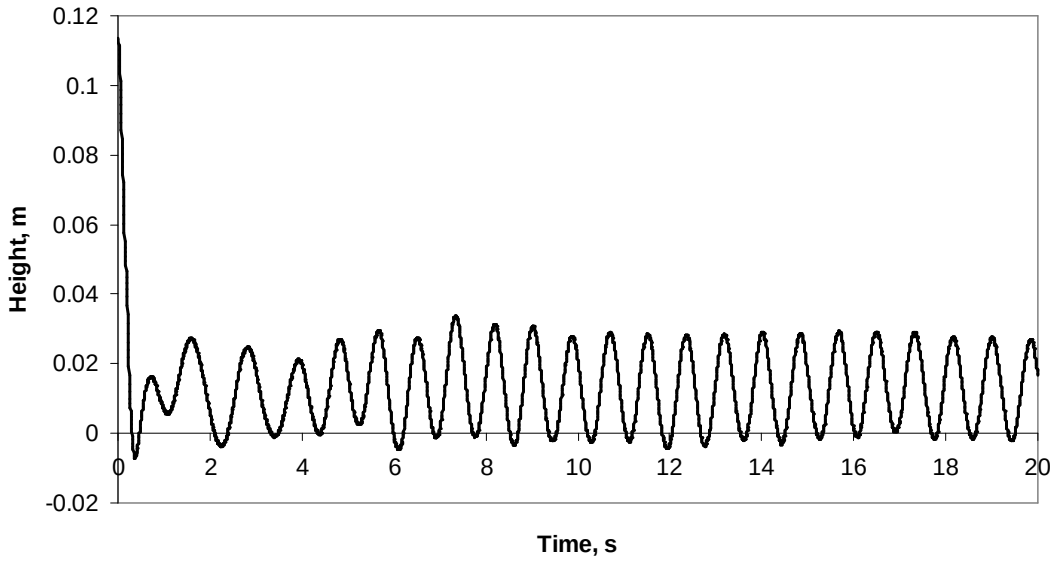

Figure 7-1. Vertical motion of the CG over the entire simulation time. Dropping of the vessel into the water occurred in the first ½ second, followed by the acquiring of steady state conditions, in this case for a wave of 0.8 Hz, nominal wave height of 40mm and U = 0.99m/s.

7.3 *Tank Width, Tank Depth and Contact Thickness Effects*

7.3.1 Tank Width Effects

Preliminary SPH simulations of the AMECRC09 hull were conducted at Fr 0.25 across the frequency range of interest in a towing tank that was 1.5m deep and 1.33m wide.

The depth of the numerical tank was necessarily less than the towing tank to enable wave generation by the moving floor method. The width of the numerical tank was chosen to be much less than the width of the towing tank purely to reduce the number of SPH particles, and so reduce the computational effort for each run.

The pitch and heave transfer functions derived from the preliminary SPH simulation results showed unusual peaks at low frequencies that were not present in the reference data.

This unexpected result led to a brief investigation into the influence of the width of the towing tank on the results, namely tank wall interference.

Tank wall interference occurs when the waves generated by the vessel moving forward are reflected from the side walls of the towing tank, and interact with the vessel or its waves, thus influencing the response of the vessel (Bhattacharya, 1972). The conditions under which tank wall interference occurs are dependent on ratios of ship length to tank width, wave length to ship length, and vessel speed to length.

Lloyd (1998) provides guidelines for avoiding tank wall interference by defining a critical Froude number below which tank wall interference will occur for given test conditions. The guidelines merely state interference will occur at the conditions, it does not state the severity of the interference.

Applying the guidelines of Lloyd (1998) to the preliminary SPH simulation and the towing tank test conditions, the Froude number below which tank wall interference will occur can be calculated.

Figure 7-2 is a plot of Froude number versus non-dimensional wave frequency below which tank wall interference will occur. Two L/B ratios are shown, where B here is the breadth of the tank. The dotted curve is for the test hull in the 1.33m wide tank, L/B of 0.45, and the solid curve is for the test hull in the 3.55m wide towing tank, L/B of 1.2. The curves were developed for the range of frequencies of interest in this study. Non-dimensional wave frequency is defined as $\omega/\sqrt{(L/g)}$, ω in rad/sec.

The curves of Figure 7-2 show that all the tests at Fr 0.25 for the L/B of 0.45 are likely to have tank wall interference. The curve for L/B of 1.2 will experience tank wall interference only above a non-dimensional frequency of 3.

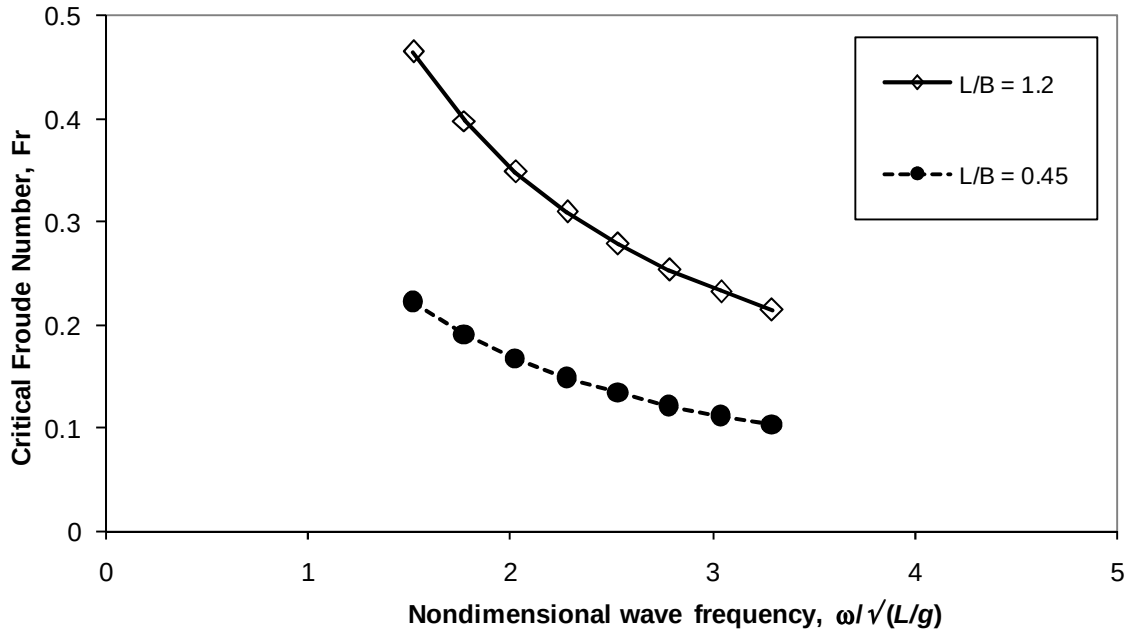

Figure 7-2. Critical Froude Number below which Tank Wall Interference will occur.

From this it was deemed possible that the irregular results in the preliminary SPH simulations in the narrow tank were due to the real physical effect of tank wall interference. To eliminate this possibility, and to be as representative as possible to the reference conditions, all further SPH simulations were conducted in a numerical tank with a ship length L, to tank breadth B, of (L/B) equal to a value of 1.2

7.3.2 Tank Depth Effects

The longest wavelength that can be used in a physical towing tank is typically twice the depth of the towing tank, such that bottom interference does not occur. Bottom interference will change the shape of the wave and hence the assumptions about linearity of the waves existing in the wave tank. The waves used for the experimental work as the reference for this research were of a wavelength less than twice the depth of the tank, and hence were deep water waves.

For the moving floor to generate waves, the tank floor must be at a depth of less than half a wave length, because the wave is generated by interaction of the water and the floor. Hence the floor of the tank for simulation was deliberately placed at a shallower location than for the physical tow tank.

In the case of higher frequency waves, the depth to generate the waves by floor excitation becomes quite shallow compared to the depth of the physical towing tank.

For these higher frequency waves requiring a shallow tank for generation by the moving floor, blockage effects may occur, even though the waves experienced by the vessel are ‘deep water’ waves.

Blockage effects occur when the cross sectional area of the vessel is large enough compared to the cross sectional area of the tank that the local fluid velocities around the vessel are altered significantly. As the blockage effect increases, the velocity of the water around the vessel becomes higher than the vessel speed over the bottom, and so this effect will influence the measured response.

The blockage factor on area for the AMC tank and the SPH tank are shown in Table 7-3. The blockage factor for the SPH simulations was 7.5 times higher than for the AMC tank because the SPH simulations employed a shallower depth tank for the unique wave generation method. This reduced depth may contribute to a depth related blockage factor.

Table 7-3 Blockage Factor based on area for the AMC tank and the SPH simulations.

Tank Name	Breadth m	Depth m	Tank Area m^2	Vessel XSA m^2	Blockage Factor
AMC Tank	3.55	1.5	5.25	0.0125	0.002
SPH Wide Shallow	3.55	.24	0.84	0.0125	0.015

Blockage effects have not been accounted for in the results presented here.

7.3.3 Contact Thickness Effects

In Chapter 4 the "contact thickness" was introduced as a numerical parameter that defines the minimum distance between the SPH particles and the shell elements of the hull of the vessel. It was shown that the hydrostatics of the vessel are sensitive to the correct value of this contact thickness parameter. A guideline was developed that stated that the correct hydrostatic response was developed when the contact thickness was 0.55 times the orthogonal SPH centre to distance.

The hydrostatic response of the vessel is a balance of the distribution of buoyancy and mass of the hull. Changing the contact thickness will change the distribution of buoyancy, and consequently the hydrostatics, as shown in Chapter 4.

The hydrodynamic response of the vessel is influenced by the inertial properties of the hull and waves, in addition to the distribution of the buoyancy and mass. A few trials were conducted to assess the sensitivity of the heave and pitch response to contact thickness variation: the pitch and heave response of the hull at a non-dimensional frequency of 2.44 (model scale of 0.6 Hz) and zero forward speed was predicted using the SPH technique.

Table 7.4 lists the change in static trim, the location of the centre of flotation and the centre of buoyancy, and the pitch and heave transfers functions for two contact thicknesses at one wave frequency. The contact thickness values were taken either side of the suggested 'correct' value developed in Chapter 4.

From the values in Table 7-4 it is noted that the LCB and LCF move at different rates, and so an angle of trim by the bow develops as contact thickness increases. The pitch and heave

transfers functions both decrease with increasing contact thickness, which is as expected as the vessel appears larger to the water with a larger contact thickness, particularly a fuller aft section for the shape of the hull presented here.

Table 7-4 Effect of Contact thickness on hydrostatic and hydrodynamic response.

Non-dimensional contact thickness (contact thickness / SPH spacing)	Static Trim of Vessel	LCB % LWL	LCF %LWL	Pitch Transfer Function F = 0.6Hz	Heave transfer Function F = 0.6Hz
0.5	0 degree	55.68 %	58.81 %	0.86	0.86
0.7	0.3 degree	55.50 %	59.51 %	0.79	0.81

The results calculated here indicate that the dynamic response was sensitive to the contact thickness for the conditions used. Ensuring the correct contact thickness through confirmation of the hydrostatics should then ensure that as accurate as possible dynamic response is predicted in SPH.

7.4 *Pitch and Heave at Froude Numbers of 0.25 and 0.5*

The SPH simulation used a tank depth of 0.24m across all wave frequencies. This represented a depth to wavelength range of about 9% to 30% of the wavelength. The shallow depth ensured good deep water wave representation by the moving floor technique as discussed in Chapter 6.

Figure 7-3 is a plot of the non-dimensional pitch transfer function as a function of non-dimensional wave frequency for a Fr of 0.25. The results obtained experimentally, those obtained using SPH and those obtained using linear strip theory are shown. In this figure it can be seen that the linear strip theory underestimates the towing tank results by 10-20%. The results from the SPH simulations underestimate the towing tank results by about 20% at the lower frequencies, increasing to as much as 50% at a non-dimensional wave frequency of 2.5, where the towing tank values were themselves quite low in magnitude.

Figure 7-4 is a plot of the non-dimensional heave transfer function as a function of non-dimensional wave frequency for a Fr of 0.25. The results obtained experimentally, those obtained using SPH and those obtained using linear strip theory are shown. The SPH simulation results are within the variability shown by the test tank results (error bars were not available in the reference data).

Figure 7-5 is a plot of the non-dimensional pitch transfer function as a function of non-dimensional wave frequency for a Fr of 0.5. The results obtained experimentally, those obtained using SPH and those obtained using linear strip theory are shown. This figure shows that the linear strip theory underestimates the towing tank results by 10-20%, at frequencies lower than the resonant peak, about 25% at the peak, and then are closer to the test results at the higher frequencies. The results from the SPH simulations are very similar to the linear strip theory results, with some scatter above and below the linear strip theory results across the frequency range.

Figure 7-6 is a plot of the non-dimensional heave transfer function as a function of non-dimensional wave frequency for a Fr of 0.5. The results obtained experimentally, those obtained using SPH and those obtained using linear strip theory are shown. The linear strip theory correlates with the towing tank results quite well across the frequency range. The SPH simulation results indicate the generic trend of the towing tank results, with good correlation at the high and low frequencies, but under-estimate the peak in the response by about 40%.

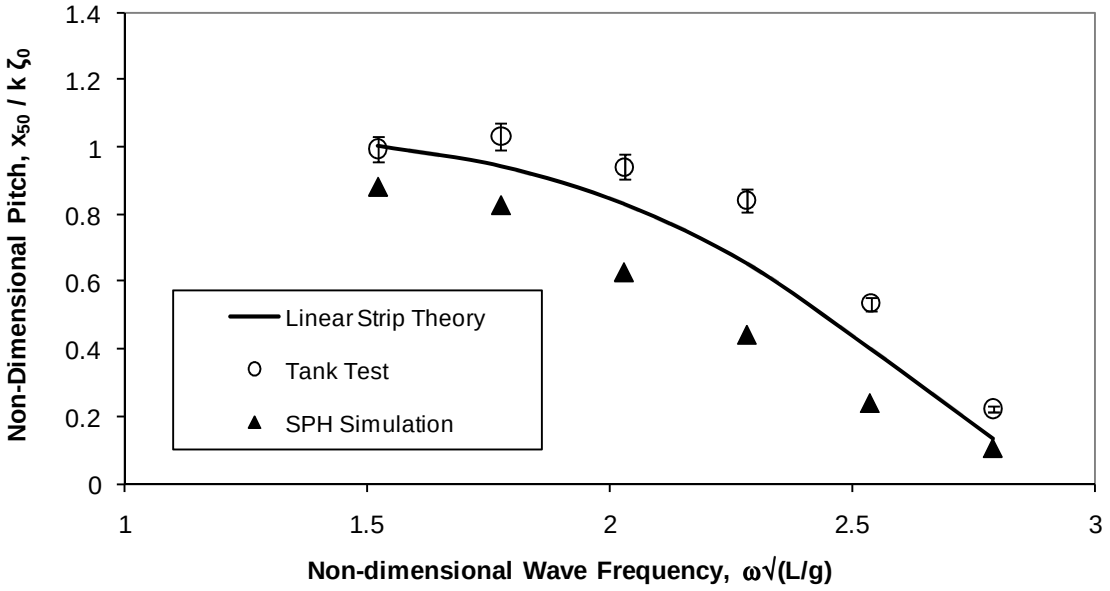

Figure 7-3. Pitch Transfer Function for Fr = 0.25.

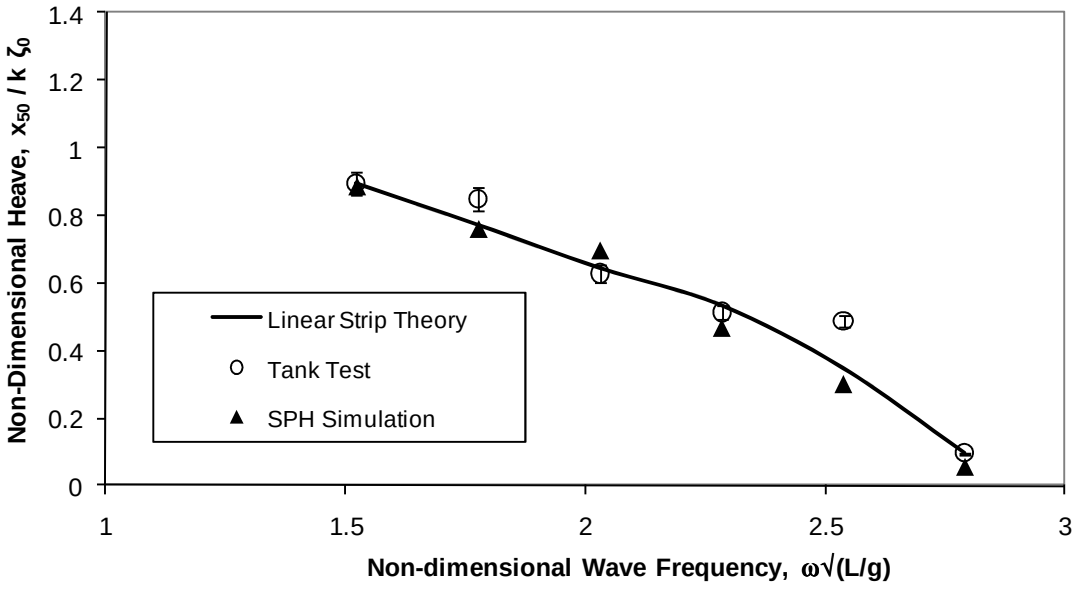

Figure 7-4. Heave Transfer Function for Fr = 0.25.

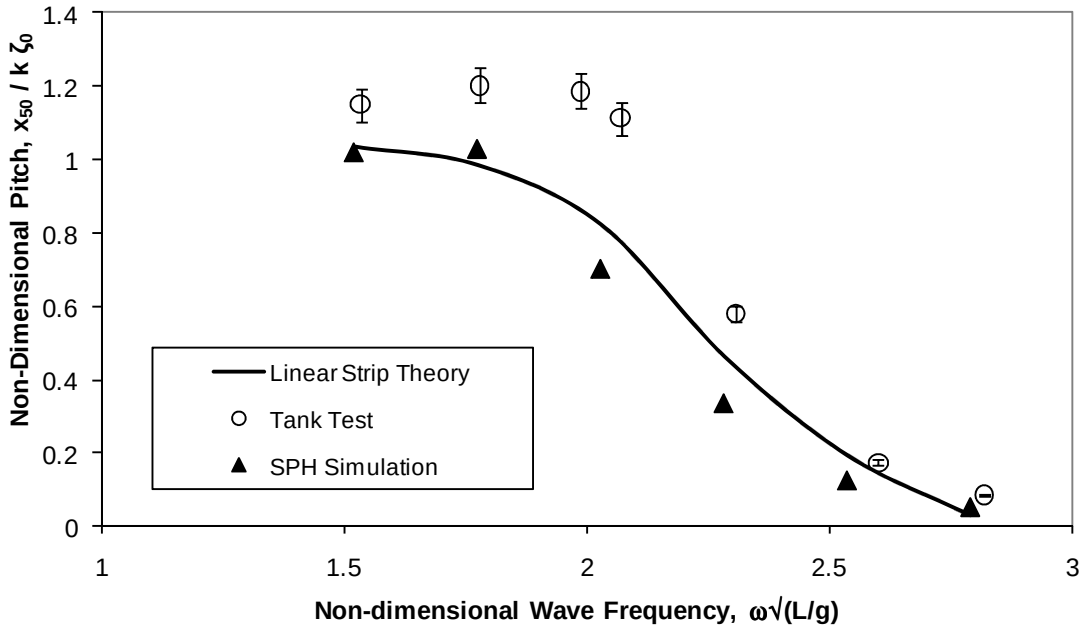

Figure 7-5. Pitch Transfer Function for Fr = 0.5.

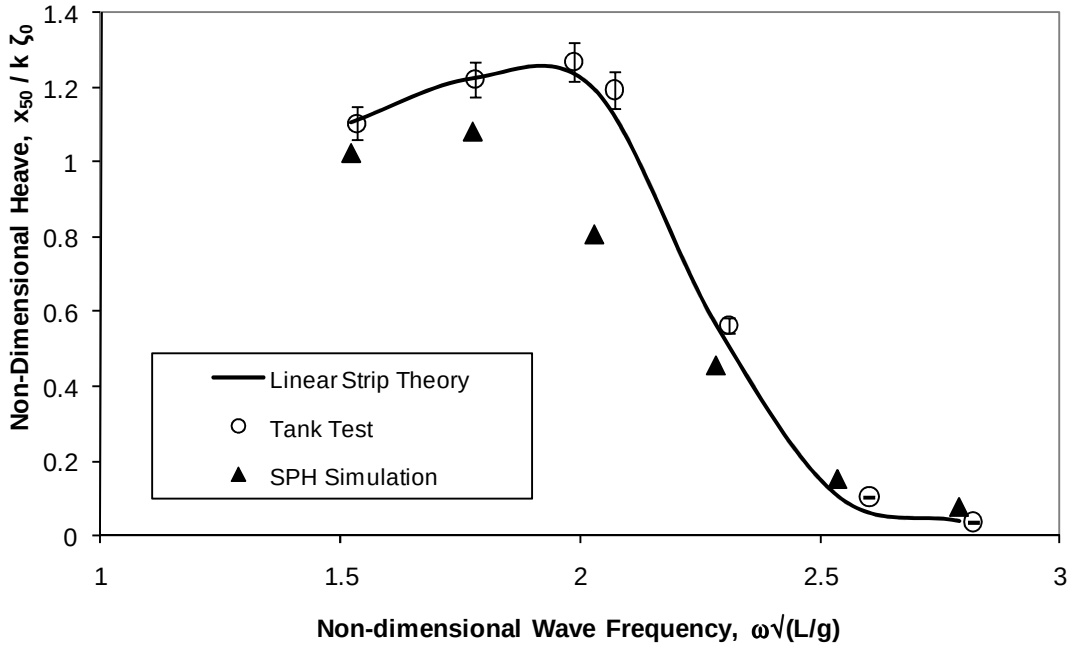

Figure 7-6. Heave Transfer Function for Fr = 0.5.

7.5 *Discussion of Ship Motion Predictions using SPH*

The transfer functions of pitch and heave for the conditions shown here follow the trends shown in both the towing tank results and the predictions using linear strip theory. The results obtained using SPH are typically about 10% lower than the experimental results, but by as much as 40-50% when the experimental results show peaks or are of small magnitude.

As both the pitch and heave results were lower when predicted using SPH than those measured in the experiment, one explanation is may be that the response obtained using SPH is over-damped in the simulations conducted here.

The dynamic results of the settling of the vessel into a hydrostatic equilibrium in Chapter 4, indicated that when the fluid is represented by a greater number of smaller SPH particles there is less damping compared to the use of fewer but larger SPH particles. A brief study in the currently affordable SPH particle size for the computing power available is therefore recommended for future work.

That the SPH technique did not reveal the sharp peaks in the heave transfer function at Fr = 0.5 is quite surprising considering that the SPH technique is more commonly used for analysis of short duration transient events (Kohlgruber et al 2003, Toso 2009, Vignejvic and Campbell 2009 a and b), rather than analysis of long duration quasi-static scenarios. This further suggests the SPH parameters have scope for tuning to reduce their inherent damping characteristics.

It is also possible that the velocity distribution in the waves is influencing the resultant ship motions. Section 6.4 revealed a phase difference between the surface and the floor, and a consequent velocity phase difference would also exist.

A brief comment is required on ship-generated waves. Wake and waves were radiated from the model hull in the SPH environment, as shown in the images of Figure A5-2 of Appendix A5. The experimental data of Macfarlane and Lees (1999) did not include wake measurements, so no correlation was possible. However, it is likely that the same dissipative forces observed in the waves discussed in Section 6.1 will be affecting these ship-generated waves also. It is therefore possible that the excessive dissipation of the wake and waves from the vessel will be influencing the response of the vessel, and hence this may also be contributing to errors observed in the predicted ship response.

8 Conclusion

This research work investigated the use of the mesh-free Smoothed Particle Hydrodynamics (SPH) technique to numerically simulate the response of a ship in regular waves. For this application the ship was defined by shell elements and the water defined by SPH particles.

Guidelines were developed to assist in selecting an SPH particle size and the contact thickness to obtain the correct buoyancy force for an object submerged. These guidelines were also used to locate the free surface. Numerically locating the free surface is useful for studies of hydrostatics and potentially for studies of damaged ships.

Regular waves produced in SPH particles using a paddle-type wave maker diminished in wave height to the point of being unusable for ship motion studies. The loss in wave height was most likely the effect reported by other researchers, as being due to the inherent numerical damping required to maintain a stable solution in the fundamental SPH algorithms.

A novel wave making technique was developed by the author that produced waves simultaneously and uniformly along the length of the tank. The technique, dubbed the moving floor technique, moves rigid floor segments of a shallow tank in accordance with the motions at that depth from linear wave theory. This wave making technique does not overcome the dissipative losses of the SPH algorithms, but instead reduces the path length over which these losses occur. This is the result of driving the surface by the motions of the floor, implying the SPH losses occur primarily through the depth of the tank instead of along the complete path of surface wave propagation.

Velocity and dynamic pressure profiles through the depth of the wave were compared to theoretical profiles. The values from simulation show the generic form of the theoretical profiles, but vary by up to 50% of the theoretical value at isolated points where they were measured within the wave. The phase of the surface elevations was observed to lead the floor elevations. This may contribute to the variation in velocities observed. Possible causes for the these deviations from the theoretical distributions are most likely due to the fundamentally different way the waves are developed.

The heave and pitch transfer functions developed for a high speed monohull displacement hull at Fr 0.25 and Fr 0.5 from motion predictions using SPH were generally lower than the transfer functions obtained from experiment. The predictions using SPH showed the presence of peaks in the responses but did not reveal them as clearly as in the experimental work and linear strip theory predictions.

The correlation between the numerical simulation using SPH and the experimental results needs to be improved before the SPH technique can be relied on as an industrial tool. The existing benefit of the technique to cater for any shape craft may lend itself to use where conventional tools will not work.

The outcomes of this research demonstrate that predicting ship motions using SPH is practical, but some refinement is required before producing accurate results. It is hoped this work will be continued to benefit from the SPH technique coupled with a structural solver.

9 Future Work

The work reported here has demonstrated that prediction of ship motions by the SPH technique is possible. However, the technique is not fully developed for industrial use, and hence is by no means complete. Numerous areas where further work is needed are readily apparent. A few suggestions are made here.

The reasons for under-prediction of the transfer functions obtained using SPH compared to those obtained from experiment needs to be understood and improved upon. Two likely reasons for the under-prediction are:

a) damping of the ship motions due to excessive "apparent" viscosity in the fluid; and

b) the velocity profile through the depth of the wave being different in a wave generated by the moving floor technique to that of a deep water wave.

Reduced damping of the ship motions may be achieved through tuning the existing SPH parameters, or it may be achieved through the implementation of new algorithms. As SPH methods are under continued development it is possible that new algorithms may be more effective in removing the numerical damping that is currently revealing itself as excessive viscosity (hence "apparent" viscosity) of the fluid.

The second item is related to the physics of wave generation. A more thorough understanding of the wave generation mechanism is required. It may be found that the variations in velocity and phase angle through the depth are unavoidable in a wave driven by floor motions. In this case, a decision as to if the deviations are acceptable needs to be made.

If acceptable ship motion correlation is achieved between the SPH technique and towing tank experiments, then confidence in the technique will be lifted and a vast array of opportunity should open up. The following are a few suggestions.

The predicted response of ships not restricted in surge. This applies to vessels in head seas, and in following seas. Both could be performed with a constant propulsive force on the vessel, and the forward speed would consequently be influenced by gravitational forces, surfing, and slamming. Non-linear limit-state conditions of ship survivability scenarios could be developed.

Development of the wave generation technique for wave spectra. As explained in Chapter 6 there will be limits on the frequency range possible based on the depth of the moving floor. However a useful wave spectrum may still be able to be developed by the laws of superposition through multi-frequency floor movements. This may then be taken further by developing waves in multiple directions.

The prediction of the roll response of ships, and those with internal roll-minimising systems such as resonant tanks could also be developed further using the SPH techniques described here and those developed by Kouh et al (2009).

Combing both the roll response of ships with a ship travelling broadside to a wave train may enable a predictive capability for broaching to be developed.

Exploiting the structural solver within the existing software lends itself to exploring structural responses of ships in waves, such as hydroelastic responses of slamming and whipping.

Predicting the response of a damaged ship may also be worthwhile. This could entail predicting the response of a disabled ship at an awkward orientation to the waves, or could include the effects of flooding through a breached hull. Flooding combines the effects of free surface flows and hydrostatics, both of which have been demonstrated competently here using SPH. The structural solver aspect of the software could then be used to predict the strains in the ship as a consequence of flooding in addition to the strains as a consequence of motions induced by waves.

It is hoped these ideas ignite some enthusiasm for further development of mesh-free methods for ship motion predictions.

10 References

Abdolmaleki, K., 2007, *"Modelling of wave impact on offshore structures."*, PhD Thesis, The University of Western Australia.

Autodesk Maya 3D, 2011, http://usa.autodesk.com/maya/ (available at May 2011).

Bass, D., Molyneux, D., and McTaggart, K., 2004, *"Simulating Wave Action in the Well Deck of Landing Platform Dock Ships using Computational Fluid Dynamics."*, WARSHIP 2004:Littoral Warfare & the Expeditionary Force, London, UK.

Bhattacharyya, R., Edited McCormack M. E., 1972 (1978 edition), "*Dynamics of Marine Vehicles*", Wiley.

Bojovic, P., 1995, "*AMECRC Systematic Series Calm Water Testing Results*", Australian Maritime Engineering Cooperative Research Centre, Report AMECRC IR 95/5.

Bourago, N.G., Kukudzhanov, V.,N., 2005, *"A review of contact algorithms"*, RAN. MTT No.1, pp 45-87, Institute for Problems in Mechanics, Russian Academy of Sciences, Moscow.

Cartwright, B., Groenenboom, P., and McGuckin, D., 2004a, *"Examples of Ship Motions and Wash Predictions by Smoothed Particle Hydrodynamics"*, PRADS 2004 Conference, 9th International Symposium of Practical Design of Ships and Other Floating Structures, http://www.prads2004.de/pdf/227.pdf, Germany.

Cartwright, B., Xia, J., Cannon, S., McGuckin, D., Groenenboom, P., 2006b, *"Motion Prediction of Ships and Yachts by Smoothed Particle Hydrodynamics"*, 2nd High Performance Yacht Design Conference, Auckland, NZ .

Cartwright, B., Groenenboom, P., McGuckin, D., 2004b, *"A novel technique to predict non-steady loads in vessels in severe seas."*, (Presentation only at the) ISOPE Conference, Toulon, France.

Cartwright, B., McGuckin, D., Turner, T., Cannon, S. 2006a. *"The modelling of landing craft motions inside a flooded Well dock using smoothed particle hydrodynamics."*, Proc. PACIFIC 2006 International Maritime Conference, Sydney, Australia.

Cartwright, B., Renilson, M., Macfarlane, G., McGuckin, G., Cannon, S., 2007. *"Motions of a landing craft in a flooded well dock - effect of well dock design"*, Proc. RINA Conf. Military Support Ships, London.

Crespo, A.J.C., Gómez-Gesteira, M., Dalrymple, R.A., 2007, *"SPH2D simulation: Validation and accuracy to experiments using different code compiling options."*, Proceedings of the SPHERIC 2nd International Workshop, Madrid, Spain.

Crespo, A.J.C., Gómez-Gesteira, M., Dalrymple, R.A., 2008, *"Modelling dam break behavior over a wet bed by a SPH technique."*, Journal of Waterway, Port, Coastal, and Ocean Engineering, Vol 134, No. 6, pp 313–320.

De Padova, D., Dalrymple, R.A., Mossa, M., Petrillo, A.F., 2009, "*SPH Simulations of Regular and Irregular Waves and their Comparison with Experimental Data*", http://arxiv.org/abs/0911.1872, downloaded November 2009 and October 2010.

Gingold, R. A., and Monaghan, J. J. 1977, *"Smoothed particle hydrodynamics: theory and application to non-spherical stars."*, Monthly Notices of the Royal Astronomical Society (1977), Volume: 181, Issue: 181, Pages: 375-389.

Gonzales, V., Homan, D., Valle, J., Diaz-Cuarda, J.C., 2006, *"A particle-based Lagrangain CFD tool for free-surface simulations"*, World Maritime Technology Conference, London.

Grabowiecki, K., Jastrzebski, T., Taczala M., 2004, *"Numerical Simulation of Crash and Grounding of Inland Waterway Transportation Barges"*, PRADS 2004 Conference, 9th International Symposium of Practical Design of Ships and Other Floating Structures, Germany.

Groenenboom, P.H.L., 1997, *"Numerical simulation of 2D and 3D hypervelocity impact using the SPH option in PAMCRASH"*, International Journal of Impact Engineering, 1997, Vol 20, pp 309-323.

Groenenboom, P.H.L., 2008, *"Lifeboat water entry simulation by the hybrid SPH-FE method"*, Proceedings of the 3rd SPHERIC Workshop, Switzerland.

Groenenboom, P.H.L., Cartwright, B., 2009, *"Hydrodynamics and fluid-structure interaction by coupled SPH-FE method"*, Journal of Hydraulic Research, Vol. 47 Extra Issue (2009), pp. 61–73.

Groenenboom, P.H.L., Cartwright, B., McGuckin, D., 2009, *"Numerical Simulation of ships in High Seas using a Couple SPH –FEA Approach"*, RINA conference on Innovation in High Speed Marine Vessels, Perth, Australia.

Groenenboom, P., Cartwright, B., de Luca, P., Kamoulakos, A., McGuckin, D., Olivarid, L., 2010, "Simulation Based Design for High Performance Composite Sailing Boats", RINA 2nd International Conference on Innovation in High Performance Sailing Yachts, Lorient, France

Groenenboom, P.H.L., 2011, *"A unified view of SPH wall boundary conditions and particle motion correction methods"*, Proceedings of the 6th SPHERIC Workshop, Hamburg, Germany.

Guilcher, P.-M., Ducrozet, G., Alessandrini B., Ferrant P., 2007, *"Water wave propagation using SPH Models."*, Proceedings of the SPHERIC 2nd International Workshop, Madrid, Spain.

Issa, R., and Violeau, D., 2006, *"SPH European Research Interest Community, SIG, Test-case 2, 3D dambreaking"*, Laboratoire National d'Hydraulique et Environnement, http://wiki.manchester.ac.uk/spheric/index.php/Test2 (available at June 2011)

Johnson, A.F., Holzapfel, M., Petrinic, N., 2001, *"Modelling soft body impact on composite Structures"*, European Conference on Computational Mechanics ECCM-2001, Cracow, Poland.

Jones, D. A., Belton, D., 2006, *"Smoothed Particle Hydrodynamics: Applications within DSTO"*, Report DSTO-TR-1922, Defence Science Technology Organisation, Australia, http://dspace.dsto.defence.gov.au/dspace/bitstream/1947/4543/4/DSTO-TR-1922.PR.pdf (as at June 2011).

Kalis, J., 2007, *"Validation of Smoothed Particle Hydrodynamics for water entry phenomena"*, Marine Technology, Master of Science Thesis dissertation, Delft University of Technology.

Kisielewicz, L.T., Ando, K., Petitjean, A., Kivomiva, M., 1993, *"Numerical simulation of a ship colliding against a pier structure"*, ISOPE 1993.

Kohlgruber, D., Pentecote, N., Vigliotti, A., Bartosch, H., and Weissburg, V., 2003, *"FE-analyses of Water Impact Tests on Helicopter Structures*" (Powerpoint Presentation), Fourth International KRASH User's Seminar, Amsterdam.

Lamb, H.L., 1879, 6th Edition 1932, *"Hydrodynamics"*, Cambridge University Press.

Liu M.B., and Liu G.R., 2010, "*Smoothed Particle Hydrodynamics (SPH): an Overview and Recent Developments*", Archives of Computational Methods in Engineering, vol. 17, no. 1, pp. 25-76.

Liu, G.R. 1st edition, 2002, "*Mesh Free Methods*", CRC Press.

Liu, G.R. and Liu M.B., 1st edition, 2003, *"Smoothed Particle Hydrodynamics, a meshfree particle method"*, World Scientific Publishing Co.

Lloyd, A.R.J.M., 1989, (1998 Edition), "Seakeeping: Ship Behaviour in Bad Weather", Ellis Horwood.

Lobovsky, L., Groenenboom P.H.L., 2009, *"Remarks on FSI simulation using SPH"*, 4th SPHERIC Workshop, France, pp 378 – 383.

Lombardi, J.C, Jr.; Sills, A., Rasio, F.A., Shapiro, S.L., 1999, *"Tests of Spurious Transport in Smoothed Particle Hydrodynamics"*, Journal of Computational Physics, Volume 152, pp 687-735.

Lucy, L. B., 1977, *"A Numerical approach to the testing of the fission hypothesis."*, The Astrophysical Journal, vol 82(12), pp 1013 - 1025.

Macfarlane, G. J., Lees, M., 1999, "*A Note on the Effect of Non-linearity on the Prediction of the Vertical Motions of a High Speed Displacement Vessel*", AMC Report Number 99/TT/01, Australian Maritime College.

McCue, L.S., Alford, L., Belknap, W., Bulian, G., Delorme, L., Francescutto, A., Lugni, C., Troesch, A.W., and Vakakis, A., 2006, *"An overview of the minisymposium on 'Extreme Ship Dynamics' presented at the 2005 SIAM Conference on Applications of Dynamical Systems,"* Marine Technology, 2006, Volume 43, No. 1, pp. 55-61.

Monaghan, J., 1985, *"Particle methods for hydrodynamics"*, Computer Physics Reports, Vol 3 Issue 2, pp 71-124.

Monaghan, J. J., Gingold, R.A., 1983, *"Shock simulation by the particle Method SPH"*, Journal of Computational Physics, Vol 52, pp374-389.

Monaghan, J.J., Thompson, M.C., Hourigan, K., 1994, *"Simulation of Free Surface Flows with SPH"*, ASME Symposium on Computational Methods in Fluid Dynamics, Lake Tahoe, USA.

Monaghan, J. J., 1994, "Simulating Free Surface Flows with SPH", Journal of Computational Physics, Vol 110, pp 399 – 406.

Murnaghan, F.D., 1944, *"The Compressibility of Media under Extreme Pressures"*, in Proceedings of the National Academy of Sciences, vol. 30, pp. 244-247.

Nguyen, V., Rabczuk, T., Bordas, S., Duflot, M., 2008, "*Meshless methods: A review and computer implementation aspects"*, Mathematics and Computers in Simulation (2008), Volume: 79, Issue: 3, Pages: 763-813.

Nielsen, B. K., 2003, *"Numerical Predictions of Green Water Loads on Ships"*, PhD Thesis, Maritime Engineering, TU Denmark.

Overpelt, B., 2007, *"Planing in Particles - Smooth Particle Hydromechanics for planing ships"*, Marine Technology, Master of Science Thesis dissertation, Delft University of Technology.

Overpelt, B., Kalis, J., Groenenboom, P., Broekhuijsen, J., 2006, *"Validation of hybrid SPH/FE simulations of the motion of an Amphibious Transport Ship in Waves."*, Proc. EuroPAM2006 Symposium, Toulouse, France.

PAM-CRASH, 2001, "*PAM-CRASH Solver Reference Manual"*, ESI Group, France.

PAM-CRASH, 2009, "*PAM-CRASH Solver Reference Manual"*, ESI Group, France.

REALFLOW, 2010, http://www.realflow.com/ (available at September 2010).

Rogers, B.D., Leduc, J., Marongiu1, J-C., Leboeuf F., 2009, "*Comparison and Evaluation of Multi-phase and Surface Tension models"*, 4th SPHERIC Workshop.

Shepard, D., 1968, *"A two-dimensional interpolation function for irregularly-spaced data."*, Proceedings of the 23rd ACM Conference, ACM Press, Pages: 517-524.

Toso, N. R. S., 2009, "*Contribution to the Modelling and Simulation of Aircraft Structures Impacting on Water"*,PhD Thesis, Institute of Aircraft Design, Universität Stuttgart, Germany.

Ubels, L.C., Johnson A.F., Gallard A.F., and Sunaric M., 2003, *"Design and testing of a composite bird strike resistant leading edge."*, National Aerospace Laboratory, Publication NLR-TP-2003-054.

Vignjevic, R., Campbell, J.C., 2009a, *"Modelling impact on aerospace structures using the coupled FE-SPH approach."*, Proceedings of the 4th SPHERIC Workshop, France.

Vignjevic, R., Campbell, J.C., 2009b, *"Modelling extreme wave loading of offshore structures"*, Proceedings of the 4th SPHERIC Workshop, France.

Vignjevic, R. 2004, "*Review of Development of the Smooth Particle Hydrodynamics (SPH) Method*", Dynamics and Control of Systems and Structures in Space (DCSSS), Riomaggiore, Italy.

Violeau, D., Issa, R. 2007, *"SPHERIC benchmark test case number 5: Sensitivity analysis to numerical and physical parameters."*, Proceedings of the SPHERIC 2nd International Workshop, Madrid, Spain.

Visual, 2009, *"Visual User's Guide"*, ESI Group, France.

Appendices

A1 Abbreviations

AMECRC	- Australian Maritime Engineering Cooperative Research Centre
AMC	- Australian Maritime College
CG	- Centre of Gravity
CFD	- Computational Fluid Dynamics
CPU	- Central Processing Unit (of a computer)
DWL	- Design Water Line
FEA	- Finite Element Analysis
FEM	- Finite Element Method
HSDHF	- High Speed Displacement Hull Form
LCF	- Longitudinal Centre of Flotation
LCB	- Longitudinal Centre of Buoyancy
PBC	- Periodic Boundary Condition
SPH	- Smoothed Particle Hydrodynamics
SWATH	- Small Water-plane Area Twin Hulled vessels
VOF	- Volume of Fluids
XSPH	- a parameter to prevent penetrations of neighbouring SPH particles
SPHERIC	- The SPH European Research Interest Community.

A2 Glossary

α	1st artificial viscosity parameter
β	2nd artificial viscosity parameter
γ	Exponent in the Murnaghan model
ε	- numerical factor for XSPH
	- shear resulting in viscous shear stress
η	numerical constant in the artificial viscosity definition
κ	constant for smoothing length calculation
λ	wavelength, m
μ	dynamic viscosity, Pa.s
Π	artificial viscosity, m5 kg-1 s-2
ρ	density, kg/m3
ρ0	reference density, kg/m3
σ	stress, Pa
τ	viscous shear stress, Pa
Ω	domain of integration, m3
ω	frequency of the waves, rad/sec
B	Bulk modulus, Pa
c	speed of sound, m/s
Fr	Froude number
h	smoothing range, m
hc	contact thickness, m
i,j	particle index
L	principle dimension of a floating object, m
m	particle mass, kg
p	isotropic pressure, Pa
N	number of particles
r	coordinate vector of a point, m
S	- surface within the domain of integration, m2, or
	- the linear scale factor between geometrically similar models
s	average uniform distance between adjacent SPH particles, m
tc	critical time step, s
U	ship velocity, m/s
V, v	particle velocity, m/s
W	smoothing function, m-3

A3 Axes Systems

The axes system for the work here were as follows:

For 3-dimensional systems:

Symbol	Unit	Description
x	m	Longitudinal axis of the vessel
y	m	Transverse axis of the vessel
z	m	Vertical axis of the vessel

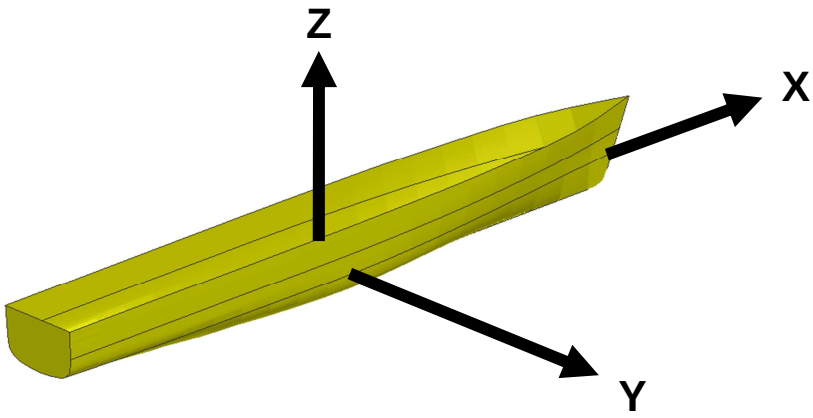

Figure A3-1. Coordinate system.

For 2-dimensional systems the forces and movements were restrained to the XZ plane

A4 Bifilar Suspension

Bifilar suspension is a technique to measure the inertial properties of a model (Bhattacharya 1972) prior to experimental work.

In bifilar suspension the hull is suspended by two thin wires of negligible inertia and stiffness, each located equi-distant from the CG of the vessel. The model is then excited in rotational oscillation about its CG, and allowed to oscillate freely. The period of the oscillation is measured and the following equation used to derive the rotational inertia (Bhattacharya, 1972):

$$k_{zz} = \frac{\sqrt{g}}{4\pi} \cdot \frac{AT}{\sqrt{l}}$$

Where,	k_{zz}	=	radius of gyration about the z axis
	A	=	distance between suspending wires, 1.28m
	T	=	period of oscillation
	l	=	length of suspending wire, 2.0m

A numerical simulation of the bifilar test was performed with A equal to 1.28m and *l* equal to 2.0m. The numerical simulation was used to confirm the inertial response of the FEA model.

Figure A4-1 shows an orthogonal view of model at rest suspended by the wires. Figure A4-2 shows a top view of the hull at the extents of the oscillation. Figure A1-3 shows the angle of rotation of the hull about the Z axis with time. The excitation of the hull is visible in Figure A4-3 as the linear portion of the curve from 1 to 2 seconds. During this motion of the hull was controlled by a boundary condition. At 2 seconds the boundary condition was released, allowing the hull free to rotate under the influence of gravity, the mass at the CG and the tension in the wires.

From Figure A4-3 the period was found to be 1.77 seconds. Using this period and the values quoted above for the model, the radius of gyration, k_{zz}, was calculated to be 0.3993m which compares well with the actual value of 1/4 * LWL, of 0.4m.

This result confirmed the FEA model had the correct radius of gyration in yaw. For long slender ships it is common for the radius of gyration in yaw and pitch to be within 1- 2% of each other (Bhattacharya, 1972), and so for the FEA model the inertia in yaw and pitch were set to be equal.

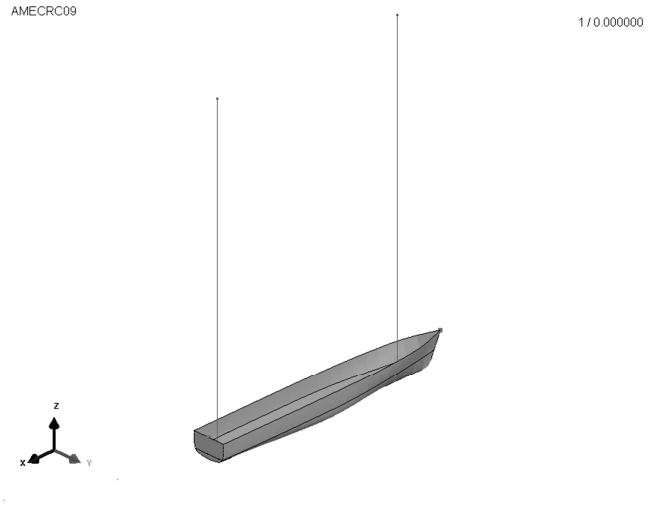

Figure A4-1. Bifilar suspension arrangement in FEA.

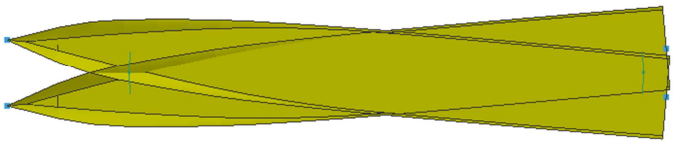

Figure A4-2. Top view of extents of oscillation

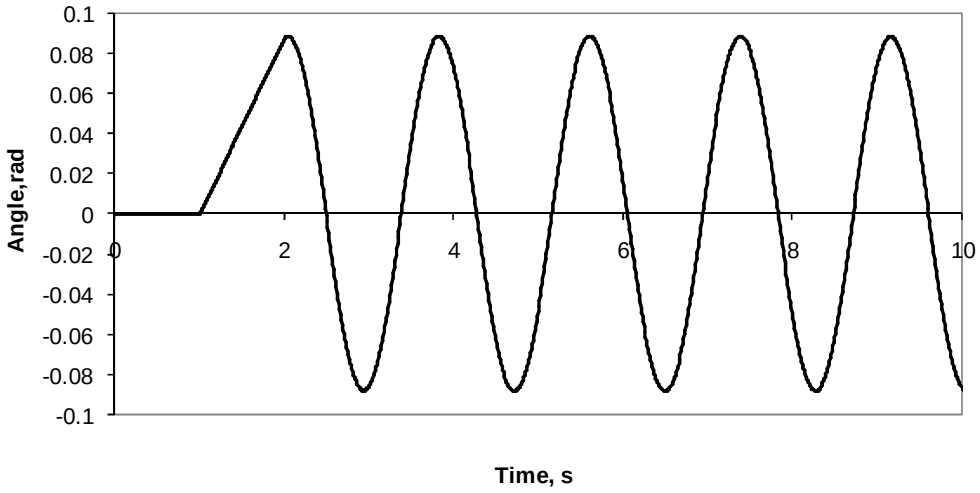

Figure A4-3. CG rotation about Z axis with time for the bifilar suspension simulation in FEA.

A5 Images from a Typical Ship Motion Simulation

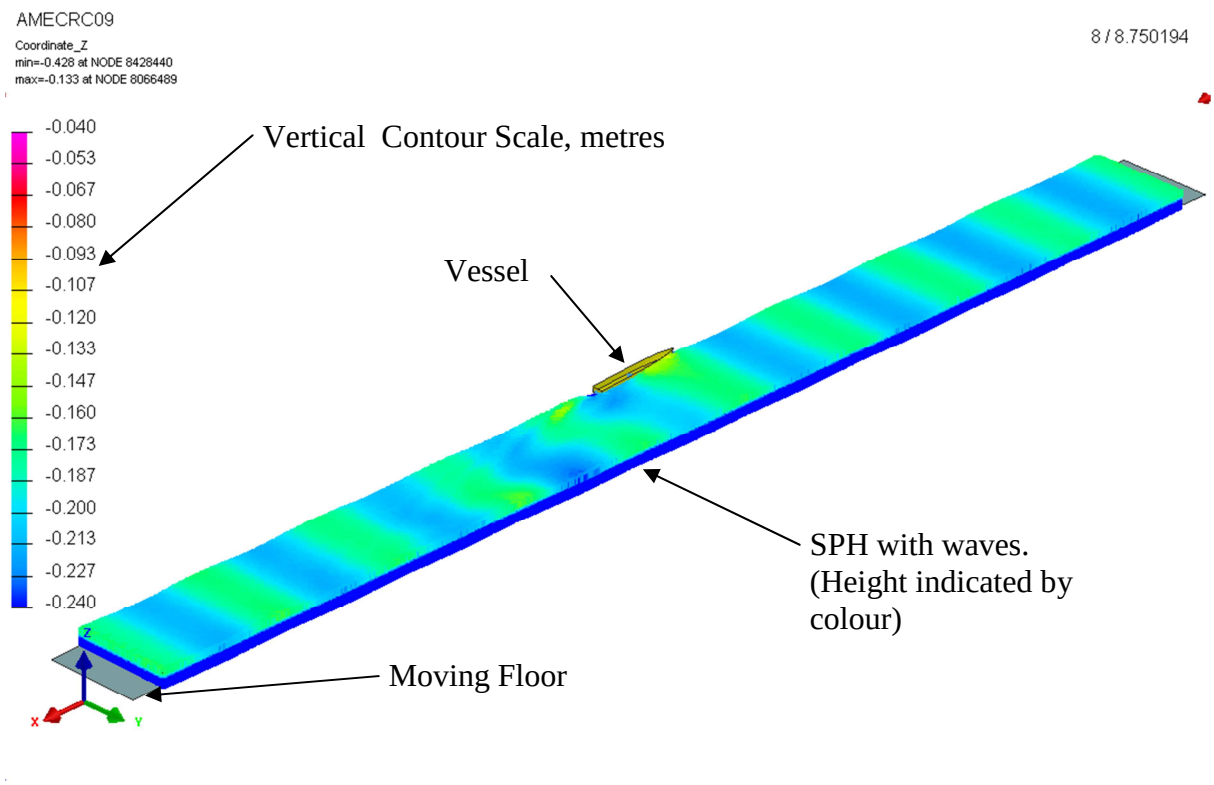

Figure A5-1 General view of the AMECRC09 hull partway through a simulation. As viewed in the post-processor software "VISUAL".

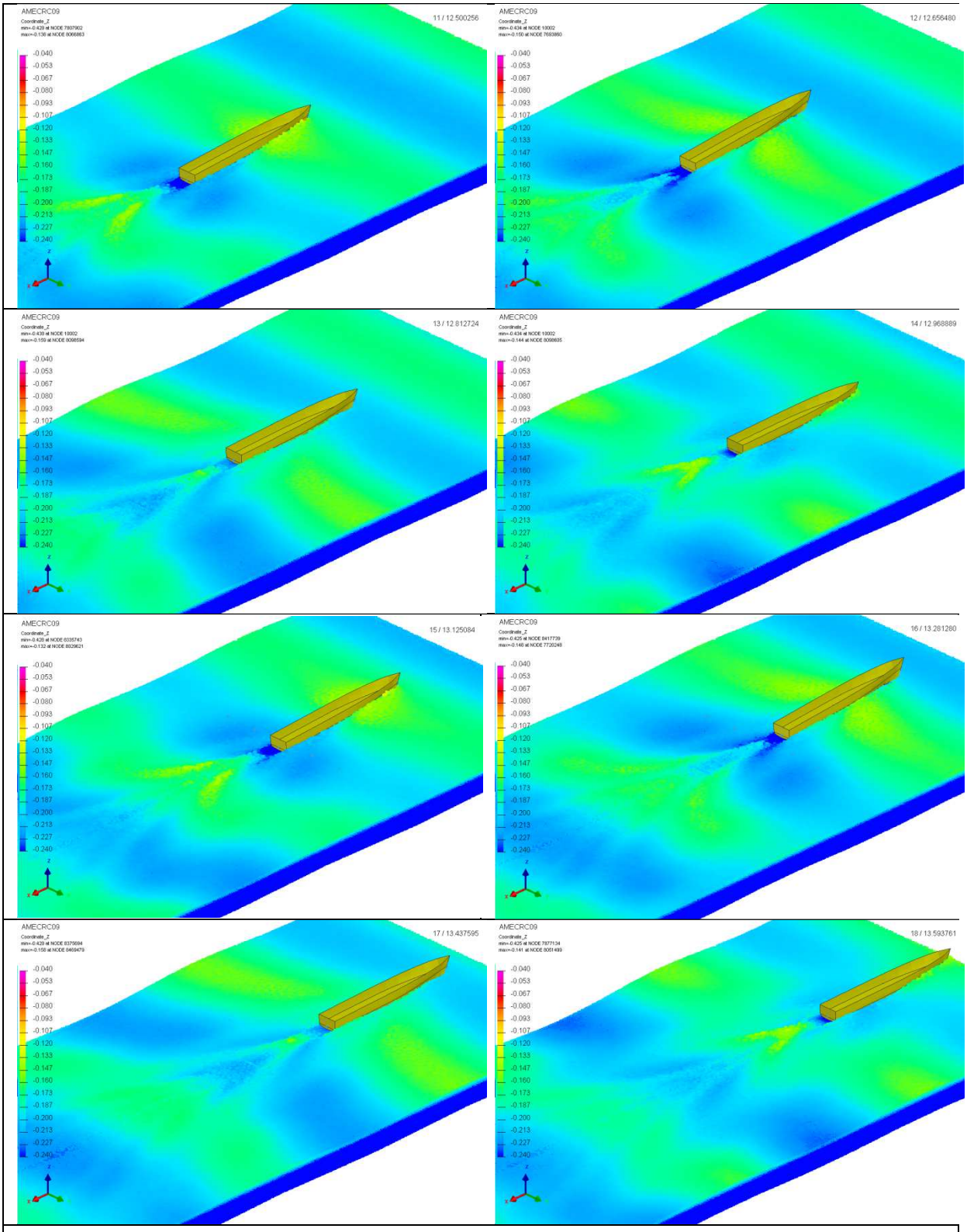

Figure A5-2. Eight sequential images of the AMECRC09 model traversing a wave towards the end of a simulated run at Fr 0.5. Colour on the water surface is vertical height in metres.